University of California
Los Angeles

Numerical Studies of Turbulence in LAPD

A dissertation submitted in partial satisfaction
of the requirements for the degree
Doctor of Philosophy in Physics

by

Brett Cory Friedman

2013

Abstract of the Dissertation

Numerical Studies of Turbulence in LAPD

by

Brett Cory Friedman

Doctor of Philosophy in Physics

University of California, Los Angeles, 2013

Professor Troy A. Carter, Chair

To be completed

The dissertation of Brett Cory Friedman is approved.

Warren B. Mori

George J. Morales

Russel E. Caflisch

Troy A. Carter, Committee Chair

University of California, Los Angeles

2013

To be completed . . .

Table of Contents

List of Figures

List of Tables

Acknowledgments

To be completed ...

Vita

2003-2007	Regent Scholar, University of California, Irvine.
2007	B.S. (Physics) Summa Cum Laude, University of California, Irvine.
2007	Chancellor's Fellow, University of California, Los Angeles.
2007-2009	Teaching Assistant, Department of Physics and Astronomy, University of California, Los Angeles.
2009-2013	Research Assistant, Department of Physics and Astronomy, University of California, Los Angeles.
2009-2012	ORISE FES Fellow, University of California, Los Angeles.
2012-2013	Dissertation Year Fellow, University of California, Los Angeles.

Publications

B. Friedman, T. A. Carter, M. V. Umansky, D. Schaffner, and B. Dudson, Energy dynamics in a simulation of LAPD turbulence, Phys. Plasmas 19, 102307 (2012).

D. A. Schaffner, T. A Carter, G. D. Rossi, D. S. Guice, J. E. Maggs, S. Vincena, and B. Friedman, Modification of Turbulent Transport with Continuous Variation of Flow Shear in the Large Plasma Device, Phys. Rev. Lett. 109, 135002 (2012).

S. Zhou, W. W. Heidbrink, H. Boehmer, R. McWilliams, T. A. Carter, S. Vincena, B. Friedman, and D. Schaffner, Sheared-flow induced confinement transition in a linear magnetized plasma, Phys. Plasmas 19, 012116 (2012).

B. Friedman, M. V. Umansky, and T. A. Carter, Grid convergence study in a simulation of LAPD turbulence, Contrib. Plasma Phys. 52, 412 (2012).

M. V. Umansky, P. Popovich, T. A. Carter, B. Friedman, and W. M. Nevins, Numerical simulation and analysis of plasma turbulence the Large Plasma Device, Phys. Plasmas 18, 055709 (2011).

P. Popovich, M.V. Umansky, T.A. Carter, and B. Friedman, Modeling plasma turbulence and transport in the Large Plasma Device, Phys. Plasmas 17, 122312 (2010).

P. Popovich, M.V. Umansky, T.A. Carter, and B. Friedman, Analysis of plasma instabilities and verification of the BOUT code for the Large Plasma Device, Phys. Plasmas 17, 102107 (2010).

S. Zhou, W. W. Heidbrink, H. Boehmer, R. McWilliams, T. A. Carter, S. Vincena, S. K. P. Tripathi, P. Popovich, B. Friedman, and F. Jenko, Turbulent transport of fast ions in the Large Plasma Device, Phys. Plasmas 17, 092103 (2010).

CHAPTER 1

Introduction

CHAPTER 2

Turbulence and Instability

Turbulence is a ubiquitous phenomenon in fluids and has been studied for centuries. It is often called the last unsolved problem in classical physics because we cannot predict in detail how or why turbulence occurs or fully predict its behavior. It is, however, extremely important to gain an understanding of it in laboratory plasmas and magnetically confined fusion devices because it causes increased particle and energy transport. This is not necessarily a good or bad property as far fusion devices are concerned on the whole – better energy confinement is needed in the core but not in the scrape-off-layer, while good particle confinement is needed in the scrape-off-layer but not in the core. Nevertheless, an enhanced understanding of plasma turbulence would allow for greater control to achieve the properties needed for fusion and would allow for greater prediction of future machine performance.

2.1 Paradigms of Turbulence

In the past, researchers thought that turbulence was a random process that could only be described in a statistical manner [TL72]. This is the classical view of turbulence. This view, however, contradicted the also widely-held belief that the Navier-Stokes equations can fully describe turbulent flow in neutral fluids [McD04]. This is contradictory because the Navier-Stokes equations are deterministic (assuming yet unproven existence of the solutions), so they cannot possibly describe a random flow. Apparently, some scientists in the first half of

the 20^{th} century didn't regard this as a problem, while others took this as a cue to abandon the fully equation-based approach to studying turbulence [TL72]. In any case, statistical theory dominated. Not until the 1970's was a deterministic theory of turbulence formulated. Nevertheless, the deterministic approach does not mean that turbulent statistics are useless because even though the turbulence is not random, it can still be stochastic. I note that random and stochastic are often used interchangeably, but formally, stochastic just refers to a variable whose autocorrelation decays exponentially fast to zero. Thus, a deterministic system may be stochastic, but not random. And stochasticity is sufficient for statistical tools to be effective [McD04].

In any case, certain statistical descriptions are still widely accepted in the fluid and plasma communities. Perhaps the most important is Kolmogorov's theory (K41 theory) of high Reynolds number small scale turbulence [Kol41, TL72]. It's based on the idea that large scale turbulent structures (eddies) are driven by instability at the largest scales (the system and integral scales), which then drive eddies of smaller scales in a cascade process. The cascade process occurs in the inertial wavenumber range, which has a power law spectrum with index of $-5/3$. When energy cascades down to the Kolmogorov scale, viscosity takes the energy away from the eddies, thermally transferring it to the fluid. I show a typical Kolmogorov spectrum in Fig. 2.1.

The modern view of turbulence is that it is deterministic [McD04]. Most of the plasma community readily accepts this as evidenced by its use of deterministic equation sets and simulations used to model plasma turbulence. The first clue that deterministic equations could describe something as apparently random as turbulence was provided by Lorenz in 1963 [Lor63]. He showed that a deterministic equation derived from the Navier-Stokes equations could exhibit random-looking behavior, and that it was sensitive to small changes in initial conditions. In 1971, Ruelle and Takens showed that the Navier-Stokes equations are capable of pro-

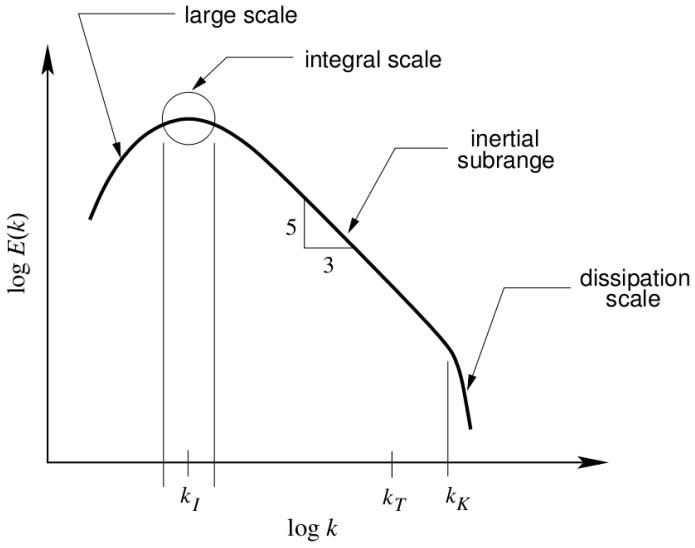

Figure 2.1: Kolmogorov energy spectrum

ducing chaotic solutions that are sensitive to initial conditions and are associated with the mathematical concept of a strange attractor [RT71, McD04]. They also presented a sequence of transitions (bifurcations) that a flow undergoes as the Reynolds number is increased on its way to a chaotic state: steady $\rightarrow$ periodic $\rightarrow$ quasi-periodic $\rightarrow$ chaotic. This isn't the only possible bifurcation sequence; in fact, some flows like Poisueille pipe flow go straight from steady to chaotic. In any case, it's significant that the sequence is short and finite, meaning that fully developed turbulence may occur at finite Reynolds number, and it can be understood in terms of a strange attractor. Interestingly, Biskamp and Kaifen showed that a system of three plasma drift waves undergoes a Ruelle-Takens bifurcation sequence [BK85].

Recently, Maggs and Morales gave support to the deterministic viewpoint of plasma turbulence (in several different machines and experiments) by connecting the exponential frequency spectra observed in many plasma experiments to a deterministic chaotic process [MM11, MM12b, MM12a]. Specifically, they showed

that low-order deterministic dynamical systems could produce the Lorentzian pulses in the time signal that give rise to an exponential frequency spectrum. The Lorentzian pulses are the result of a certain orbit structure surrounding a limit cycle attractor. This showed that experimental turbulence could be explained in terms of deterministic chaos.

Anyhow, this dissertation is not primarily concerned with bifurcations or the nature of a particular strange attractor. I simply mention this to give credence to my use of a deterministic set of dynamical equations to model the turbulence in LAPD. Furthermore, some of my results may be of use to others who wish to pursue the kinds of studies undertaken by Biskamp [BK85] and Maggs [MM12b]. Also, I will occasionally refer to cascades, stochasticity, etc., and I wanted to explain my use of these terms in advance.

2.2 Instability: Turbulent Drive

The focus of this dissertation is on the specific process that drives turbulence in LAPD and possibly many other devices. Turbulence is dissipative and therefore needs a source of energy to sustain itself. Generally, this source comes from a gradient in a steady (equilibrium) variable such as a flow or a pressure. Fluctuations that take energy from these equilibrium gradients often develop certain unstable mode structures that continue to take energy indefinitely. The details of these instabilities are important for understanding the onset of turbulence and the structure of turbulence. Both the neutral-fluid community and the plasma community have studied instabilities in great depth.

2.2.1 Linear Instabilities Aboud in Plasmas

Linear instabilities are those that can grow from infinitesimally small fluctuations about an equilibrium. They can be calculated by linearizing a dynamical equa-

tion set about an equilibrium, where at least one equilibrium profile has a finite gradient. The linear system will generally have the form

$$\frac{\partial \mathbf{v}}{\partial t} = \mathbf{M}\mathbf{v} \tag{2.1}$$

where $\mathbf{v}$ is a vector of independent variables that describe the state of the system and $\mathbf{M}$ is a matrix of coupling coefficients and differential operators. If the equations are coupled, $\mathbf{M}$ is not diagonal. With $\mathbf{v}$ having an exponential time dependence, this equation is an eigenvalue problem, with (generally complex) eigenvalues γ_i and eigenvectors $\boldsymbol{\xi}_i$, which are linearly independent. If any of the eigenvalues sit in the right half of the complex plane, their associated eigenvectors will grow exponentially from noisy infinitessimal perturbations to the equilibrium. In this case, the system is linearly unstable. Now although having an equilibrium profile with a finite gradient is a necessary condition for linear instability, it is not sufficient. At least one of the eigenvalues must have a positive real part. This is why so much effort goes to calculating linear plasma systems, testing for linear instability.

In general, plasma physics has so many more types of equilibrium gradients and physical processes that neutral fluids do not, that there are many more linear plasma instabilities than linear fluid instabilities. Plasmas have linear instabilities due to density gradients, temperature gradients, velocity gradients, current gradients, magnetic field curvature, etc [Wes04, Che06]. Linear plasma instabilities can be collisional, collionless, electrostatic, electromagnetic, ionization-related, sheath-induced, etc. The shear number of instabilities can be overwhelming. In physical systems, any number of linear instabilities can be present at the same time, combining with each other, with some being more significant than others. Often times, it can take quite the effort to identify which linear instability with what specific properties is responsible for turbulence in a given situation. This can be important if one wants to create reduced models or if one wants to be able

to predict the type of turbulence will occur in future machines. Unfortunately, however, this isn't even the entire story as turbulence is inherently nonlinear, opening the door for even more instabilities.

2.2.2 Supercritical Stability and Subcritical Instability

While the plasma community has focused much attention on linear stability of various plasma systems, the neutral-fluid community has long been aware that nonlinear stability effects are crucial to explaining observed transitions from laminar to turbulent flow [Kro99]. The foundations of the theory of nonlinear hydrodynamic stability were laid by Landau [Lan44, LL59]. While his ideas have required much elaboration, qualification, and application, they still contain many ingredients of modern day theory. I outline some of those ideas, following the treatment in Drazin and Reid [DR81].

Landau began with the linear theory of stability of a steady flow, which has a spectrum of linearly independent eigenmodes, each with growth rate σ. For some dimensionless parameter R (generally the Reynolds number in neutral fluids), when $R < R_c$, all modes have $\sigma < 0$. As R increases above R_c, one mode becomes unstable with $\sigma > 0$, where $\sigma \sim R - R_c$ for $|R - R_c| \ll 1$. He described the evolution of the amplitude $|A|$ of the most unstable or least stable mode by what is now called the Landau equation:

$$\frac{d|A|^2}{dt} = 2\sigma|A|^2 - l|A|^4 \tag{2.2}$$

where l is the Landau constant and the $l|A|^4$ term is the nonlinearity. Landau's equation admits an analytic solution given an initial condition, making it easy to explore. Several different qualitative scenarios arise depending on the signs and magnitudes of σ and l. If $l > 0, \sigma > 0$, as $t \to \infty, |A| \to (2\sigma/l)^{1/2}$ no matter the value of the intial condition A_0. This value of $A_e \equiv (2\sigma/l)^{1/2}$ is called an attractor

with a global basin of attraction since any initial state asymptotically evolves to it. Note that the linear problem is unstable because $|A| \to \infty$ as $t \to \infty$, but the nonlinear problem is stable in that it evolves to a finite value as $t \to \infty$. This is called supercritical stability. If $l > 0, \sigma < 0$, as $t \to \infty, |A| \to 0$ for both the linear and nonlinear problem. Here, zero is an attractor. The situation is rather simple for $l > 0$ and the bifurcation diagram for this is shown in Fig. 2.2 a). The branching of the curve of the equilibrium solutions at $R = R_c, |A| = 0$ is called a bifurcation.

On the other hand, if $l < 0, \sigma > 0$, both the linear and the nonlinear problem are unstable with the nonlinear problem growing super-exponentially in time, becoming infinite at finite time. Such a situation is unphysical, and the Landau equation is too simple in this case. The most interesting and most commonly studied case is when $l < 0, \sigma < 0$. If $A_0 < A_e$, the solution decays to zero as $t \to \infty$. However, if $A_0 > A_e$, the solution is unstable and breaks down at finite time. Fig. 2.2 b) depicts the bifurcation diagram for the case of $l < 0$. In this figure, R_G represents a Reynolds number below which the unstable bifurcated solution doesn't exist. This isn't a part of the Landau equation, but Landau suggested that this should be the case.

Furthermore, unlike in the supercritical case, the subcritical case contains regions ($R > R_G$) where the unstable solution is not bounded by a higher region of stability, indicating that the solutions become infinite. In reality, other nonlinear effects due to terms not included in the Landau equation don't allow mode amplitudes to become infinitely large, and the flow can become turbulent. Now the subcritical case is so interesting because it allows for instability and turbulence when a system is linearly stable. This seems to be the case in several different kinds of flows. Landau asserted that Poiseuille pipe flow is an example of this [Lan44]. Poiseuille pipe flow, which is flow with a parabollic velocity profile, is linearly stable for all R, so that $R_c = \infty$. But experimentally, it is known that

for $R = R_G \sim 2000$, it becomes unstable to finite disturbances. Plane Couette flow (flow with linear velocity profile between two infinite moving planes) is another example of this. Plane Poiseuille flow, also admits subcritical instability, but it has a finite R_c, so it's more representative of Fig. 2.2 b) [TTR93].

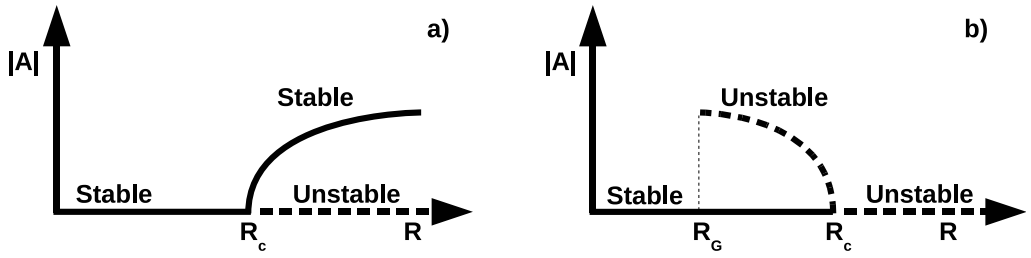

Figure 2.2: Supercritical and subcritical bifurcation diagrams

2.2.3 Non-normality, Transient Growth, and Subcritical Turbulence

Subcritical instability is especially unintuitive when one considers cases in which the nonlinearities of the equation set are energetically conservative, which is often the case. Then, only the linear terms in the equations can extract energy from the equilibrium gradients. It seems reasonable that when all of the linear eigenmodes of a system are stable, there shouldn't be any instability. This makes subcritical instability a mysterious phenomenon in some cases. However, several neutral-fluid researchers in the early 90's explained the mechanism behind linear subcritical growth [Gus91, BF92, RSH93, RH93, TTR93, HR94, Hen96]. The mechanism requires that the eigenvectors of the linear system be nonorthogonal. In other words, the linear operator matrix (like $\mathbf{M}$ in Eq. 2.1) must be non-normal. Such non-normality is a necessary condition for sustained subcritical turbulence

in systems with conservative nonlinearities.

I illustrate the mechanism behind sustained subcritical turbulence with a simple diagram in Fig. 2.3 representing a two-dimensional two-state system. I start in Fig. 2.3 a) with two 2D linear eigenvectors that are not orthogonal to one another, but are largely anti-parallel with a 30^o angle between them. I give them each a starting amplitude so that they form a leg and a hypotenuese of a 30-60-90 triangle. The sum of these vectors, which is the other leg, is the initial state of the system. The squared length of this is the energy of the system. Note that the total energy of the system is $|\mathbf{u}+\mathbf{v}|^2 = |\mathbf{u}|^2 + |\mathbf{v}|^2 + 2\mathbf{u}\cdot\mathbf{v}$. So since the eigenvectors are nonorthogonal, the total energy of the system is not just the sum of the individual energies of the eigenmodes ($|\mathbf{u}|^2 + |\mathbf{v}|^2$), but it includes an interaction term ($2\mathbf{u}\cdot\mathbf{v}$) that can be positive or negative.

Now, in Fig. 2.3 b), I show the result of evolution of the linear system. Linearly, since the vectors are eigenvectors, they grow or decay exponentially at given rates γ_u, γ_v. And since I am interested in the subcritical case, I give both of the vectors negative growth rates. Furthermore, $\mathbf{u}$ has much smaller damping rate than $\mathbf{v}$. After a certain amount of time, under purely linear action – where each vector decays at its characteristic decay rate – the system resides in the state shown in Fig. 2.3 b). Note that I have changed the scales on the axes because the triangle has become much smaller. Perhaps surprisingly, even though both vectors $\mathbf{u}$ and $\mathbf{v}$ have decayed and have smaller magnitudes than they did in Fig. 2.3 a), the total energy of the system (the green line) has grown! Clearly, the reason is that the interaction energy between the two vectors has become less negative. Moreover, if the system were to continue evolving linearly, the total energy would eventually decay as the vectors become smaller. Therefore, the growth of the total energy from a) to b) is called transient growth. One may wonder where this transient energy comes from. The answer is that the energy comes from the equilibrium gradients – the same as unstable linear eigenvectors. So systems in which the

fluctuations are made up of only nonorthogonal stable linear eigenvectors can transiently grow in energy before decaying. At small times, the growth has been shown to be algebraic, meaning it is proportional to time [Wal95]. This is in contrast to growth by unstable linear eigenmodes, which is exponential in time.

Now the linear growth in non-normal linearly stable systems is only transient, but the nonlinearities in the full nonlinear systems can take this transiently injected energy, mix it around, and sustain the fluctuation energy or sustain the turbulence indefinitely. In Fig. 2.3 c), I show how the nonlinearities, which conserve the total energy, can mix the energy between individual modes and the interaction energy. The nonlinearities can essentially prop up the linear eigenvectors individual energies without injecting net energy into the system. Finally, Fig. 2.3 d) shows linear decay of the eigenvectors, bringing the system back to its original state with its original energy. Altogether, this is the basic mechanism of subcritical instability or self-sustained subcritical turbulence in systems with conservative nonlinearities. It is basically a linear mechanism, but it requires nonlinearity to sustain or bootstrap itself. Although my simple diagram makes it seem as though the transient growth mechanism is rather weak (amplifying the total energy from 25 to 36), the mechanism can amplify energies by factors of several thousand in realistic systems [Gus91, BF92].

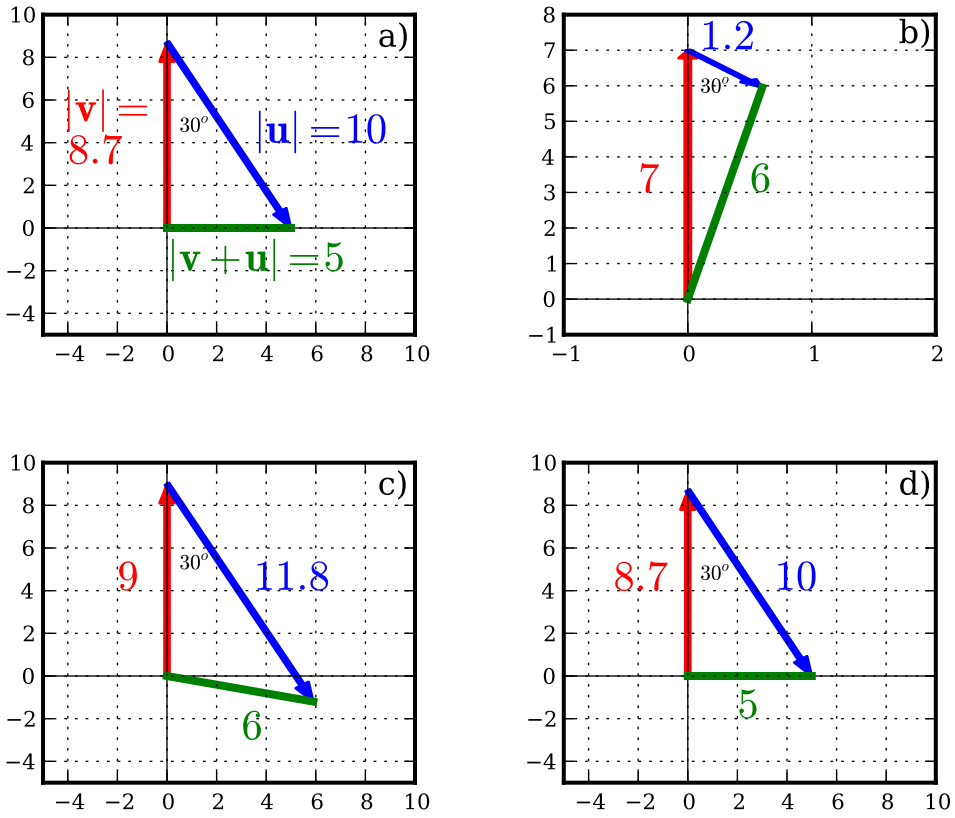

Figure 2.3: Non-normal subcritical instability diagram

CHAPTER 3

The Braginskii Fluid Model and LAPD

3.1 LAPD Suitability to the Braginskii Fluid Model

At a basic level, the state of a plasma is described by seven-dimensional distribution functions $f_j(\mathbf{x}, \mathbf{v}, t)$ for each species j. The behavior of the plasma is described by the system of kinetic equations (Boltzmann equations), which evolve the distribution functions forward in time:

$$\frac{\partial f_j}{\partial t} + \mathbf{v} \cdot \nabla f_j + \frac{e_j}{m_j}(\mathbf{E} + \mathbf{v} \times \mathbf{B}) \cdot \frac{\partial f_j}{\partial \mathbf{v}} = \left(\frac{\partial f_j}{\partial t}\right)_C . \tag{3.1}$$

$\left(\frac{\partial f_j}{\partial t}\right)_C$ is the change in the distribution function due to collisions. For plasmas, the collisions are Coulomb collisions, and the collision term takes the form of the Fokker-Planck operator. With this operator, Eq. 3.1 is called the Fokker-Planck equation. Now it is well known that the Fokker-Planck equation cannot be solved numerically for problems that require time intervals much larger than the electron-cyclotron time due to computational and time limitations. The phase space is just too large. Therefore, reduced equations, such as gyrokinetic, drift kinetic, or fluid equations have been derived to produce numerically tractable equations. These equations are all derived under certain physical assumptions such as strong guiding magnetic fields, small fluctuation levels, or slow spatial and/or time variations such that these different equations are best applied to different physical situations.

The equations that are arguably most suitable to describe waves and turbulence in LAPD (and fastest to solve numerically) are the fluid equations, specif-

ically those derived by Braginskii [Bra65]. In deriving his equations, Braginskii approximates the solution as $f_j = f_j^0 + f_j^1$ where the zero-order piece f_j^0 is a Maxwellian and the first-order piece f_j^1 is a perturbation on the zero-order distribution function: $|f_j^1| \ll f_j^0$. The equations are then derived by taking moments of the Fokker-Planck equation to create coupled equations of the independent variables, $n_j, \mathbf{v_j}$, and T_j. Now certain requirements must hold to justify the Braginskii approximation, all of which have the flavor that macroscopic quantities must vary slowly in time and space. This is generally caused by strong relaxation processes such as collisions, which keep the distribution functions close to Maxwellians. In general, for the Braginskii equations to be applicable, processes of interest must occur on time intervals much greater than the collision time and quantities should vary slowly over distances traversed by the particles between collisions.

Specifically, the requirement that time variations must be slow can be written $\frac{d}{dt} \ll \nu$, where for electron drift wave turbulence, this is approximately $\omega_* \ll \nu_e$. Table 4.3, which displays typical LAPD operating parameters, shows that $\omega_*/\nu_e \sim 0.01$. The requirement that spatial quantities vary slowly compared to the collisional mean free path can be written simply for the direction parallel to the magnetic field as $\lambda_{ei} \sim \lambda_{ee} \ll L_\parallel$. For LAPD, $\lambda_{ei}/L_\parallel \sim 0.01$. For the direction perpendicular to the magnetic field, the same kind of relation $\lambda_{mfp} \ll L_\perp$ must also hold. However, due to the cyclotron motion of particles around the magnetic field, λ_{mfp} is really the larmor radius, unless the collisional mean free path is less than the larmor radius. For electrons, $\rho_e \ll \lambda_{ei}$ and $\rho_e/L_\perp \sim 10^{-4}$ where $L_\perp \sim 0.1$ m. For the ions, the ion cyclotron frequency is close to the ion collision frequency, meaning that either the ion larmor radius or the ion mean free path may be used. Using the larmor radius, $\rho_i/L_\perp \sim 0.01$. Therefore, the collisionality is high enough and the machine dimensions are large enough so that the Braginskii fluid model should be applicable to LAPD.

3.2 The Braginskii Equations

The Braginskii fluid equations are as follows: the continuity equation for species j, electrons or ions, is [Wes04, Bra65]

$$\frac{\partial n_j}{\partial t} = -\nabla \cdot (n_j \mathbf{v}_j). \tag{3.2}$$

The momentum balance equation is

$$n_j m_j \frac{d\mathbf{v}_j}{dt} = -\nabla p_j - \frac{\partial \Pi_{j\alpha\beta}}{\partial x_\beta} + n_j e_j(\mathbf{E} + \mathbf{v_j} \times \mathbf{B}) + \mathbf{R}_j. \tag{3.3}$$

$p_j = n_j T_j$ is the pressure. $\Pi_{j\alpha\beta}$ is the stress tensor, which involves the products of viscosity coefficients and rate-of-strain tensor components. The viscosity coefficients are some of the several terms that are called transport coefficients. The transport coefficients are calculated by the Braginskii procedure in terms of n, $\mathbf{v}$, and T. $\mathbf{R}_j$, which involves several other transport coefficients, is the rate of collional momentum transfer. The momentum transfer from ions to electrons is given by

$$\mathbf{R}_e = -m_e n_e \nu_e (0.51 u_{\parallel e} + \mathbf{u}_{\perp e}) - 0.71 n_e \nabla_\parallel T_e - \frac{3}{2}\frac{n_e \nu_e}{\omega_{ce}} \mathbf{b} \times \nabla T_e \tag{3.4}$$

where $\mathbf{u} = \mathbf{v}_e - \mathbf{v}_i$ and ν_e is the electron collision frequency with ions. $\mathbf{R}_e$ includes both the friction force and the thermal force, which, like the friction force, is due to electron-ion collisions, but originates from the temperature dependence of the collisionality. The thermal force terms are those proportional to the gradients of temperature. $\mathbf{R}_i = -\mathbf{R}_e$ in a fully ionized plasma with one ion species. However, LAPD has a significant neutral density. Collisions with neutrals are much more important for the ions [PUC10a]. So

$$\mathbf{R}_i = -\mathbf{R}_e - n_i m_i \nu_{in} \mathbf{v_i}. \tag{3.5}$$

The energy balance equation is

$$\frac{3}{2}n_j\frac{\partial T_j}{\partial t} = -n\mathbf{v}_j\cdot\nabla T_j - p_j\nabla\cdot\mathbf{v}_j - \nabla\cdot\mathbf{q}_j - \Pi_{j\alpha\beta}\frac{\partial v_j\alpha}{\partial x_\beta} + Q_j \tag{3.6}$$

where the term involving the stress tensor describes viscous heating. The electron heat flux (with more transport coefficients) is

$$\begin{aligned} q_e = n_eT_e\left(0.71u_\parallel + \frac{3\nu_e}{2\omega_{ce}}\mathbf{b}\times\mathbf{u}\right) \\ +\frac{n_eT_e}{m_e\nu_e}\left(-3.16\nabla_\parallel T_e - \frac{4.66\nu_e^2}{\omega_{ce}^2}\nabla_\perp T_e - \frac{5\nu_e}{2\omega_{ce}}\mathbf{b}\times\nabla T_e\right) \end{aligned} \tag{3.7}$$

where the first part of this expression constitutes convection, while the second part is conduction. The ion heat flux is

$$q_i = \frac{n_iT_i}{m_i\nu_i}\left(-3.9\nabla_\parallel T_i - \frac{2\nu_i^2}{\omega_{ci}^2}\nabla_\perp T_i - \frac{5\nu_i}{2\omega_{ci}}\mathbf{b}\times\nabla T_i\right). \tag{3.8}$$

The last transport coefficients are in the heating Q. The ion heating due to collisional heat exchange between ions and electrons is

$$Q_i = \frac{3m_e}{m_i}n_e\nu_e(T_e - T_i) \tag{3.9}$$

while the electron heating is

$$Q_e = -\mathbf{R}\cdot\mathbf{u} - Q_i. \tag{3.10}$$

The electron heat exchange involves an ohmic heating contribution ($\mathbf{R}\cdot\mathbf{u}$) that is absent from the ion heating because electrons colliding with ions transfer very little momentum to the ions.

3.3 The Vorticity Equation

Now the Braginskii equations in the previous section contain electric and magnetic fields which must be self-consistently determined by the charges and currents that are evolved by the equations. This is done with the inclusion of Maxwell's equations. Two of those equations are used to write the fields in terms of potentials:

$$\begin{aligned} \mathbf{E} &= -\nabla\phi - \frac{\partial \mathbf{A}}{\partial t} \\ \mathbf{B} &= \nabla \times \mathbf{A}. \end{aligned} \tag{3.11}$$

The vector potential $\mathbf{A}$ is strictly a fluctuating quantity, meaning it is not used to describe the guide field $\mathbf{B}_0$. The next equation,

$$\nabla \times \mathbf{B} = \nabla(\nabla \cdot \mathbf{A}) - \nabla^2 \mathbf{A} = \mu_0 \mathbf{j} \tag{3.12}$$

is used to relate the vector potential to the current, where the displacement current is neglected as is generally done in plasmas. The Poisson equation is not that useful for the main part of the plasma, in which the quasineutrality relation, $n_e = n_i \equiv n$, holds. The useful equation that can be used instead is the conservation of charge (or ambipolarity condition), $\nabla \cdot \mathbf{j} = 0$. The vorticity equation is derived from this conservation of charge equation.

The current is $\mathbf{j} = en(v_{\parallel i} - v_{\parallel e}) + en(\mathbf{v}_{\perp i} - \mathbf{v}_{\perp e})$. In LAPD, the parallel current is carried primarily by the fast streaming electrons, while the perpendicular current is primarily carried by the ions, which have larger Larmor radii. So the conservation of charge equation can be simplified to

$$\nabla_\parallel (n v_{\parallel e}) = \nabla_\perp \cdot (n \mathbf{v}_{\perp i}). \tag{3.13}$$

The perpendicular ion component of this equation is derived from Eq. 3.3

for the ions. Neglecting terms that have finite ion temperature (pressure and stress tensor), and solving for the ion velocity in the Lorentz force term, the perpendicular ion velocity has three terms [PUC10a, SC03]:

$$\mathbf{v}_{\perp i} = \mathbf{v}_E + \mathbf{v}_{pi} + \mathbf{v}_{\nu i} \tag{3.14}$$

where the $\mathbf{E} \times \mathbf{B}$ velocity is $\mathbf{v}_E = \mathbf{E} \times \mathbf{B}/B^2 = -\nabla_\perp \phi \times \mathbf{B}/B^2$, the polarization velocity is $\mathbf{v}_{pi} = (1/\omega_{ci})\mathbf{b} \times (\partial_t + \mathbf{v}_i \cdot \nabla)\mathbf{v}_i$, and the Pedersen velocity is $\mathbf{v}_{\nu i} = (\nu_{in}/\omega_{ci})\mathbf{b} \times \mathbf{v}_i$. The charge conservation equation then takes the form:

$$\nabla_\parallel (n v_{\parallel e}) = \frac{1}{\omega_{ci}} \nabla_\perp \cdot \left[n\mathbf{b} \times (\partial_t + \mathbf{v}_i \cdot \nabla + \nu_{in})\mathbf{v}_i \right]. \tag{3.15}$$

Note that the $\mathbf{E} \times \mathbf{B}$ velocity doesn't contribute to the current due to the electrons producing an equal and opposite $\mathbf{E} \times \mathbf{B}$ current. I now employ the approximation $\mathbf{v}_i \sim \mathbf{v}_E$ to Eq. 3.15. This approximation wasn't appropriate of course for Eq. 3.14 due to the fact that $\mathbf{v}_E$ doesn't contribute to the current, but it is appropriate here. Then,

$$\begin{aligned} \nabla_\parallel (n v_{\parallel e}) &= \frac{1}{\omega_{ci}} \nabla_\perp \cdot \left[n\mathbf{b} \times (\partial_t + \mathbf{v}_E \cdot \nabla + \nu_{in})\mathbf{v}_E \right] \rightarrow \\ \nabla_\parallel (n v_{\parallel e}) &= -\frac{m_i}{eB^2} \nabla_\perp \cdot \left[n\mathbf{b} \times (\partial_t + \mathbf{v}_E \cdot \nabla + \nu_{in}) \nabla_\perp \phi \right]. \end{aligned} \tag{3.16}$$

Next, defining the vorticity as $\varpi \equiv \nabla_\perp \cdot (n \nabla_\perp \phi)$, the vorticity equation reads,

$$\frac{\partial \varpi}{\partial t} = -\mathbf{v}_E \cdot \nabla_\perp \varpi - \nabla_\perp \mathbf{v}_E : \nabla_\perp (n \nabla_\perp \phi) - \frac{eB^2}{m_i} \nabla_\parallel (n v_{\parallel e}) - \nu_{in} \varpi. \tag{3.17}$$

Finally, the term with the tensor product can be rewritten in a different form [PUC10a]:

$$\frac{\partial \varpi}{\partial t} = -\mathbf{v}_E \cdot \nabla_\perp \varpi + \frac{1}{2}(\mathbf{b} \times \nabla_\perp n) \cdot \nabla_\perp \mathbf{v}_E^2 - \frac{eB^2}{m_i} \nabla_\parallel (n v_{\parallel e}) - \nu_{in} \varpi. \tag{3.18}$$

3.4 Minimizing the Equation Set for LAPD Parameters

3.4.1 The Reduced Equations

The continuity equations 3.2 for electrons and ions do not have to both be used due to the quasineutrality condition $n_e = n_i \equiv n$. So, if one focuses on the electron continuity equation, then,

$$\frac{\partial n}{\partial t} = -\nabla \cdot (n\mathbf{v}_e). \tag{3.19}$$

Now, $\mathbf{v}_e = \mathbf{v}_{\perp e} + v_{\parallel e}$, where $\mathbf{v}_{\perp e} = \mathbf{v}_E + \mathbf{v}_{de} + \mathbf{v}_{pe}$, with the diamagnetic velocity $\mathbf{v}_{de} = \frac{\mathbf{b}\times\nabla p_e}{en_eB}$, which wasn't included for the ions in Eq. 3.14 due to the neglect of ion pressure. To a good approximation, the electron polarization velocity is smaller than the $\mathbf{E}\times\mathbf{B}$ velocity, so that $\nabla \cdot (n\mathbf{v}_{\perp e}) = \mathbf{v}_E \cdot \nabla n$ [PUC10a, SC03]. So, the continuity equation reads

$$\frac{\partial n}{\partial t} = -\mathbf{v}_E \cdot \nabla n - \nabla_\parallel (n v_{\parallel e}). \tag{3.20}$$

Next, the momentum equations (Eq. 3.3), of which there are six (three for electron velocity components and three for ion velocity components) are reduced to two here. The first is the vorticity equation (Eq. 3.18), in which I used the perpendicular momentum equations to derive it. The second is the equation for the parallel electron momentum. I neglect the parallel ion momentum equation since $v_{\parallel e} \gg v_{\parallel i}$ for LAPD. The electron parallel momentum equation is then

$$nm_e \frac{\partial v_{\parallel e}}{\partial t} = -nm_e \mathbf{v}_E \cdot \nabla v_{\parallel e} - \nabla_\parallel p_e - enE_\parallel - 0.71 n \nabla_\parallel T_e - 0.51 m_e n \nu_e v_{\parallel e}, \tag{3.21}$$

where the viscous terms have been neglected. The conservation of energy equations (Eq. 3.6) are left. Since the ion temperature in LAPD is very low

($T_i \leq 1$ eV), the ion energy equation is neglected. The electron energy equation is [SC03]

$$\frac{3}{2}n\frac{\partial T_e}{\partial t} = -\frac{3}{2}n\mathbf{v}_E \cdot \nabla T_e - p_e\nabla_\parallel v_{\parallel e} + 0.71T_e\nabla\cdot(nv_{\parallel e}) \\ +\nabla_\parallel(\kappa_{\parallel e}\nabla_\parallel T_e) + 0.51m_e n\nu_e v_{\parallel e}^2 - 3\frac{m_e}{m_i}n\nu_e T_e, \tag{3.22}$$

where $\kappa_{\parallel e} = 3.16\frac{nT_e}{m_e\nu_e}$.

3.4.2 The Electrostatic Justification

Plasma currents create magnetic fields in plasmas. Often times, analytic and numerical calculations of plasma waves and turbulence neglect the time dependent magnetic field perturbations, focusing only on the electrostatic contribution to the waves, turbulence, and transport. In the reduced fluid equations of the previous subsection, the magnetic perturbation enters in two important ways. First, it enters the electric field term of Eq. 3.21 because $E_\parallel = -\nabla_\parallel\phi - \frac{\partial A_\parallel}{\partial t}$, where $A_\parallel$ is the parallel component of the vector potential. Second, it affects the parallel gradient operator, $\nabla_\parallel = \mathbf{b}\cdot\nabla$ where $\mathbf{b}$ is in the direction of the total magnetic field [SC03]. In the electrostatic limit, $A_\parallel \to 0$, so $E_\parallel = -\nabla_\parallel\phi$ and $\nabla_\parallel = \mathbf{b}_0\cdot\nabla$. I take this limit in the remaining chapters, but there is the question of how justified I am to do so.

As a first step in answering this question, examine Eq. 3.21. The four independent variables, $n, \phi, v_{\parallel e}$, and T_e, which each have their own evolution equation, are all present in Eq. 3.21. Taking the parallel projection of Eq. 3.12 gives

$$\nabla_\perp^2 A_\parallel = -\mu_0 j_\parallel = \mu_0 nev_{\parallel e}. \tag{3.23}$$

So $A_\parallel \sim \mu_0 neL_\perp^2 v_{\parallel e}$, where $\nabla_\perp^2 \sim 1/L_\perp^2$. Then, Eq. 3.21 can be approximately rewritten as,

$$nm_e\frac{dv_{\parallel e}}{dt} \sim -T_e\nabla_\parallel n + en\nabla_\parallel\phi + \mu_0 e^2 n^2 L_\perp^2 \frac{\partial v_{\parallel e}}{\partial t} - 1.71n\nabla_\parallel T_e - 0.51 m_e n\nu_e v_{\parallel e}. \quad (3.24)$$

The electromagnetic induction term, ($EM = en\frac{\partial A_\parallel}{\partial t}$) is now written in terms of $v_{\parallel e}$ as $EM = \mu_0 e^2 n^2 L_\perp^2 \frac{\partial v_{\parallel e}}{\partial t}$. It can therefore be directly compared to the other terms proportional to $v_{\parallel e}$ to test for its importance. The other terms are the inertial term, $M = nm_e\frac{dv_{\parallel e}}{dt}$ and the resistive term, $R = 0.51 m_e n\nu_e v_{\parallel e}$. A common way to compare these terms is to approximate the time derivative as the ion cyclotron frequency $\frac{\partial}{\partial t} \sim \omega_{ci}$ and the perpendicular length scale as the ion sound gyroradius $L_\perp \sim \rho_s$, where $\rho_s = c_s/\omega_{ci}$. Then the ratio of the three terms (obtained by dividing each term by $eBnv_{\parallel e}$) is:

$$M : EM : R = \frac{m_e}{m_i} : \beta : \frac{0.51\nu_e}{\omega_{ce}}. \quad (3.25)$$

It can be seen from Table 4.3 that in LAPD, this ratio is $1 : 3.6 : 1.5$. Thus, all three terms are of the same order with the electromagnetic term slightly larger than the other two. It seems then quite unjustified to use an electrostatic approximation.

However, estimating $\frac{\partial}{\partial t} \sim \omega_{ci}$ isn't necessarily accurate. The equation set describes drift waves and so a more proper estimate might be $\frac{\partial}{\partial t} \sim \omega_*$. Under this approximations, the ratio is $1 : 3.6 : 70$, meaning that the resistive term is more than an order of magnitude larger than the other two; however, the approximation $\frac{\partial}{\partial t} \sim \omega_*$ is still rough and the numerical value of ω_* in Table 4.3 is somewhat of a rough itself. Moreover, one could also argue with the approximation of the perpendicular length scale as the sound gyroradius. This is probably too small, in which case the electromagnetic inductance has been underestimated. While it's clear that the inertial term is probably unimportant, the inductive term could be important.

Similarly, the contribution of $\tilde{\mathbf{b}} \sim A_\parallel$ in $\nabla_\parallel$ can be approximated in a similar manner with similar inconclusive results. Without a clear separation between the resistive and inductive terms, the best way to determine the validity of the electrostatic approximation is by direct numerical calculation of the turbulence with and without the electromagnetic contributions. Therefore, I simulated an electrostatic and two electromagnetic versions of LAPD turbulence. The details of the electrostatic code are described in Chapter 4 and in Appendix A.

The only difference between the electrostatic and the first electromagnetic simulation is the exclusion/inclusion of the electromagnetic term $en\frac{\partial A_\parallel}{\partial t}$ in the parallel electron momentum equation (Eq. 3.21). Of course the Maxwell equation (Eq. 3.12) must also be included for the electromagnetic simulation. The second electromagnetic simulation includes not only this term but also the $A_\parallel$ contribution to $\nabla_\parallel$ in the parallel electron momentum equation.

Now, turbulence is best characterized and compared in a statistical and often spectral manner. More details of turbulence characterization and comparison will be discussed later, but for now, I make a few statistical comparisons between the electrostatic and electromagnetic simulation results. Figure 3.1 shows the results of the three simulations as well as the experiment – namely, a comparison of the frequency spectra, the probability distribution function (pdf), and the rms level of the density fluctuations. The "Full Electromagnetic" curves are from the simulation including the $A_\parallel$ contribution to $\nabla_\parallel$, while the "Electromagnetic" curves just include the $A_\parallel$ contribution to $E_\parallel$. Clearly, the fluctuations are statistically similar in all cases and none of the simulations are inconsistent with the experiment. However, the electromagnetic effects are noticable, and as I include more electromagnetic contributions in the simulations, the turbulent statistics more closely resemble those of the experiment. I make no quantitative comparison here, but rely only on a visual examination in making this conclusion.

Now, as mentioned above, I do not include any electromagnetic contributions

in the simulations used in the following chapters. It seems rather unjustified to do so since I am clearly able to run electromagnetic simulations and they seem to reproduce experimental turbulence with slightly better accuracy than the electrostatic ones. One justification for my abandonment of electromagnetic simulations, however, is that electromagnetic simulations take a bit longer than electrostatic ones due to the extra relation in Eq. 3.12 that is used to solve for $A_\parallel$, which requires an inversion of the Laplacian. This takes extra computation. Another justification is that the electromagnetic equations make the energy dynamics analysis in Chapter 6 a bit more complicated. Both of these factors are mitigated, however, if the inertial term $nm_e \frac{dv_{\parallel e}}{dt}$ is dropped. Nevertheless, at the beginning of this work, I strived to find the simplest possible model to describe the turbulence in LAPD, and I determined that the electrostatic approximation was acceptable. At that time, I didn't have the results of Fig. 3.1. If I had the time, I would redo all of the simulations and analysis to include electromagnetic contributions, but drop the inertial term in Eq. 3.21. This is a clear route to take for future work. Nevertheless, I am confident that electromagnetics would not change any of my conclusions in this work. So for the remainder of this work, I will present theoretical calculations, simulation results, and conclusions using the electrostatic approximation.

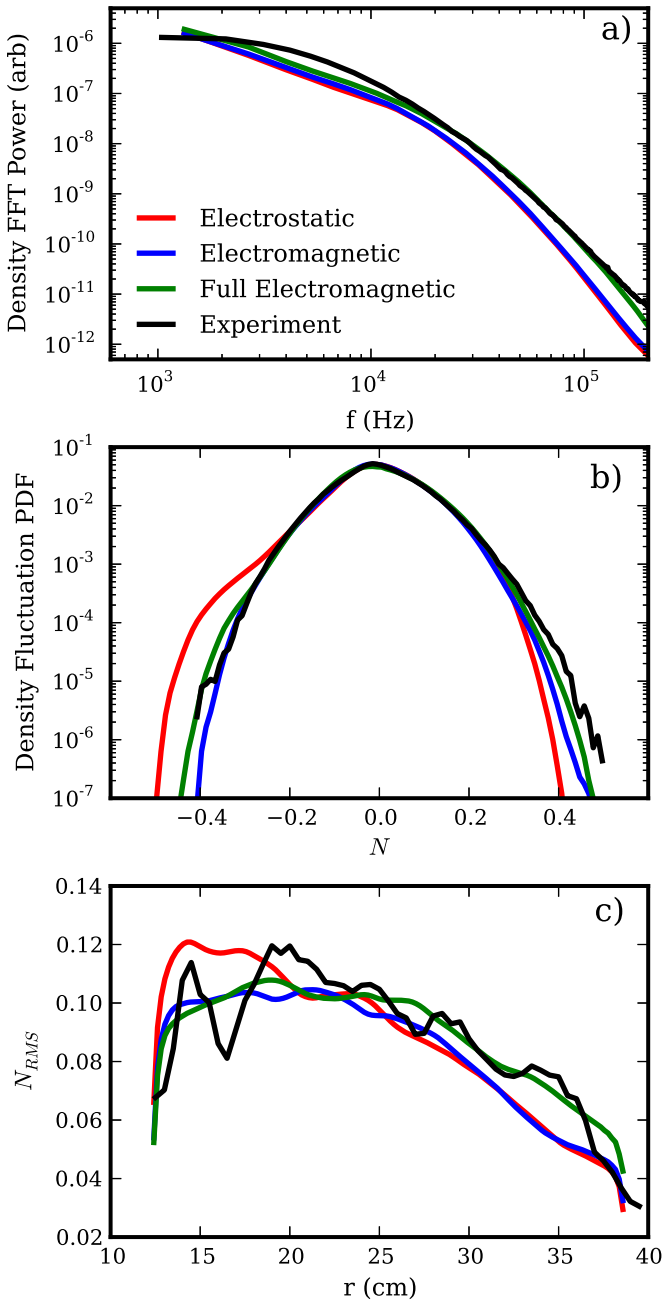

Figure 3.1: Electromagnetic statistics comparison

CHAPTER 4

LAPD Simulation Details

In this chapter, I state and explain the equations, boundary conditions, parameters, and profiles that I use in the LAPD simulations. There are two main classes of simulations: those with a mean radial electric field and those without. The simulations with the mean radial electric field will be explored in Chapter 9. This chapter and all those up to Chapter 9 deal with the simulations with no mean radial electric field. There are only four different simulations that are used until Chapter 9, and they differ in only one way: their axial boundary conditions, which are explained in Sec. 4.2.

I solve the equations using the BOUT++ code [DUX09]. The code is discussed and partially displayed in Appendix A, and specific numerical routines and other details are described there as well.

4.1 The Equations

I use the Braginskii equations as shown in Chapter 3 to model LAPD turbulence. I separate all variables into time-independent equilibrium parts and time-dependent fluctuating parts. I do this in order to input experimental time-independent profiles. The alternative would be to solve the full equations with no equilibrium/fluctuation separation and no experimental profile input. The difficulty in this alternative technique is the need to specify sources, sinks, and boundary conditions, which can be difficult to measure or estimate. This alternative method has

been untertaken by Rogers and Ricci [RR10]. Our approach is easier, and since the time-independent profiles are so important in driving the turbulence, I feel that inputing the experimentally measured profiles can help produce physically realistic turbulence.

Now due to the equilibrium/fluctuation separation technique, I can linearize the equations, keeping only one nonlinearity in each equation: the advective nonlinearity. While this isn't necessary, it does simplify the energy dynamics as formulated in Chapter 6. The justification is practical rather than mathematical, and the partially linearized equations produce fluctuations that are quite statistically similar to experimental fluctuations, which is shown in Chapter 5, so I feel justified in doing this.

In the equations below, I normalize all quantities to give dimensionless variables. All times are normalized to the inverse ion cyclotron frequency $\omega_{ci} = \frac{eB}{m_i}$, velocities are normalized to the ion sound speed $c_s = \sqrt{\frac{T_e}{m_i}}$, lengths are normalized to the sound gyro-radius $\rho_s = c_s/\omega_{ci}$, potentials to T_e/e, densities to the density at the radial cylindrical axis, and temperatures to the temperature at the cylindrical axis. Quantities such as c_s that are typically functions of radius due to the radial dependence of the electron temperature are taken to be constant in these normalizations, where I use the values at the radial axis. The equations below don't reflect this, but the transport coefficients in the actual code do. So, the LAPD simulation equations are as follows:

$$\partial_t N = -\mathbf{v_E} \cdot \nabla N_0 - N_0 \nabla_\parallel v_{\parallel e} + \mu_N \nabla_\perp^2 N + S_N + \{\phi, N\}, \tag{4.1}$$

$$\partial_t v_{\parallel e} = -\frac{m_i}{m_e}\frac{T_{e0}}{N_0}\nabla_\parallel N - 1.71\frac{m_i}{m_e}\nabla_\parallel T_e + \frac{m_i}{m_e}\nabla_\parallel \phi - \nu_e v_{\parallel e} + \{\phi, v_{\parallel e}\}, \tag{4.2}$$

$$\partial_t \varpi = -N_0 \nabla_\parallel v_{\parallel e} - \nu_{in}\varpi + \mu_\phi \nabla_\perp^2 \varpi + \{\phi, \varpi\}, \tag{4.3}$$

$$\partial_t T_e = -\mathbf{v_E} \cdot \nabla T_{e0} - 1.71\frac{2}{3}T_{e0}\nabla_\parallel v_{\parallel e} + \frac{2}{3N_0}\kappa_{\parallel e}\nabla_\parallel^2 T_e - \frac{2m_e}{m_i}\nu_e T_e + \mu_T \nabla_\perp^2 T_e + S_T + \{\phi, T_e\}. \tag{4.4}$$

Note that the advective nonlinearities in each equation are written with Poisson brackets. Additionally, the only equilibrium profiles are N_0 and T_{e0}, which are only functions of radius. $\phi_0 = v_{\parallel e0} = 0$ in these equations. The linearized vorticity is $\varpi = \nabla_\perp \cdot (N_0 \nabla_\perp \phi)$. $N, v_{\parallel e}, \phi$, and T_e are fluctuating first-order quantities.

These equations have a few additional terms not included in the equations of Chapter 3. First, I have included density and temperature sources S_N and S_T. I have left out a momentum source as well as the contribution of the density source to changes of the momentum and temperature. Second, I have included diffusive ($\mu_N \nabla_\perp^2 N$ and $\mu_T \nabla_\perp^2 T_e$) and viscous ($\mu_\phi \nabla_\perp^2 \varpi$) terms in Eqs. 4.1, 4.4, and 4.3 respectively.

4.1.1 Sources

The density source is actually a source/sink. It models both the ionization of neutral atoms as well as the recombination of ions and electrons. The sink action in LAPD is dominated by parallel (along $\mathbf{B}$) losses to materials at the machine ends because the magnetic field prevents rapid radial loss. It's also possible that a layer of neutral atoms near the end of the machine opposite the cathode cools the plasma enough so that recombination can be strong in this layer. The sink action occurs at all radii with finite plasma density, which constitutes regions both inside and outside of the cathode radius due to radial ion transport. If the sink action is primarily at the end plates, the sink can be calculated by $2n_{se}c_s/L_\parallel$, where n_{se} is the density at the sheath edge in front of the end plate, c_s is the sound speed at the sheath edge, and the factor of 2 accounts for the two plates. n_{se} and c_s are functions of radius such that the sink is strongest at the radial axis and decreases at larger radii. Calculation of the sink term requires knowledge of the density and temperature at the end of the machine, which is generally not measured experimentally.

The ionization source occurs primarily inside of the cathode radius. The source term is calculated with $n_e n_n \langle \sigma v \rangle_{iz}$, where n_n is the neutral Helium density and $\langle \sigma v \rangle_{iz}$ is the ionization rate of Helium and is a strong function of temperature. The strong temperature dependence is the reason why ionization occurs only within the cathode radius. Ionization rates are readily available [Sta00], but the neutral density is not, making the source difficult to calculate. However, it is clear that if one were to sum up the source and sink and integrate axially, the region inside of the cathode radius must be a net source, while the region outside of it must be a net sink.

Now when I simulate the turbulence in LAPD without the source terms, turbulence drives radial transport such that the total flux-surface-averaged density gradient relaxes over time as seen in Fig. 4.1 a) until the radial transport ceases. It's interesting that $\langle N_t \rangle_{fs} = \langle N_0 + N \rangle_{fs}$ doesn't become totally flat, but maintains a gradient. This is probably a result of the partial linearization of the equations, especially the diffusion term $\mu_N \nabla_\perp^2 N$, and possibly boundary conditions. Nevertheless, the strong relaxation is not physical due to the presence of the physical source/sink mechanism. (Note that the equilibrium density profile N_0 used in the simulation to make Fig. 4.1 a) is not the same N_0 shown in Fig. 4.2. I show the relaxation of the profile in Fig. 4.1 a) because it has a very steep gradient, which makes the relaxation effect more pronounced and easier to see.)

Now, rather than developing a first principle's source based on the theoretical source/sink expressions, I use ad hoc controlling sources. I estimate that $\langle N_t \rangle_{fs}$ remains constant over time, and model the source using the integral portion of a PID controller. This means that I write an equation for the source:

$$\partial_t S_n = - \langle N \rangle_{fs} . \tag{4.5}$$

Therefore,

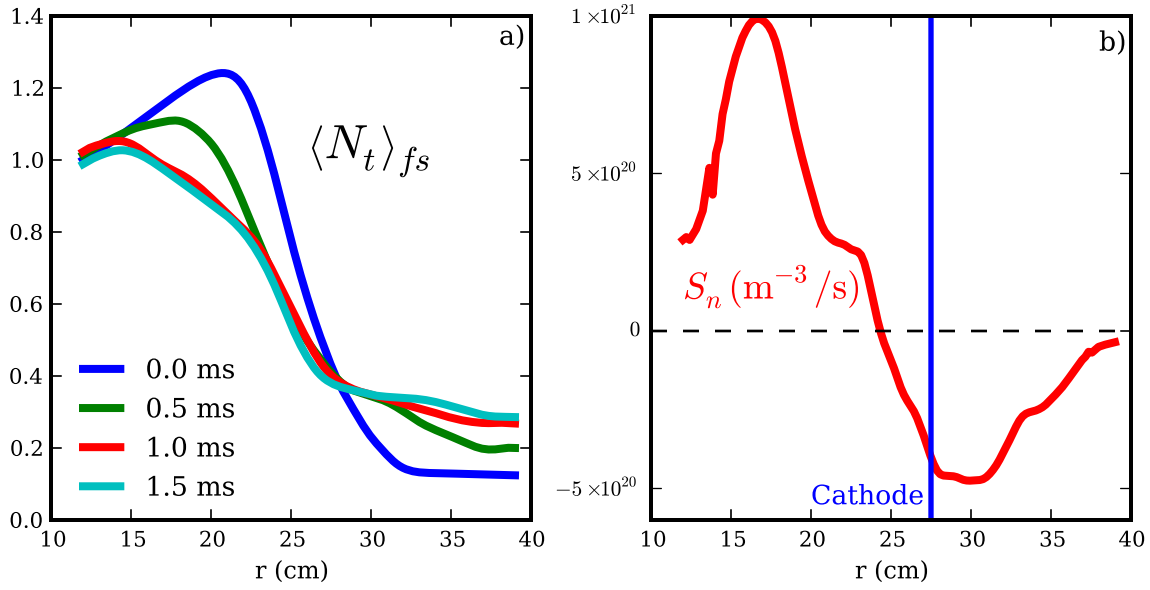

Figure 4.1: a) Profile relaxation and b) evolved density source

$$S_n(t) = -\int_0^t \langle N(\tau)\rangle_{fs}\, d\tau. \tag{4.6}$$

A typical time-averaged density source is shown in Fig. 4.1 b). The upshot of using such a source is that $\langle N_t(t)\rangle_{fs} \simeq N_0$. Notice that the source in Fig. 4.1 b) is net positive inside of the cathode radius and negative outside of it, just as one would expect. I use the same method for the temperature source. The temperature source ultimately comes from the hot electrons that are boiled off of the cathode, which transfer their energy to the plasma through ionizing collisions. This heat transfer is mostly to the electrons of the plasma. The temperature sink is caused by collisions with ions and neutrals which line radiate and by heat loss to the sheath and end walls.

I emphasize that the sources are not first principle sources. They are constructed based on the simulated radial transport. The alternative first principle's approach was used by Rogers and Ricci for LAPD [RR10]. They use a stationary

top-hat-like ionization source that models the physical density-producing process in LAPD. Furthermore, they do not separate equilibrium from fluctuations or input equilibrium profiles. Their source feeds the density, which then transports itself until it comes to a quasi-equilibrium state (a sink is also present). This method solves for the full plasma state with very little experimental input. They input the sources and derive the plasma state. On the other hand, I input part of the plasma state and derive the sources. As stated before, our method has the advantage of using experimentally measured profiles. This experimental input allows us to more easily simulate turbulence that resembles that in the experiment, and therefore make conclusions on the fluctuation properties. I do not, however, evolve the equilibrium and gain the knowledge that comes from that.

4.1.2 Artificial Diffusion and Viscosity

Artificial diffusion or hyperdiffusion terms are ubiquitous in fluid simulations. They are generally intended to prevent high frequency or high wavenumber ringing caused by numerical advection schemes at steep interfaces. They can, however, cause unphysical smoothing in systems that are non-diffusive and non-viscous or cause over-smoothing if applied haphazardly. Some numerical advection schemes contain their own diffusion, called numerical diffusion. Other non-advective finite difference schemes also contain numerical diffusion or dispersion.

I use artificial diffusion and viscosity for several reasons. The first is to prevent artificial high-wavenumber oscillations due to the Arakawa advection scheme that I use [Ara66]. Second, it smooths out the solutions, preventing the total density and temperature from becoming negative at any point in space, which is obviously unphysical. Third, I can use it to prevent the need to go to very fine grid spacing at which physical diffusion and viscosity are important. Finally, I can use it to help saturate the turbulence at levels consistent with experiment. These reasons are all somewhat related, and I note that I performed an artificial diffusion and

viscosity sensitivity study in Ref. [FUC12].

Diffusion and viscosity are real effects that are present in the non-reduced Braginskii equations. In Chapter 3, I made the approximation that $\nabla \cdot (n\mathbf{v}_{\perp e}) = \mathbf{v}_E \cdot \nabla n$, which neglected the polarization velocity part of $\mathbf{v}_{\perp e}$. Now the "full polarization velocity" [SC03] (from crossing Eq. 3.3 with $\mathbf{b}$ and neglecting the stress tensor) is

$$\mathbf{v}_{pe} = (1/\omega_{ce}) \left[\frac{d(\mathbf{b} \times \mathbf{v}_{\perp e})}{dt} + \nu_e \mathbf{b} \times \mathbf{v}_{\perp e} - \nu_e \mathbf{b} \times \mathbf{v}_{\perp i} - \frac{3}{2} \frac{\nu_e}{m_e \omega_{ce}} \nabla_\perp T_e \right]. \quad (4.7)$$

The part of this that causes collisional diffusive terms is $(\nu_e/\omega_{ce})\mathbf{b} \times \mathbf{v}_{\perp e}$. Now this contains $\mathbf{v}_{\perp e}$ itself, which must be approximated as $\mathbf{v}_{\perp e} = \mathbf{v}_E + \mathbf{v}_{de}$ to allow for closure. Only the diamagnetic drift part will be important for the collisional diffusion, so the part of the polarization velocity that I focus on is $(\nu_e/\omega_{ce})\mathbf{b} \times \mathbf{v}_{de}$. Recall that I want to use this in the continuity equation, so I am interested in the term $\nabla \cdot (n_e v_e) \rightarrow \nabla \cdot (n_e(\nu_e/\omega_{ce})\mathbf{b} \times \mathbf{v}_{de}) = -\nabla \cdot \frac{\nu_e m_e}{e^2 B^2} \nabla_\perp p_e$. Now defining $D = \frac{\nu_e m_e T_e}{e^2 B^2}$, I have $\nabla \cdot (n_e v_e) = -\nabla \cdot (D \nabla_\perp n)+$ lots of other terms. D is the classical diffusion coefficient, which is about $0.01\text{m}^2/\text{s}$ for LAPD parameters. One of the terms in $\nabla \cdot (D\nabla_\perp n)$ is $D\nabla_\perp^2 n$, which has the same form of the artificial diffusion term that I've added to Eq. 4.1. Of course, I have neglected many terms of the same order as this term in Eq. 4.1, but this shows that such a classical diffusion term is present in the Braginskii equations.

A similar treatment can be used for the energy conservation equation (Eq. 3.6), using the same procedure as for the continuity equation but with the $p_e \nabla \cdot \mathbf{v}_e$ term in Eq. 3.6. The result is $p_e \nabla \cdot \mathbf{v}_e = D n_e \nabla_\perp^2 T_e +$ lots of other terms. This has the same form as the temperature diffusion term in Eq. 4.4.

The viscosity in the vorticity equation comes from the ion stress tensor term $\frac{\partial \Pi_{i\alpha\beta}}{\partial x_\beta}$ that I neglected when deriving the vorticity equation because I neglected everything with finite ion temperature. If this was included, a vorticity diffusion

term (aka a viscosity) would have been included in the vorticity equation [PUC10b] as it is in other equation sets like the well-known Hasagawa-Wakatani equations [HW83]. The magnetized Braginskii viscosity coefficient is $\eta_1^i = \frac{3nT_i}{10\omega_{ci}^2\tau_i}$, which is about $2 \times 10^{-8}\text{kg/m} \cdot \text{s}$ for LAPD. Since LAPD's ions are not necessarily magnetized due to the fact that $\omega_{ci}\tau_i \sim 1$, the unmagnetized ion viscosity is $\eta_0^i = 0.96nT_i\tau_i$ [Bra65] which is about $4 \times 10^{-7}\text{kg/m} \cdot \text{s}$.

For the artificial diffusion and viscosity coefficients in Eqs. 4.1-4.4, I use a single value of 1.25×10^{-3} in our normalized units, which is $0.075\text{m}^2/\text{s}$ in real units. I find that this value produces turbulent fluctuation levels consistent with experimental levels. I use this as a free parameter in this sense. This value is much larger than the real classical diffusion D, but is smaller than $\frac{\eta_1^i}{nm_i} = 1\text{m}^2/\text{s}$. Nevertheless, I neglected a number of terms in Eqs. 4.1-4.4 such that there isn't justification to use the real diffusion and viscosity in these equations. Artificial diffusion and viscosity terms, however, serve a numerical purpose.

4.2 Boundary Conditions

Boundary conditions are often difficult to determine in plasma devices. While the properties of the boundaries are usually known, the way that the plasma interacts with them can be complex. Plasma boundary physics is one of the main elements of present day fusion research [Sta00]. Often times there is uncertainty in the equations that need to be used in simulations, and once the equations are found, they can be difficult to implement in codes.

The boundary conditions in LAPD are difficult to determine. LAPD contains at one end, a hot emitting cathode behind a biased mesh annode. In front of the annode are biasable azimuthal limiters with radius about equal to the cathode radius, though the limiter radius may be changed. The far end contains a floating mesh plate. The cylinder is conducting and has a radius about 20 cm larger than

the cathode radius.

4.2.1 Simple Boundaries

In all simulations, I use an annulus rather than a cylinder. Although the inner radius of the annulus may be arbitrarily small, I take the inner radius to be 12 cm. I take the outer radius to be 39 cm. This is generally the radial extent of our experimental probe measurements. Furthermore, the plasma fluctuations are nearly zero (when normalized to values at the cylindrical axis) outside of this annular region, which is seen in Fig. 3.1 c). Therefore, I set the radial boundaries on all of the fluctuating variables ($N, \phi, v_{\parallel e}$, andT_e) to zero. It would be nice in the future to take data spanning at least a few more cm and extend the simulation domain accordingly. But for now, the results use such an annular domain.

As for the axial boundaries, I use four different boundary conditions: periodic, zero-value (Dirichlet), zero-derivative (Neumann), and Bohm sheath. The only non-trivial one, Bohm sheath, is derived and described in the following subsection. The others are all trivial to implement and provide a test of the importance of the axial boundary conditions on the nature of the turbulence.

4.2.2 Bohm Sheath Boundaries

Bohm sheath boundary conditions are applicable when a plasma terminates at a conducting plate. I note that this is not necessarily the case in LAPD. The cathode/annode system is obviously much different from a simple floating or biased conducting plate. Furthermore, the mesh wall at the far end is not a solid wall. Moreover, it's not clear if the plasma is even attached to the far end mesh wall or if it becomes detached in the neutrals in front of it, where the plasma cools and recombines before interacting with the wall. In any case, it is still instructive to apply such an idealized boundary condition to LAPD because it is somewhat

more realistic than the simpler boundary conditions, and it creates a new linear instability (see Sec. 5.1.2), which can be used to test the robustness of LAPD's nonlinear instability. Therefore, I proceed with the derivation of the Bohm sheath boundary conditions.

Now, it is known that to good approximation, a plasma bounded by a wall can be divided into two regions: the main plasma and the Debye sheath [Sta00]. The Debye sheath is a small region adjacent to the wall, generally several Debye lengths long. It has a net positive charge ($n_i > n_e$) that shields the negative charge on the wall. The sheath does not completely shield the negative wall, however, and a small electric field penetrates into the main plasma (the ambipolar field), which mostly serves to accelerate the cold ions toward the wall, and slightly retard the electrons before entering the sheath. In the main plasma, the quasi-neutrality relation holds ($n_i = n_e$).

The well-known Bohm criterion along with other considerations restricts the ions to move into the sheath entrance at the sound speed $c_s = \sqrt{T_e/m_i}$. I consider here the case where there is no external biasing; in other words, the end plates are electrically isolated and floating. The wall can be set to an arbitrary potential, say $\phi_w = 0$, while the potential at the sheath entrance is then the positive floating potential ϕ_{sf}. This potential difference across the sheath reflects slow electrons that enter the sheath. The electrons approximately maintain a cutoff Maxwellian velocity distrubution throughout the sheath, and at the wall, their velocity is retarded by a Boltzmann factor due to the floating potential. In total, the current to the wall is [BRT91, BCR93, XRD93]

$$J_\parallel = \pm en \left[c_s - \frac{(T_e/m_e)^{1/2}}{2\sqrt{\pi}} e^{\left(-\frac{e\phi_{sf}}{T_e}\right)} \right], \tag{4.8}$$

where the $\pm$ indicates that the plasma flux goes into the wall, which is in different directions for the different end plates. Note that there is a factor of

$\sqrt{2}$ discrepancy between different reports on the expression used for the thermal velocity, which should have only a minor consequence. In this expression, all values are total (equilibrium + fluctuations).

Now, this is not only the current to the wall, but also the current going into the sheath edge, since the sheath is too small for there to be appreciable radial current loss or an ionization source within the sheath. All values, in fact, are taken to be those at the sheath edge. Furthermore, since the wall is electrically isolated, the equilibrium current at the wall vanishes. This sets the value for the floating potential to be $\phi_{sf} = \Lambda T_{e0}/e$ with $\Lambda = \ln\left(\frac{1}{2\sqrt{\pi}}\sqrt{\frac{m_i}{m_e}}\right)$. Note that T_{e0} is a function of radius, meaning ϕ_{sf} is also a function of radius. Thus, a radial temperature gradient produces a radial electric field, at least at the sheath edge and likely penetrating axially into the main plasma. It is noted that $J_\parallel$ need not vanish on every field line since the end plates are conducting and charges can move around on the plate, however, the vanishing equilibrium current is generally a fair approximation [BCR93].

On the other hand, the fluctuating component of the current is allowed to vary between field lines. The first order fluctuating component is obtained by linearizing Eq. 4.8, giving the result:

$$J_\parallel = \pm e N_0 c_{s0} \left[\frac{e\phi}{T_{e0}} - \Lambda \frac{T_e}{T_{e0}}\right], \tag{4.9}$$

where now, $J_\parallel, \phi$ and T_e are fluctuating components, consistent with previous notation. This expression for the current sets the fluctuating axial boundary condition of the plasma and is often called the Bohm Sheath boundary condition. This current condition holds both at the wall and at the sheath entrance. So rather than taking the simulation domain all the way to the wall, simulations often end at the sheath entrance and employ this analytically derived boundary condition to the boundaries of the main plasma. Then one doesn't have to worry

about the small spatial scales and the non-quasineutrality of the sheath. The corresponding boundary conditions for the other fluid variables such as the density and temperature have recently been derived by Loizu et al. [LRH12]. However, I simply take them to have zero-gradient as most others have done, although this isn't wholly inconsistent with Loizu's calculations.

Now while one may set the parallel current (or equivalently $v_{\|e}$) at the axial boundaries to the quantity on the right hand side of Eq. 4.9, I don't do that. I use Ohm's Law ($-\nabla_\| \phi = \eta_\| J_\|$) to set the boundary condition for the gradient of ϕ. I do this for practical reasons in the coding. Therefore, the boundary condition used in the code is (in our normalized units):

$$\nabla_\| \phi = \pm \frac{\nu_e m_e}{m_i} \left(\phi - \Lambda T_e\right). \tag{4.10}$$

4.3 Profiles and Parameters

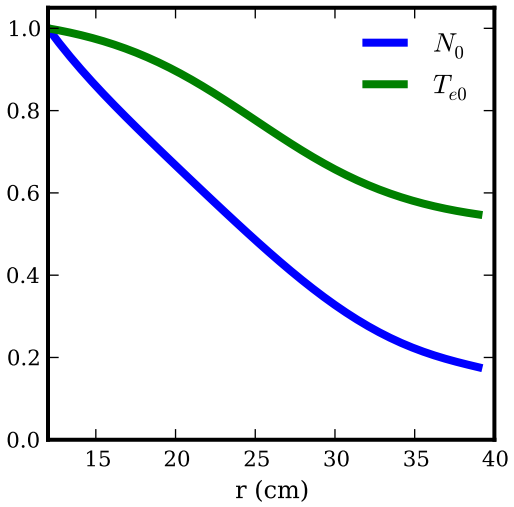

Figure 4.2: Equilibrium density and electron temperature profiles

As explained above, I take all equilibrium profiles and parameters from ex-

perimental measurements. All simulations before Chapter 9 use profiles and parameters from one particular experiment. This experiment used limiter biasing to essentially null out the mean radial electric field [SCR12]. I used this experiment so that I could neglect the mean potential profile in the equations (as is done in Eqs. 4.1-4.4), which simplifies our analysis. The normalized profiles that I use are shown in Fig. 4.2, and the parameters are shown in Table 4.3. The density profile is a polynomial fit to the experimental equilibrium density profile. The temperature profile is a tanh function that somewhat resembles typical LAPD temperature profiles. At the time of the first simulations, I didn't have reliable temperature profile measurements, so I was forced to estimate what the profile might look like. I note that the real temperature profile has a steeper gradient than the one I use. And again, I use $\phi_0 = 0$, which is a good approximation for the experimental nulled out potential profile.

The profiles that I use have no azimuthal or axial variation because I don't have the corresponding experimental measurements. So I assume that the equilibrium profiles are only functions of radius. It's likely, however, that there is some axial variation in the profiles and parameters. In LAPD, $\nu^* \equiv L_\parallel/\lambda_{ei} \sim 100$, generally indicating that a parallel temperature gradient can exist depending on the locations of the sources and sinks [Sta00]. Furthermore, if the Bohm sheath boundary condition is correct, the equilibrium potential must have a parallel gradient in order to accelerate the ions up to the sound speed at the sheath entrance. This ambipolar parallel electric field should exist between the location of the sheath entrance and an ion collision length into the main plasma. The parallel electric field generated by the condition of Eq. 4.10 is just the perturbed field that responds to electron temperature perturbations. It doesn't constitute the equilibrium electric field.

Moreover, recall that the Bohm sheath condition combined with a radial equilibrium electron temperature profile implies (at least near the sheath) a corre-

sponding equilibrium potential profile, since $\phi_{sf} = \Lambda T_{e0}/e$. Experimentally, this relation doesn't hold where the plasma is measured, meaning that either the ambipolar field doesn't penetrate far into the plasma or that the real LAPD boundary conditions are more complicated than simple floating conducting plates. So I don't use any equilibrium axial variation, leaving this to future work.

Species	^{4}He
Z	1
n	2.86×10^{18} m^{-3}
T_e	6 eV
T_i	$\lesssim 1$ eV
B_0	0.1 T
$L_\parallel$	17 m
a	0.4 m
λ_D	10^{-5} m
ω_{ci}	2.4×10^6 rad/s
ω_{ce}	1.8×10^{10} rad/s
ρ_e	5.3×10^{-5} m
ρ_i	$\sim 1 \times 10^{-3}$ m
ρ_s	5×10^{-3} m
v_{te}	9.4×10^5 m/s
c_s	1.1×10^4 m/s
v_A	7×10^5 m/s
β	5×10^{-4}
m_e/m_i	1.4×10^{-4}
$\ln\Lambda$	11
ν_e	7.2×10^6 Hz
λ_{ei}	0.13 m
ν_i	$\sim 10^6$ Hz
ν_{in}	3×10^3 Hz
$\kappa_\parallel^e$	9.8×10^{23} eV/m^2 s
η_0^i	$\sim 10^{12}$ eV s/m^3
ω_*	$\sim 5 \times 10^4$ rad/s

Table 4.1: LAPD simulation parameters

CHAPTER 5

The Nature of LAPD Turbulence

Simulations can supplement experiment by providing detailed spatial data that is too difficult to obtain experimentally. This spatial data can be analyzed, revealing new properties of the experiment. In order for simulations to provide information, however, they must accurately represent the system which they model. Assessing the validity of simulations generally comes in two parts: verification and validation. Verification, the evidence that the code solves the equations correctly, will not be taken up here. I note, however, that my collaborators and I have done verification studies in the past, somewhat detailed in Popovich et al. [PUC10a]. We compared linear BOUT (the old version of BOUT++) and BOUT++ simulations to analytic solutions as well as to eigensystem solver solutions. On the other hand, I will focus parts of this chapter on our validation effort. Validation is the evidence that the simulation model accurately reproduces features of the experiment. Generally, the more features of the experiment that the model reproduces, the more valid the model. While this chapter focuses on simple analyses to describe the nature of the simulated turbulence, it will also make comparisons, where possible, to experimental data in order to show that the model is relatively well validated. First, however, I analyze the linear instabilities in the LAPD simulations, and this affords no experimental comparison.

5.1 LAPD Linear Instabilities

Linear instabilities are prevalent in plasma physics. They come from the linearization around an equilibrium of the plasma equations. Physically, if a plasma is in a time-independent steady state that is linearly unstable and a finite fluctuation of any size occurs, the fluctuation will grow exponentially. Linear instabilities often drive hydrodynamic and plasma turbulence. I therefore study the linear instabilities of the LAPD system before moving onto the turbulence because they can offer insight into the nature of the turbulence. The LAPD equations, parameters, and profiles described in Chapter 4 give rise to a couple of linear instabilities. They are both drift wave type instabilities, but they have different pressure/potential coupling mechanisms. One type couples through the adiabatic response, while the other couples through the sheath boundary response.

5.1.1 Drift Waves

Electron drift waves driven by an equilibrium density or pressure gradient that use the adiabatic response are generally referred to as just drift waves or the universal instability. The electron drift wave mechanism is the following: An electron pressure fluctuation in the plasma is linked with a potential fluctuation through the adiabatic response. The adiabatic response is simply a parallel force balance between the pressure force and the electrostatic force. A simplified version of Eq. 3.3 can be written:

$$\nabla_{\parallel} p_e = en\nabla_{\parallel}\phi + Rv_{\parallel e}, \tag{5.1}$$

where the term $Rv_{\parallel e}$ represents effects such as electron inertia, resistivity, and electromagnetic induction. If $R = 0$, the electrons are said to be adiabatic, meaning $\nabla_{\parallel} p_e = en\nabla_{\parallel}\phi$. When T_e fluctuations are neglected and $\nabla_{\parallel} \neq 0$, this integrates to the Boltzmann expression:

$$n = n_0 e^{e\phi/T_e}. \tag{5.2}$$

For any R and T_e fluctuations, the parallel electron dynamics couple the pressure to the potential as long as the parallel wavelength $k_\parallel$ is finite. The perpendicular electric field associated with the potential fluctuation has a component in the azimuthal direction with $k_\perp \gg k_\parallel$. This creates a radial $\mathbf{E} \times \mathbf{B}$ drift that advects the pressure in the radial direction. Because of the radial pressure gradient, the fluctuation to propagates azimuthally as a wave at the drift speed $v_{De} = \frac{T_e}{eB}\frac{\partial \ln N_0}{\partial r}$ [Che06] in the electron diamagnetic drift direction. If there is a small phase difference between the pressure and the potential of the wave (the result of $R \neq 0$), the equilibrium pressure gradient will enhance the fluctuation, causing instability. Since $p_e = n_e T_e$, the pressure fluctuation may be due to either a density fluctuation, an electron temperature fluctuation, or both. The universal instability generally refers to the situation where an equilibrium density gradient drives a density fluctuating wave. But a temperature gradient driving a temperature fluctuation wave is also possible, and may be called a thermal drift wave [MTK11]. It's not necessary, however, to separate them, and I will just refer to both of these as drift waves.

The LAPD equation set (Eqs. 4.1-4.4) supports such drift waves, which are unstable with the parameters and profiles used in the simulations. The growth rate as a function of the azimuthal wavenumber m is shown in Fig. 5.1 a) for the LAPD parameters in Table 4.3 and profiles in Fig. 4.2. The growth rates are found by simulating the linearized version of Eqs. 4.1-4.4 in BOUT++ with the three different simple axial boundary conditions: periodic, zero-value (Dirichlet), and zero-derivative (Neumann). The linear equations simply omit the advective nonlinearities and the source terms, though the source terms have no affect on any of the linear modes besides $m = 0$ modes. The simulations are run for long enough so that the fastest growing modes can dominate the dynamics.

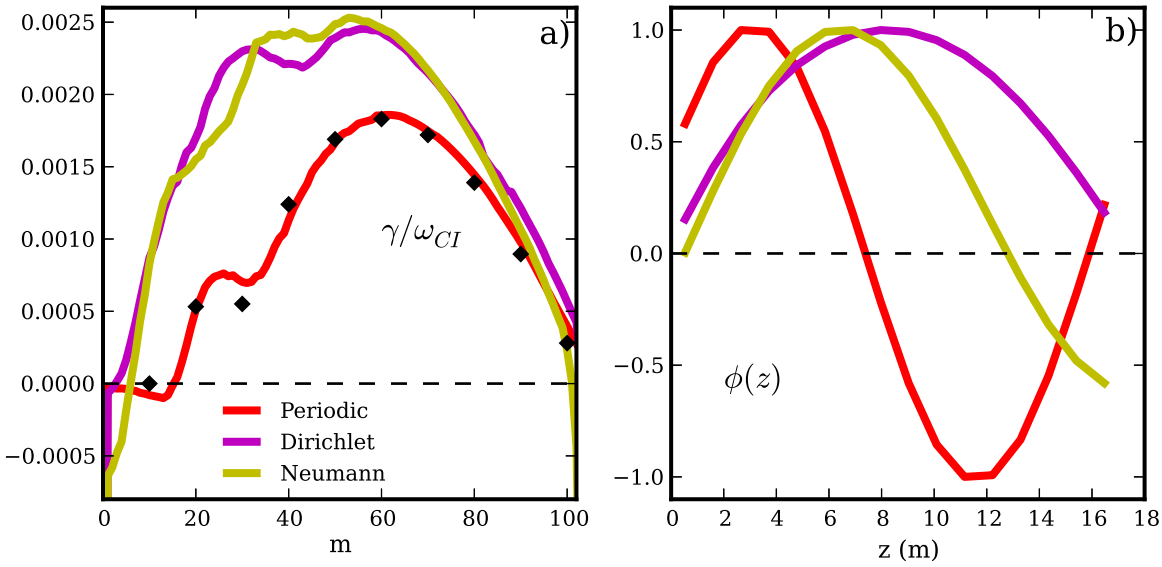

Figure 5.1: Linear drift wave a) growth rates and b) axial structures

The solid curves in Fig. 5.1 are calculated from the simulation results using the formula, $\gamma_m = \frac{\partial E_m}{\partial t}/(2E_m)$ where E_m is the energy of the fastest growing linear eigenmode with azimuthal mode number m. The energy is defined in Chapter 6. The details of obtaining γ_m are explained in that chapter, but for now, it is sufficient to state that this procedure calculates γ_m at a particular time using only the structures of the fluctuating quantities: $N, \phi, v_{\|e}, \text{and} T_e$. An alternative way to calculate γ_m is to use BOUT++'s Fourier filtering capabilities and run many simulations where each one filters out a different azimuthal mode. Then, I take the log of the envelope of one or several of the fluctuating quantities and calculate the slope of the line, which gives the growth rate for each particular simulation. This procedure uses the time signal of the fluctuations rather than their spatial structure to calculate the growth rate, thus providing a check on the first method. The results using this alternative method for the periodic case are shown with the black diamonds in Fig. 5.1 a), which agree well with the curve calculated using the alternative energetic structure-based calculation. I do this

check with all of the simulations to ensure consistency. This second method is more time consuming, so I only sample a few values of m. Furthermore, it's difficult to get growth rates when $\gamma_m < 0$ using this second method.

The difference in the growth rate curves with the different boundary conditions is due to the different $k_\parallel = \frac{2\pi n}{L_\parallel}$ where n is the axial mode number. The periodic simulation restricts n to integer values, while the Dirichlet and Neumann simulations allow for any fractional n. The largest growth rate occurs for $n \sim 1/2$. The Dirichlet and Neumann axial structures for the most unstable m mode, shown in Fig. 5.1 b), reflect this. The periodic simulation, which has $n = 1$ structure, has a smaller growth rate, especially at low m. Note that in Fig. 5.1 b), the axial boundaries are not plotted. For instance, the zero-valued boundaries for the Dirichlet simulation are not shown. Also, the axial structures are taken at one random point in the $r - \theta$ plane and at one time point, and are normalized to their maximum value.

5.1.2 Conducting Wall Mode

I now consider the linear instability that can exist in a plasma bounded by two conducting walls on the boundaries where the magnetic field lines terminate (the axial boundaries) [BRT91, BCR93, XRD93]. The instability is actually of the drift wave variety, but unlike the drift waves discussed above, the pressure-potential coupling mechanism is through the sheath boundary response rather than through the adiabatic response. The Bohm sheath boundary conditions that were derived in Sec. 4.2.2 can provide this coupling. As already noted, these boundary conditions are not necessarily the correct ones for LAPD, but are somewhat idealized. Yet, it is still academically instructive to apply such an idealized boundary condition to LAPD because it creates this new linear instability, which can be used to test the robustness of LAPD's nonlinear instability.

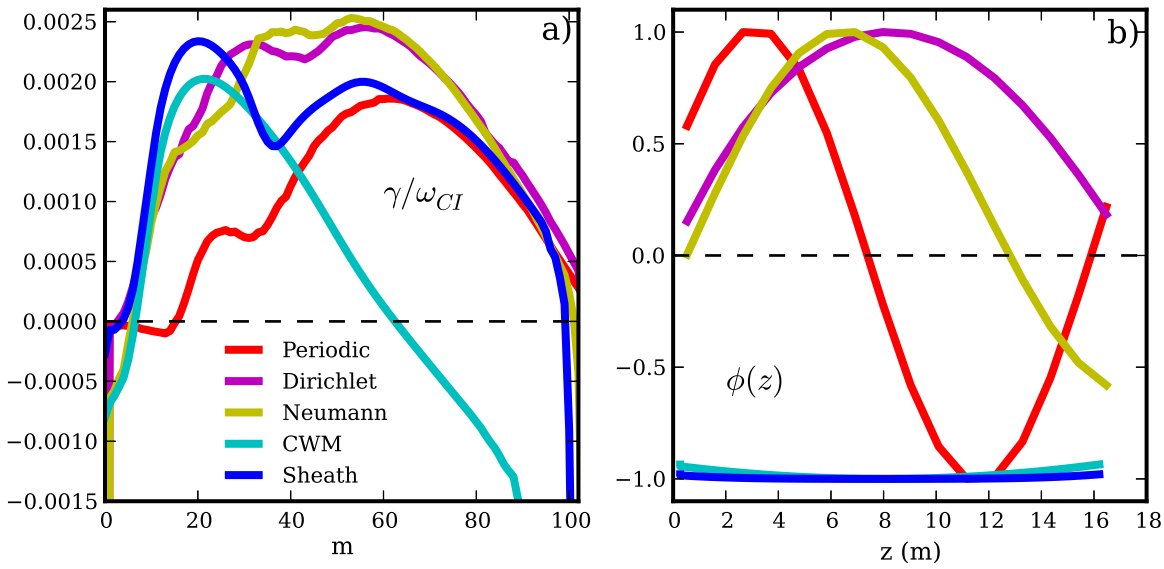

Figure 5.2: Linear conducting wall mode a) growth rates and b) axial structures

The conducting wall mode (CWM) instability in the case considered here is purely an electron temperature gradient instability, although other types of gradients can cause it [BCR93]. Electron temperature fluctuations are advected by electrostatic potential fluctuations and feed off the equilibrium electron temperature gradient as in the case of the thermal drift waves. However, in contrast to the thermal drift waves, the coupling between the temperature and potential fluctuations comes through the sheath boundary condition rather than through the adiabatic response. Furthermore, the CWM can have (nearly) $k_{\|} = 0$ flute-like behavior. The coupling mechanism is as follows: an electron temperature perturbation – say a positive constant fluctuation along a small flux tube – increases the sound speed and the electron thermal speed on the flux tube. Since the ions must enter the Bohm sheath at the sound speed by being accelerated by a parallel electric field, the temperature increase must coincide with an increase in the parallel potential gradient as derived in Eq. 4.10. Additionally, the increased electron thermal speed causes an increase in the floating potential along the flux

tube. These serve to couple the electron temperature to the potential.

The CWM can be isolated from the normal drift waves by removing the adiabatic response from the full LAPD equation set, and of course using the Bohm sheath boundary condition of Eq. 4.10. Removal of the adiabatic response in this case means removal of the $\nabla_\parallel p_e$ and the $0.71\nabla_\parallel T_e$ terms in the parallel momentum equation (Eq. 4.2). This causes the density fluctuation N to become a passive scalar, so Eq. 4.1 can be removed as well with no consequence. So the isolated linear CWM equations are:

$$\partial_t v_{\parallel e} = \frac{m_i}{m_e}\nabla_\parallel \phi - \nu_e v_{\parallel e}, \tag{5.3}$$

$$\partial_t \varpi = -N_0 \nabla_\parallel v_{\parallel e} - \nu_{in}\varpi + \mu_\phi \nabla_\perp^2 \varpi, \tag{5.4}$$

$$\partial_t T_e = -\mathbf{v_E}\cdot\nabla T_{e0} + \frac{2}{3N_0}\kappa_{\parallel e}\nabla_\parallel^2 T_e - \frac{2m_e}{m_i}\nu_e T_e + \mu_T \nabla_\perp^2 T_e, \tag{5.5}$$

The CWM growth rate curve is shown in Fig. 5.2 a). The CWM is most unstable at values of $m \sim 20$, which is much lower than the $m \sim 60$ values of the drift waves. Furthermore, the CWM maximum growth rate is about equal to the drift wave growth rates. And from Fig. 5.2 b), the CWM axial structure is flute-like ($k_\parallel \simeq 0$). Finally, the growth rate curve of the full set of equations along with the sheath boundary condition is shown in this figure as the curve labeled "sheath." This set of equations contains the drift wave and CWM instabilities. From both Figs. 5.2 a) and b), it is clear that the sheath simulation is dominated by the CWM at $m \leq 20$, which in fact is where the growth rate is maximum. At $m \geq 40$, the drift waves dominate.

5.2 LAPD Turbulence: A Visual Examination

When I simulate the full LAPD equation set with the advective nonlinearities and source terms, I find that the simulation develops into a turbulent state. To

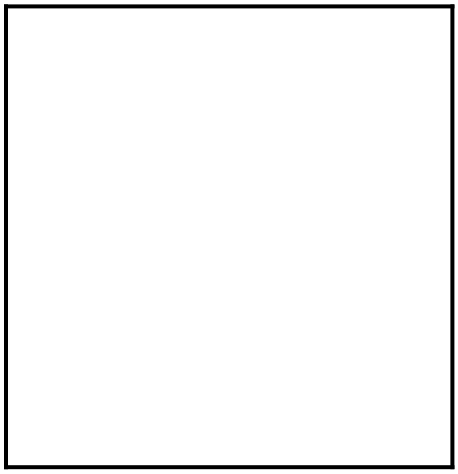

Figure 5.3: 3D turbulent simulation animation

start the simulation, I initialize each fluctuation quantity ($N, \phi, v_{\parallel e}$, and T_e) with a small random 3D spatial structure. The structure evolves and a coherent structure emerges (the fastest growing linear eigenvector), which grows exponentially in time. Once the normalized fluctuations reach values on the order of $0.01-0.1$, they saturate and appear to be turbulent. A 3D animation of the density fluctuation N is shown in Fig. 5.3. The animation shows a 1/8th wedge of the simulated annulus to make the axial extent of the annulus visible. The animation begins right before the fastest growing mode structure becomes dominant. The fastest growing mode dominates the structure for some time, where there is a clear coherent wave structure that simply propagates in the electron diamagnetic drift direction. This stage is called the linear stage since the linear terms in the equations dominate the evolution. Note that the axial structure in the linear stage has a finite wavelength about half of the length of the animation domain. The axial boundary conditions used here (Neumann) allow for such a structure.

Soon, the coherent eigenmode structure, which has been growing in magnitude, saturates and transitions to a turbulent-looking state that I call the turbulent

stage. The evolution of the RMS fluctuation amplitude of the density and potential is shown in Fig. 5.4 a). The potential is separated into a flux-surface-averaged component ϕ_{fs} and the remainder $\phi - \phi_{fs}$. ϕ_{fs} quantifies the amplitude in the zonal flow, which appears in Fig. 5.4 a) to possibly have some role in the initial saturation, but has a relatively small magnitude in the turbulent stage. For all the fluctuations, the exponential growth period during the linear stage is followed by saturation corresponding to the visual change from coherent to turbulent spatial structures in the animation. Upon transition to the turbulent stage, I notice in the animation that there is also a qualitative change in the axial mode structure. The axial structures elongate, looking more flute-like than in the linear stage. I confirm this by taking the axial Fourier transform of the density fluctuations and plotting the RMS values of the different axial mode numbers in Fig. 5.4 b). The linear stage is dominated by the $n = 1$ Fourier component, while the turbulent stage is dominated by the $n = 0$ flute mode component. I found this to be an interesting and unexpected transition when I first identified it. There is not only the expected bifurcation from linear waves to turbulence, but also the unexpected bifurcation from linear drift wave structures to turblent flute-like structures. I will discuss why this is unexpected in the upcoming chapters, and I will show in detail what causes it. But take note that this is a key finding. This $n = 0$ dominance in the turbulent stage is the main subject of the remaining chapters.

However, before I jump into the analysis of the $n = 0$ mode dominance, I continue to look at simple and common turbulence analysis techniques to describe the nature of the turbulence and to validate the simulations. Continuing on with the visual examination, I show one visual comparison between the simulation and experiment. For the experimental visual, I use a processed fast camera movie. The camera records the light intensity given off by the plasma. The light is primarily due to line radiation of the helium atoms and ions. It should be some function of plasma density, neutral density, and plasma temperature. Noting that the

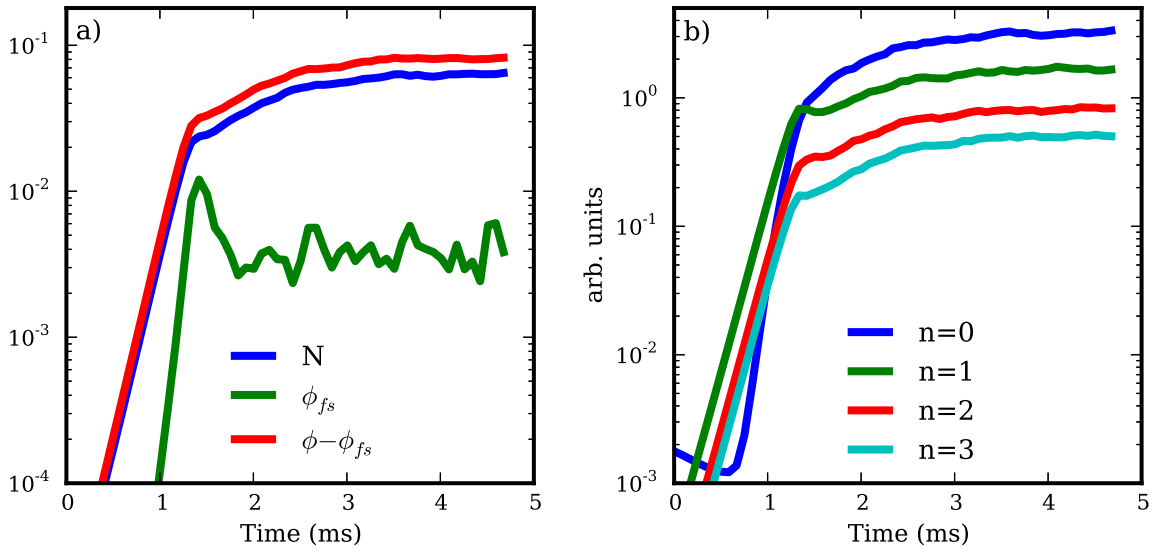

Figure 5.4: RMS time evolution of a) fluctuations and b) axial mode numbers

comparison is certainly not exact, I show the experimental camera data next to corresponding simulation data of the density N signal during the turbulent stage. This is shown in Fig. 5.5. The animations cover the same spatial domain and last for equal time intervals (about 2 ms). Both are simply fluctuation data with the time-independent background not included (subtracted out from the camera data).

Visual comparisons like this are certainly not quantitative, and at best this comparison reveals that both simulatin and experiment appear turbulent and contain similarly sized spatial structures and similar time scales. The camera data can be a valuable tool since it provides so much simultaneous spatial data – something that is difficult to do with probes. Nevertheless, I do not proceed here with detailed statistical analysis of the camera data or any quantitative comparisons between the camera and simulation. This work is left for future studies. Rather, I now focus on statistical analysis of the simulation data, and compare it to experimental Langmuir probe data when possible.

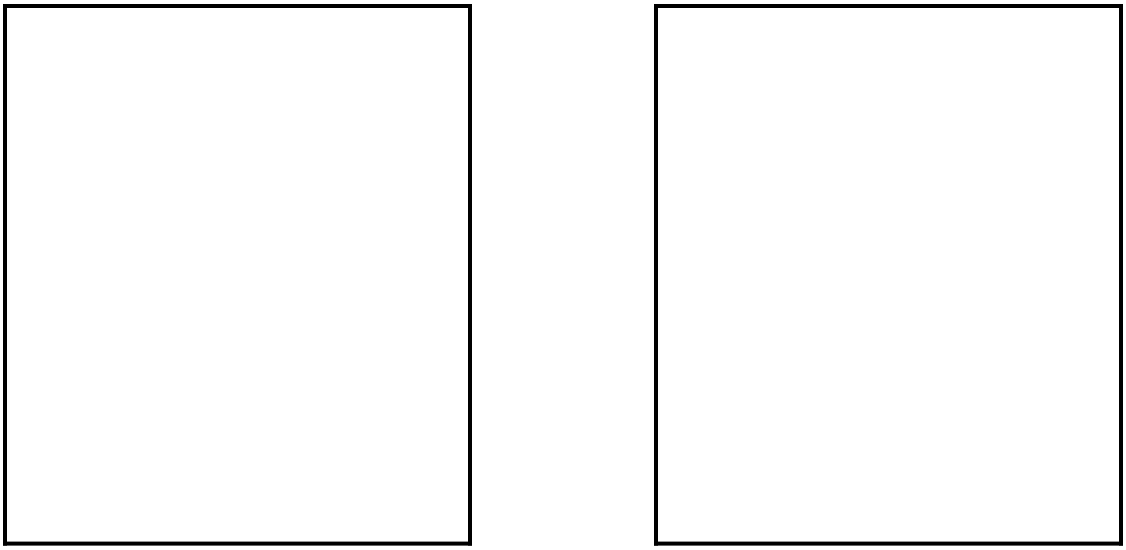

a) Simulation b) Experiment

Figure 5.5: Turbulent movies

5.3 LAPD Turbulence: A Statistical Examination

Dynamical systems are often described statistically using such tools as spectra, pdfs, and spatial and temporal correlations. This is probably the most common way to describe stochastic systems. Recall from Chapter 2 that stochastic systems are those whose temporal autocorrelations decay to zero exponentially fast. I show the temporal autocorrelations of the experiment and a simulation in Fig. 5.6, showing that the autocorrelations recede exponentially (confirmed by a semilog plot), with the simulation having a longer correlation time than the experiment. This is not surprising given the visually longer lived structures in the simulation as seen in Fig. 5.5.

Now before I proceed with more statistical data comparisons to qualify and quantify the agreement between the simulations and experiment, I must first explain how I can extract equivalent information from the simulations and experiment. In general, this hinges upon experimental measurement theory.

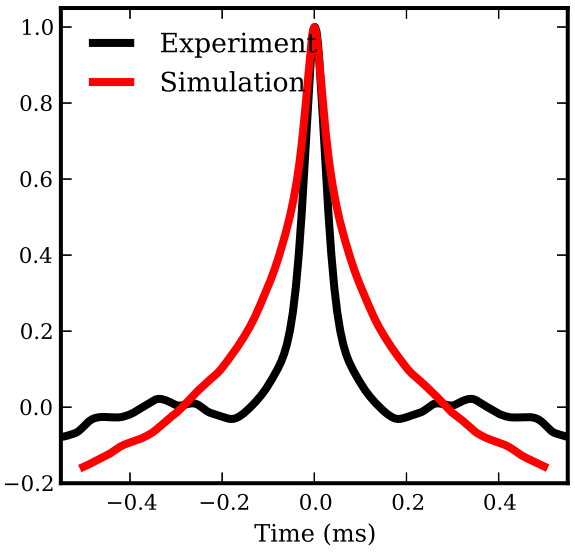

Figure 5.6: Temporal density autocorrelation

5.3.1 Experimental Probe Data

There are many different kinds of experimental measurements, but I focus here only on Langmuir probe measurements. The Langmuir probes in LAPD generally provide time series data although I do have some two-probe data that provides certain spatial information. Langmuir probes do not directly measure any of the independent state or flux variables of the simulation $(N, \phi, v_{\|e}, T_e)$, but they can measure quantities that are functions of these variables. The probes are biased to a known potential (with respect to a reference like the cathode potential), and the current they draw from the plasma is measured. As long as the probes are biased sufficiently below the plasma potential so as to repel most electrons, they develop sheaths around them in the same way as the conducting plates considered in Sec. 4.2.2. The ion current to the probe is [Hut02]

$$I_i \sim \frac{1}{2} e A_s n c_s \tag{5.6}$$

where A_s is the sheath area, approximately equal to the probe area, and the factor of $\frac{1}{2}n$ is the reduction of density at the sheath edge compared to the main plasma. The probe may be biased negatively enough so that all electrons are repelled. The current collected is just that of Eq. 5.6, called the ion saturation current. As the probe voltage is swept positively from this point, more electrons are collected. The total current to the probe then takes the form [Hut02]

$$I = eA_s n c_s \left[\frac{1}{2} - \left(\frac{m_i}{2\pi m_e} \right)^{1/2} e^{eV_p/T_e} \right], \tag{5.7}$$

where V_p (which is negative) is the potential of the probe with respect to the plasma potential. When $I = 0$, the probe potential is at the floating potential: $\frac{e(V_f - \phi)}{T_e} = \frac{1}{2}\ln\left(\frac{\pi m_e}{2m_i}\right)$. The temperature can be obtained by sweeping the probe potential to get $\frac{\partial I}{\partial V_p}$, which is an exponential function of V_p. So the logarithm of this function produces a straight line. Then, the temperature is:

$$T_e = e(I - I_i)/\frac{\partial I}{\partial V_p}. \tag{5.8}$$

Now the sweeping process is too slow to obtain temperature fluctuations. It's best used to obtain the equilibrium temperature profile. Since a single Langmuir probe doesn't give temperature fluctuations, it's impossible to find the exact density and potential fluctuations, N and ϕ. The probes only produce I_{sat} and V_f fluctuation data. Nevertheless, the simulations produce N, ϕ, and T_e fluctuations, which I can use to calculate the I_{sat} and V_f simulation values using the relations: $I_{sat} = \frac{1}{2}eA_s n c_s$ and $V_f = \phi + \frac{T_e}{2e}\ln\left(\frac{\pi m_e}{2m_i}\right)$. So rather than manipulating probe data to find the experimental N and ϕ fluctuations, I can use the simulation data to calculate experimentally-accessable quantities. The derived simulation quantities are called synthetic diagnostics. Synthetic diagnostics are model-dependent and they bind together some of the fundamental underlying data. For instance, two measurements (I_{sat} and V_f) comprise three fundamental state variables (N, ϕ, and

T_e), so the synthetic diagnostics bind the temperature fluctuations to the density and potential fluctuations. Nevertheless, synthetic diagnostics provide a way to make apples-to-apples comparisons between simulation and experimental data.

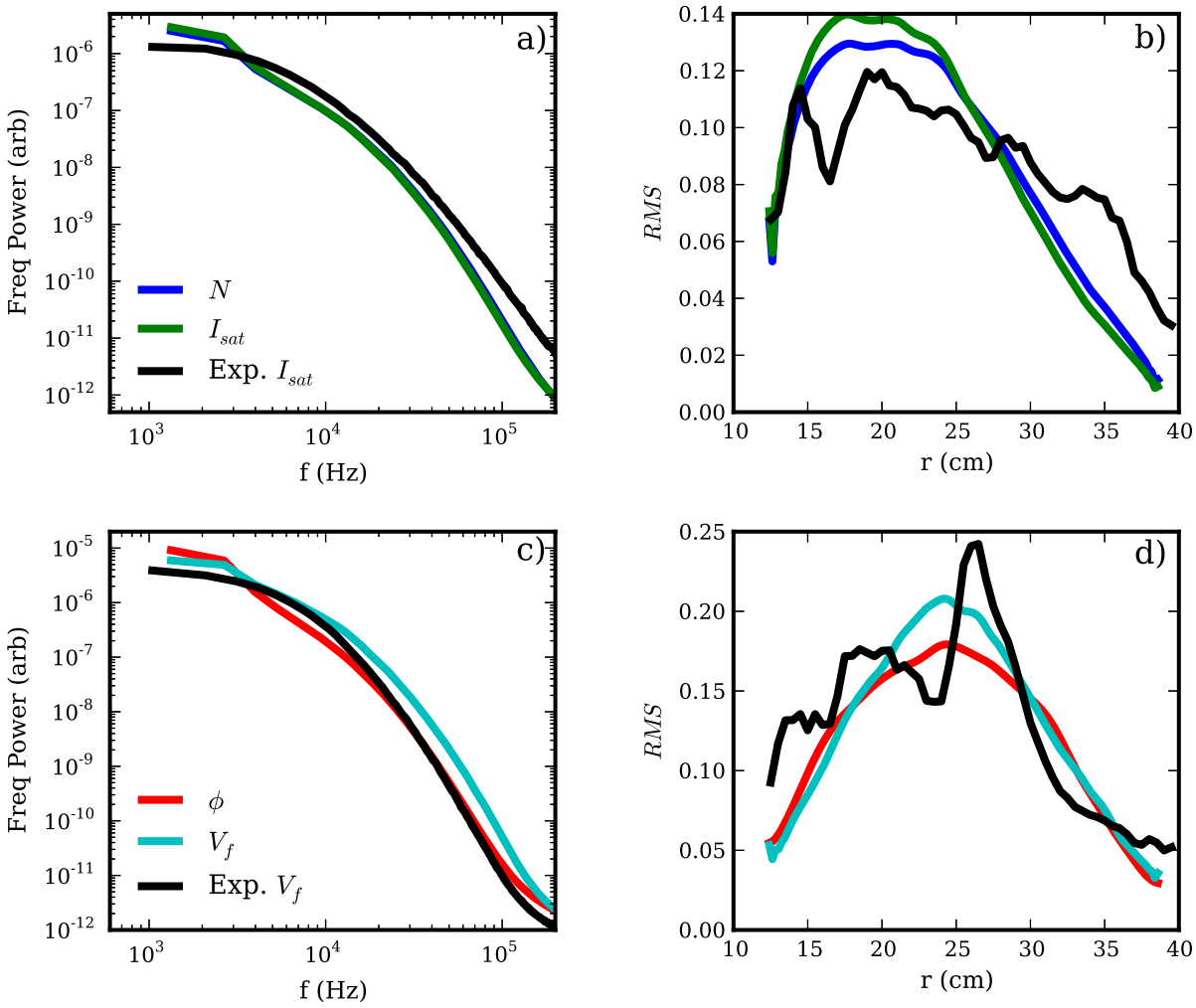

Figure 5.7: I_{sat} and V_f statistical data

I show in Fig. 5.7, a statistical comparison between I_{sat} and V_f fluctuations from simulation and experiment. The simulation uses the full nonlinear equation set along with Bohm sheath axial boundary conditions. I also show simulation

statistics for N and ϕ fluctuations so that they may be compared to the simulation statistics of the synthetic I_{sat} and V_f respectively. Figs. 5.7 a) and b) compare the frequency spectra and radial RMS amplitudes of experimental and simulation I_{sat} fluctuations along with N fluctuations from the simulation. Figs. 5.7 c) and d) compare the same statistical properties, but this time of V_f fluctuations along with ϕ fluctuations from the simulation. The I_{sat} fluctuations from the simulation have nearly identical statistical properties as the N fluctuations because I_{sat} is proportional to density but only weakly dependent on temperature (square root dependence). V_f fluctuations are also somewhat similar to ϕ fluctuations, but to a lesser degree due to the large dependence of T_e on V_f. Furthermore, the simulation and experiment have very similar statistical properties, which I expand upon below.

5.3.2 Statistical Density Comparisons

A comparison of statistical properties of the experimental and simulation density fluctuations is shown in Fig. 5.8. I actually compare the N fluctuations for the simulations to the I_{sat} fluctuations of the experiment, but as seen in Fig. 5.7, I_{sat} and N statistics are nearly identical. Fig. 5.8 contains results from five different simulations that all use the full nonlinear LAPD equation set (Eqs. 4.1-4.4) but differ in the axial boundary conditions as follows: 1) Periodic – uses periodic axial boundary conditions. 2) Sheath – uses Bohm sheath boundary conditions (Eq. 4.10). 3) $n = 0$ suppressed – uses axial boundary conditions, however, the axial average ($k_\parallel$ or $n = 0$) density, temperature, and potential fluctuation components are artifically removed from the simulation. 4) Dirichlet – uses zero-value axial boundary conditions. 5) Neumann – uses zero-first-derivative axial boundary conditions. I will discuss the $n = 0$ suppressed simulation more in Chapter 7, but for now it is sufficient to say that this simulation does not contain the nonlinear instability and is thus a control case by which to compare the others.

It still contains the same linear instabilities as the Periodic simulation, however.

Fig. 5.8 a) shows the frequency power spectrum of the density fluctuations. I use a sliding Hamming window on the time series data and take the FFT, then take a volume average from 15 to 35 cm to get each simulation curve. I use the same technique for the experimental density fluctuation data, except I only have probe data at one location in the $\theta - z$ plane. The axial location is near the center of the machine. Fig. 5.8 b) shows the probability distribution function (PDF) of the density fluctuations, while Fig. 5.8 c) shows the RMS amplitude of the density fluctuations as a function of radius. Fig. 5.8 d) plots the radial k_r power spectrum of the simulations. I don't have experimental radial spectra data, which requires multiple probes at different radii. Fig. 5.8 e) is the azimuthal m_θ power spectra. Two probes separated azimuthally are used to obtain the experimental spectra. Finally Fig. 5.8 f) is the axial $k_\parallel$ spectra, and I don't have experimental axial spectra due to the difficulty of aligning two probes along a field line a significant distance from each other, which is required because of the long axial wavelengths of the modes.

Fig. 5.8 contains a lot of information about the simulations and experiment. The first obvious result is that the $n = 0$ suppressed simulation is statistically much different than all of the other simulations and the experiment. The density fluctuations of this simulation are a factor of 2-3 lower than that of the other simulations and the experiment. Furthermore, this simulation has peaks in the frequency, m_θ, and $k_\parallel$ spectra that are unique. The frequency and m_θ peaks are inconsistent with the experiment. Its spatial spectra peak at $m_\theta \sim 30$ and $k_\parallel \rho_s \sim 0.002 \rightarrow n = 1$, which is somewhat consistent with the linear growth rate spectra of Fig. 5.1, although the m_θ peak location is somewhat less than the maximum linear growth rate value of m_θ, which is around 60 when the axial boundaries are periodic. This differs significantly from all of the other simulations and the experiment which have peaks at $m_\theta \sim 10$ (if they peak at all). And again,

as was clear from Fig. 5.4 b), all of the other simulations are strongly dominated by $n = 0$ axial mode numbers, which will be explained in the upcoming chapters as due to the nonlinear instability.

Moreover, all of the simulations other than the $n = 0$ suppressed simulation have qualitatively and semi-quantitatively similar statistical properties. I note that on a quantitative level, the Dirichlet and Neumann simulations have fluctuation levels about 1.5 times less than the Periodic and Sheath simulations. I don't fully understand the reason for this, but note that the axial wavenumber spectra in Fig. 5.8 f) are shallower for the Dirichlet and Neumann simulations. This certainly affects the energy injection and energy dissipation, as will be seen in the following chapters. Nevertheless, even though their fluctuation levels are too low, I don't claim that the Dirichlet and Neumann simulations are less consistent with the experiment than the Periodic and Sheath simulations. The reason is that I have a free parameter, namely the artificial diffusion coefficient, which affects the overall fluctuation level without significantly affecting the shapes of the spectra. I tuned this parameter to be 1.25×10^{-3} (see Chapter 4) to match the fluctuation level of the Periodic simulation with experiment. Had I tuned this parameter with the Dirichlet or Neumann simulations in mind, it would seem that the Periodic and Sheath simulations had fluctuation levels too large. So, in fact, all four of these simulations are qualitatively consistent with the experiment, and they are also quantitatively consistent with the caveat that the quantitative match is caused by tuning a single free parameter. I don't provide any error analysis to quantify the agreement between simulation and experiment, but rather just use an eye test. The fact that several different statistical properties of several fields (see Fig. 5.7) agree between simulation and experiment lends evidence to my claim that the simulation model is relatively well validated.

One final statistical measurement that may be compared between simulation and experiment is the spatial correlation. Experimentally, this can be done by

fixing one probe at a certain location and moving another probe around and measuring the correlation between the two I_{sat} signals. The second probe can scan the $r - \theta$ plane at an axial location close to the first probe. The results of the simulated spatial correlation compared to the experimental correlation are shown in Fig. 5.9. For the simulation, I show only the result from the Periodic simulation. The darkest red point, which has a correlation value of 1 marks the location of the stationary probe. The black line is the $1/e$ contour, where the distance from the stationary probe to this contour is the correlation length. The simulation correlation length of about 1 cm is about half of that of the experimental correlation length. Furthermore, neither have completely isotropic structure, and their slight divergences from isotropy are not that similar. However, there is no complex mode structure or long extended correlations in either one.

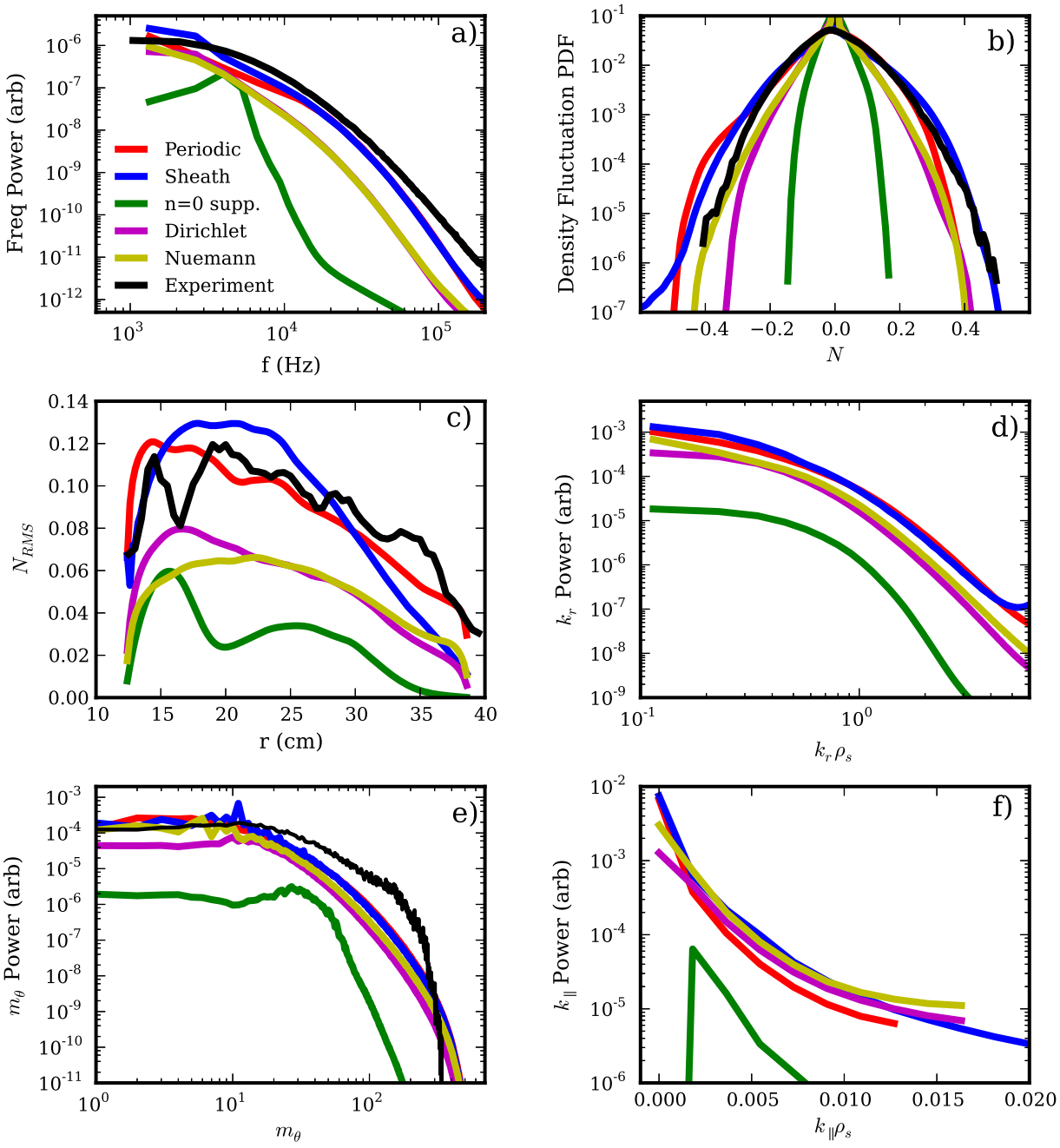

Figure 5.8: Density statistics

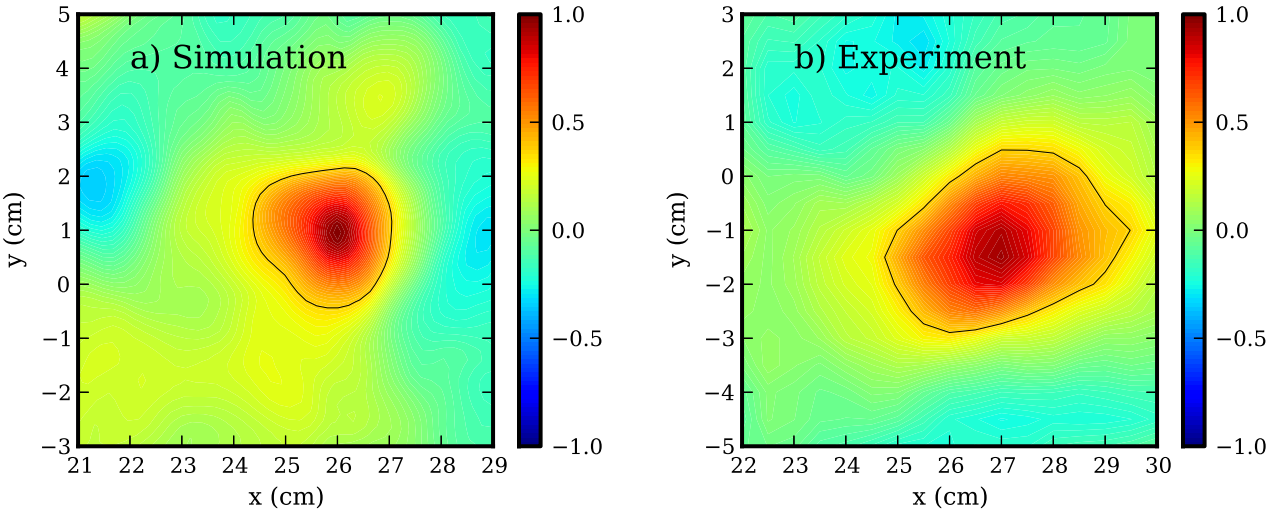

Figure 5.9: Spatial density correlations

CHAPTER 6

Energy Dynamics Formalism

In the last section of the previous chapter, I analyzed the experimental and simulated turbulence using simple and common statistical methods. Never did I assume any kind of model for the turbulence, nor did I take full advantage of the wealth of spatial information provided by the simulations. In the remaining chapters, I do use the simulated physics model along with the turbulent spatial structures to analyze the nature of the turbulence from an energy dynamics perspective. The energy dynamics provide direct information about energy injection into the turbulence from the equilibrium gradients, energy transfer among different fields and between different normal modes, and turbulent energy dissipation. This information allowed me to uncover the mysterious mechanism that drives the $n = 0$ fluctuations so strongly in the simulations (see Fig. 5.8 f)). The mechanism is a nonlinear instability. I will provide evidence for this in the next chapter, but in this chapter, I will derive the dynamical energy equations and explain what they mean.

6.1 Total Energy and Dynamics

First, I consider the total, volume-averaged energy and energy dynamics. The total volume-averaged energy of the fluctuations (in normalized units) is:

$$E = \frac{1}{2}\int_V \left[P_0 \left((N/N_0)^2 + \frac{3}{2}(T_e/T_{e0})^2 \right) + N_0 \left(\frac{m_e}{m_i} v_{\|e}^2 + (\nabla_\perp \phi)^2 \right) \right] dV, \quad (6.1)$$

where $P_0 = N_0 T_{e0}$ is the equilibrium pressure. The $\frac{1}{2}P_0(N/N_0)^2$ term is the potential energy due to density fluctuations, $\frac{3}{4}P_0(T_e/T_{e0})^2$ is the electron temperature fluctuation potential energy, $\frac{1}{2}N_0\frac{m_e}{m_i}v_{\|e}^2$ is the parallel electron kinetic energy, and $\frac{1}{2}N_0(\nabla_\perp\phi)^2$ is the $\mathbf{E}\times\mathbf{B}$ perpendicular kinetic energy. The energy contained in the electric field is smaller than the perpendicular kinetic energy by a factor of $(v_A/c)^2$ and is therefore neglected.

The dynamical energy evolution $\partial E/\partial t$ can be obtained using Eqs. 4.1- 4.4 in the following way. First, take Eq. 4.1 and multiply both sides by $\frac{T_{e0}}{N_0}N$ and integrate over the volume. The result is:

$$\frac{\partial E_N}{\partial t} = \left\langle -T_{e0}N\mathbf{v_E}\cdot\nabla \ln N_0 - T_{e0}N\nabla_\| v_{\|e} - \mu_N\frac{T_{e0}}{N_0}(\nabla_\perp N)^2 + \frac{T_{e0}}{N_0}NS_N\right\rangle, \quad (6.2)$$

where $E_N = \frac{1}{2}\left\langle P_0(N/N_0)^2\right\rangle$ with $\langle\rangle$ shorthand for the volume integral $\int_V dV$. Next, multiply Eq. 4.2 by $N_0\frac{m_e}{m_i}v_{\|e}$, Eq. 4.3 by $-\phi$, and Eq. 4.4 by $\frac{3}{2}\frac{N_0}{T_{e0}}T_e$ and volume integrate, giving:

$$\begin{aligned}
\frac{\partial E_v}{\partial t} &= \left\langle -T_{e0}v_{\|e}\nabla_\| N - 1.71N_0 v_{\|e}\nabla_\| T_e + N_0 v_{\|e}\nabla_\|\phi - \frac{m_e}{m_i}N_0\nu_e v_{\|e}^2\right\rangle, & (6.3)\\
\frac{\partial E_\phi}{\partial t} &= \left\langle N_0\phi\nabla_\| v_{\|e} - \nu_{in}N_0(\nabla_\perp\phi)^2 - \mu_\phi\phi\nabla_\perp^2\varpi\right\rangle, & (6.4)\\
\frac{\partial E_T}{\partial t} &= \left\langle -\frac{3}{2}N_0T_e\mathbf{v_E}\cdot\nabla\ln T_{e0} - 1.71N_0T_e\nabla_\| v_{\|e} - \kappa_{\|e}/T_{e0}(\nabla_\| T_e)^2\right\rangle \\
&+ \left\langle -\frac{3m_e}{m_i}\frac{N_0}{T_{e0}}\nu_e T_e^2 - \frac{3}{2}\mu_T\frac{N_0}{T_{e0}}(\nabla_\perp T_e)^2 + \frac{3}{2}\frac{N_0}{T_{e0}}T_eS_T\right\rangle, & (6.5)
\end{aligned}$$

where $E_v = \frac{1}{2}\left\langle N_0\frac{m_e}{m_i}v_{\|e}^2\right\rangle$, $E_\phi = \frac{1}{2}\left\langle N_0(\nabla_\perp\phi)^2\right\rangle$, and $E_T = \frac{3}{4}\left\langle P_0(T_e/T_{e0})^2\right\rangle$.

Note that there are a few simplifications made in these equations. One simplification is that the term $\left\langle \mu_N\frac{T_{e0}}{N_0}N\nabla_\perp^2 N\right\rangle$ is written approximately as $-\left\langle \mu_N\frac{T_{e0}}{N_0}(\nabla_\perp N)^2\right\rangle$ in Eq. 6.2. The fact that $\frac{T_{e0}}{N_0}\approx 1$ makes this approximation acceptable. In fact, I don't use this approximation when calculating such quantities from the simulations, but I write it here as it illuminates the fact that this energy term

is negative. I use the same approximation with the $-\left\langle \frac{3}{2}\mu_T \frac{N_0}{T_{e0}}(\nabla_\perp T)^2 \right\rangle$ and $-\left\langle \kappa_{\|e}/T_{e0}(\nabla_\| T_e)^2 \right\rangle$ terms, although the latter contains the fraction $\kappa_{\|e}/T_{e0}$, which is not necessarily close to being constant.

Moreover, notice that none of the advective nonlinear terms are present in these energy dynamics equations. The reason is that $\langle f\{g,f\}\rangle = 0$, which holds as long as all of the boundaries are periodic, have $f = 0$ boundaries, or have $\nabla g \cdot d\vec{S} = 0$ boundaries. Now only Eq. 6.4 actually has this $\langle f\{g,f\}\rangle$ form for its nonlinearity because all of the other energy equations contain equilibrium profile quantities in the volume average (e.g. $\left\langle \frac{T_{e0}}{N_0} N\{\phi, N\} \right\rangle$ in Eq. 6.2). Nevertheless, the equilibrium profile quantities come as $\frac{T_{e0}}{N_0} \approx 1$ for Eq. 6.2 and $\frac{N_0}{T_{e0}} \approx 1$ for Eq. 6.5, while there is a factor of the electron to ion mass ratio multiplied by the nonlinearity in Eq. 6.3. This means that all of the nonlinearities approximately vanish in the energy equations. Furthermore, I have confirmed this by direct calculation of these terms. This is why I do not include the nonlinearities in Eqs. 6.2- 6.5.

I note that I could have used a different expression for the energy in order to absolutely conserve the nonlinearities. For instance, I could have set $E_N = \frac{1}{2}\langle N^2 \rangle$, neglecting the factor $\frac{T_{e0}}{N_0}$. In fact, I did this in the Friedman et al. paper [FCU12]. However, this expression would not be the physical energy, although it would have the convenient property of conserving the nonlinearities. Energy, after all, is a useful concept because it's a conserved quantity. Nevertheless, I have chosen to use the physical energy in this work as well as in another paper [FCU13] because the physical energy conserves the adiabatic response. I will show this below. Furthermore, the physical energy very nearly conserves the nonlinearities, so it's not a big problem to use the physical energy. The calculated error of neglecting the nonlinearities in the energy dynamics equations is only about 1%. Now, one may wonder why the physical energy doesn't absolutely conserve the advective nonlinearities. The answer lies in the partial linearization of the simulation equa-

tions. The linearization neglects many nonlinear contributions that are needed for global energy conservation. Nevertheless, I find that the spectral energy dynamics analysis in Sec. 6.2 is simpler when I neglect most of the nonlinearities.

Now Eqs. 6.2- 6.5 are still not increadibly revealing because they contain nearly as many terms as the original simulated equations. However, I can break each of these equations down in the following way:

$$\frac{\partial E_j}{\partial t} = Q_j + C_j + D_j. \tag{6.6}$$

The subscript j represents the individual field: (N, v, ϕ, T). Q_j represents energy injection from an equilibrium gradient. For example, Q_N represents the energy injected into E_N (the density fluctuation potential energy) taken from the free energy of the equilibrium density gradient ($\nabla_r N_0$). These terms are:

$$\begin{aligned} Q_N &= \left\langle -T_{e0} N \mathbf{v_E} \cdot \nabla \ln N_0 \right\rangle, & (6.7)\\ Q_v &= 0, & (6.8)\\ Q_\phi &= 0, & (6.9)\\ Q_T &= \left\langle -\frac{3}{2} N_0 T_e \mathbf{v_E} \cdot \nabla \ln T_{e0} \right\rangle. & (6.10) \end{aligned}$$

Only the density and temperature fluctuations receive energy from the equilibrium density and temperature gradients, respectively. They do so by radial $\mathbf{E} \times \mathbf{B}$ advection, moving fluid or heat across the gradient where it can enhance or diminish the density and temperature fluctuations. I call the Q_j terms energy injection terms, but they can in fact dissipate fluctuation energy if the phase between the density (or temperature) and potential are stabilizing.

Next, the C_j terms represent transfer channels. They are:

$$C_N = \left\langle -T_{e0} N \nabla_\parallel v_{\parallel e} \right\rangle, \tag{6.11}$$

$$C_v = \left\langle -T_{e0} v_{\parallel e} \nabla_\parallel N - 1.71 N_0 v_{\parallel e} \nabla_\parallel T_e + N_0 v_{\parallel e} \nabla_\parallel \phi \right\rangle , \tag{6.12}$$

$$C_\phi = \left\langle N_0 \phi \nabla_\parallel v_{\parallel e} \right\rangle , \tag{6.13}$$

$$C_T = \left\langle -1.71 N_0 T_e \nabla_\parallel v_{\parallel e} \right\rangle . \tag{6.14}$$

Notice that $C_N + C_\phi + C_T = -C_v$ if the axial boundaries are periodic or zero value. Alternatively, $\sum_j C_j = 0$. So no energy is gained or lost in total. Energy does, however, transfer between the different fields: $N, T_e, \phi \leftrightarrow v_{\parallel e}$. All energy transfers through the parallel electron velocity. The density, temperature, and potential fluctuations all feed or draw energy from the parallel electron velocity. The equations allow no state variable energy transfer. For instance, the density and potential fluctuations cannot transfer energy between each other directly. Recall that this is the mechanism of the adiabatic response (see Sec. 5.1). I commented on the conservation of energy of the adiabatic response above when discussing the use of the physical energy, and this is what I meant. Note that the "energy-like" expression used in one of our papers [FCU12] that absolutely conserved the advective nonlinearities did not come close to conserving the adiabatic response energy. That's why in this work and in another paper [FCU13], I chose to use the physical energy.

I inject two minor points concerning the boundary conditions. The first is that the Neumann and sheath simulations don't exactly conserve the adiabatic response because of non-vanishing contributions from the boundaries. Second, the sheath boundary conditions allow energy transfer between the temperature and potential fluctuations without the adiabatic response. That transfer mechanism isn't represented in the C_j expressions. I will calculate it in Chapter 8.

Finally, the D_j terms represent dissipative energy loss from the fluctuations. They are:

$$D_N = \left\langle -\mu_N \frac{T_{e0}}{N_0} (\nabla_\perp N)^2 + \frac{T_{e0}}{N_0} N S_N \right\rangle , \tag{6.15}$$

$$
\begin{aligned}
D_v &= \left\langle -\frac{m_e}{m_i} N_0 \nu_e v_{\parallel e}^2 \right\rangle, && (6.16)\\
D_\phi &= \left\langle -\nu_{in} N_0 (\nabla_\perp \phi)^2 - \mu_\phi \phi \nabla_\perp^2 \varpi \right\rangle, && (6.17)\\
D_T &= \left\langle -\kappa_{\parallel e}/T_{e0} (\nabla_\parallel T_e)^2 - \frac{3m_e}{m_i} \frac{N_0}{T_{e0}} \nu_e T_e^2 \right\rangle \\
&+ \left\langle -\frac{3}{2} \mu_T \frac{N_0}{T_{e0}} (\nabla_\perp T_e)^2 + \frac{3}{2} \frac{N_0}{T_{e0}} T_e S_T \right\rangle. && (6.18)
\end{aligned}
$$

Most of these terms are clearly negative. However, the source terms do not have a clear sign and the $\langle -\mu_\phi \phi \nabla_\perp^2 \varpi \rangle$ viscous term in Eq. 6.17 doesn't have a clear sign either. Recall, though, that the sources essentially remove the flux-surface averaged component of the density and temperature fluctuations, indicating that they remove the energy associated with these fluctuation components. Taking $S_N \approx -\langle N \rangle_{fs}$ from Eqs. 4.5 and 4.6, then the source contribution to D_N is $-\left\langle \frac{T_{e0}}{N_0} \langle N \rangle_{fs}^2 \right\rangle$, which is negative. The viscous term in Eq. 6.17 is less obviously negative, however, letting $\nabla_\perp \to -k_\perp^2$ makes the viscous term approximately $-\langle \mu_\phi N_0 k_\perp^4 \phi^2 \rangle$. So it's reasonable to conclude that all contributions in the D_j expressions are absolutely negative. My direct calculations have confirmed this.

6.2 Spectral Energy Dynamics

While the total energy dynamics can reveal some important information such as the amount of energy entering the density fluctuations vs. the temperature fluctuations, the direction of energy flow through the adiabatic response, and how much energy is dissipated by the various mechanisms, the total dynamics cannot show the mechanism of the nonlinear instability. In fact, the total energy dynamics are rather useless in revealing any nonlinear physics. Spectral or mode-decomposed energy dynamics, on the other hand, provide much more information regarding mode-specific processes like cascades and complex nonlinear processes.

When deriving mode-decomposed energy dynamics, one first has to choose a set of basis functions. As long as the functions form an independent complete

basis, they are acceptable. Fourier modes are a natural basis to use for any coordinate with periodic boundaries. Fourier modes are also orthogonal to one another, making them ideal. Linear eigenmodes provide another good choice for a basis; however, they can be non-orthogonal in some systems, making them somewhat unweildy. I began this study using a linear eigenmode decomposition, but I eventually gave up that path because the linear eigenmodes of this system are non-orthogonal. The results were complicated and didn't show anything more interesting than a simpler Fourier decomposition would show. Hatch et al. dealt with this non-orthogonality problem with two distinct methods [HTJ11]. The first was to use a Gram-Schmidt orthogonalization procedure starting with the most unstable linear eigenmode to make the modes orthogonal. The resulting modes other than the most unstable linear eigenmode, however, were no longer the linear eigenmodes. The second method was to use a proper orthogonal decomposition (POD, which is essentially a kind of singular value decomposition) to create orthogonal modes that best captured the dominant turbulent structures. Both of these methods are very interesting and quite useful for some systems, however, they are probably most useful for systems with strong linear instabilities where most of the energy of the turbulence is contained in the fastest growing linear eigenmode or a dominant POD mode. That is not the case for the LAPD turbulence.

I found that the most useful basis to take is a partial Fourier basis. Namely, I simply use a Fourier decomposition in the azimuthal and axial directions. For example, I decompose the density in the following way:

$$N(r,\theta,z,t) = \sum_{\vec{k}} n_{\vec{k}}(r,t) e^{i(m\theta + k_z z)}. \tag{6.19}$$

Here, $k_z = \frac{2\pi n}{L_\parallel \rho_s}$, where n is the axial mode number and m is the azimuthal mode number, and the $\vec{k}$ symbol is short for (m,n). The sum over $\vec{k}$ is in fact

a double sum over m and n. Furthermore, positive and negative m and n are included in the sums to ensure reality of N since $n_{-\vec{k}} = n^*_{\vec{k}}$. Similar decompositions are used for $v_{\|e}, \phi$, and T_e. Note that the radial part of the basis function $n_{\vec{k}}(r,t)$ is time-dependent and shouldn't really be called a basis function at all because of this. I cannot say anything about nonlinear processes involving different radial modes since I haven't decomposed the radial structures into a time-independent basis. Essentially, I have limited the amount of information I can gain from this decomposition. I have intentionally done this to focus on a few particular results, which would be more difficult to see if I used an additional radial decomposition.

To derive the spectral energy equations, I first substitute the Fourier decompositions into Eqs. 4.1- 4.4. Using the density evolution equation as an example, I get:

$$\begin{aligned}
&\sum_{\vec{k}} \frac{\partial n_{\vec{k}}}{\partial t} e^{i(m\theta + k_z z)} = \\
&\sum_{\vec{k}} \left[-\frac{im}{r} \partial_r N_0 \phi_{\vec{k}} - i k_z N_0 v_{\vec{k}} + \mu_N (\partial_r^2 n_{\vec{k}} + \frac{1}{r} \partial_r n_{\vec{k}} - \frac{m^2}{r^2} n_{\vec{k}}) \right] e^{i(m\theta + k_z z)} \\
&+ \frac{1}{r} \sum_{\vec{k},\vec{k}'} (imn_{\vec{k}} \partial_r \phi_{\vec{k}'} - im' \partial_r n_{\vec{k}} \phi_{\vec{k}'}) e^{i(m+m')\theta + i(k_z + k'_z)z} + S_N. \qquad (6.20)
\end{aligned}$$

Note the double sum for the nonlinearity. Continuing on with just the density equation for now, I proceed to get the energy equation by multiplying through by $\frac{T_{e0}}{N_0} n^*_{\vec{k}''} e^{-im''\theta - ik''_z z}$ and integrating over space. The result is (with primes permutted):

$$\begin{aligned}
&\frac{1}{2} \left\langle \frac{T_{e0}}{N_0} \frac{\partial |n_{\vec{k}}|^2}{\partial t} \right\rangle = \\
&\left\langle -\frac{T_{e0}}{N_0} \frac{im}{r} \partial_r N_0 \phi_{\vec{k}} n^*_{\vec{k}} - i k_z T_{e0} v_{\vec{k}} n^*_{\vec{k}} + \frac{T_{e0}}{N_0} \mu_N (\partial_r^2 n_{\vec{k}} + \frac{1}{r} \partial_r n_{\vec{k}} - \frac{m^2}{r^2} n_{\vec{k}}) n^*_{\vec{k}} \right\rangle
\end{aligned}$$

$$+\left\langle \frac{T_{e0}}{rN_0}\sum_{\vec{k}'}\left(im'n_{\vec{k}'}\partial_r\phi_{\vec{k}-\vec{k}'}n^*_{\vec{k}}-i(m-m')\partial_r n_{\vec{k}'}\phi_{\vec{k}-\vec{k}'}n^*_{\vec{k}}\right)\right\rangle$$
$$+\left\langle \frac{T_{e0}}{N_0}S_N n^*_{\vec{k}=0}\right\rangle, \tag{6.21}$$

where the brackets now represent the reality operator and the radial integral $Re\left\{\int rdr\right\}$ because I have performed the azimuthal and axial integrations and taken the real part of the equation. Breaking this up into specific parts:

$$\frac{\partial E_N(\vec{k})}{\partial t} = Q_N(\vec{k}) + C_N(\vec{k}) + D_N(\vec{k}) + \sum_{\vec{k}'} T_N(\vec{k},\vec{k}') \tag{6.22}$$

with

$$E_N(\vec{k}) = \frac{1}{2}\left\langle \frac{T_{e0}}{N_0}|n_{\vec{k}}|^2\right\rangle \tag{6.23}$$
$$Q_N(\vec{k}) = \left\langle -\frac{im}{r}\frac{T_{e0}}{N_0}\partial_r N_0\phi_{\vec{k}}n^*_{\vec{k}}\right\rangle \tag{6.24}$$
$$C_N(\vec{k}) = \left\langle -ik_z T_{e0}v_{\vec{k}}n^*_{\vec{k}}\right\rangle \tag{6.25}$$
$$D_N(\vec{k}) = \left\langle \frac{T_{e0}}{N_0}\mu_N(\partial_r^2 n_{\vec{k}}+\frac{1}{r}\partial_r n_{\vec{k}}-\frac{m^2}{r^2}n_{\vec{k}})n^*_{\vec{k}}+\frac{T_{e0}}{N_0}S_N n^*_{\vec{k}=0}\right\rangle \tag{6.26}$$
$$T_N(\vec{k},\vec{k}') = \left\langle \frac{T_{e0}}{rN_0}\left(im'n_{\vec{k}'}\partial_r\phi_{\vec{k}-\vec{k}'}n^*_{\vec{k}}-i(m-m')\partial_r n_{\vec{k}'}\phi_{\vec{k}-\vec{k}'}n^*_{\vec{k}}\right)\right\rangle \tag{6.27}$$

The new piece not in the total energy dynamics in Sec. 6.1, $T_N(\vec{k},\vec{k}')$, comes from the advective nonlinearity. It couples different Fourier modes, meaning that it transfers energy between different $\vec{k}$ waves. It is not conserved for individual $\vec{k}$ modes, but is conserved on the aggregate, meaning $\sum_{\vec{k},\vec{k}'} T_N(\vec{k},\vec{k}') \simeq 0$. Notice also that $Q_N(\vec{k})$ can be finite for $n = 0$, but $C_N(\vec{k})$ is zero for $n = 0$. In other words, flute modes may take energy from the equilibrium density gradient, but they cannot access the adiabatic response. This precludes linear drift wave flute modes. But it does not preclude nonlinear drift wave flute modes because they can transfer their energy to non-flute structures in order to access the adiabatic response.

For completeness, I write the rest of the spectral energy dynamics pieces here. The perpendicular kinetic energy dynamics pieces are:

$$
\begin{aligned}
E_\phi(\vec{k}) &= \frac{1}{2}\left\langle N_0 \left|\frac{\partial \phi_{\vec{k}}}{\partial r}\right|^2 + N_0 \frac{m^2}{r^2}|\phi_{\vec{k}}|^2 \right\rangle && (6.28)\\
Q_\phi(\vec{k}) &= 0 && (6.29)\\
C_\phi(\vec{k}) &= \left\langle i k_z N_0 v_{\vec{k}} \phi^*_{\vec{k}} \right\rangle && (6.30)\\
D_\phi(\vec{k}) &= \left\langle -\mu_\phi(\partial_r^2 \varpi_{\vec{k}} + \frac{1}{r}\partial_r \varpi_{\vec{k}} - \frac{m^2}{r^2}\varpi_{\vec{k}})\phi^*_{\vec{k}} - \nu_{in} E_\phi(\vec{k}) \right\rangle && (6.31)\\
T_\phi(\vec{k},\vec{k}') &= \left\langle -\frac{1}{r}\left(i m' \varpi_{\vec{k}'} \partial_r \phi_{\vec{k}-\vec{k}'} \phi^*_{\vec{k}} - i(m-m')\partial_r \varpi_{\vec{k}'} \phi_{\vec{k}-\vec{k}'} \phi^*_{\vec{k}} \right) \right\rangle && (6.32)
\end{aligned}
$$

and for the electron temperature potential energy:

$$
\begin{aligned}
E_T(\vec{k}) &= \frac{3}{4}\left\langle \frac{N_0}{T_{e0}} |t_{\vec{k}}|^2 \right\rangle && (6.33)\\
Q_T(\vec{k}) &= \left\langle -\frac{3}{2}\frac{N_0}{T_{e0}}\frac{im}{r}\partial_r T_{e0} \phi_{\vec{k}} t^*_{\vec{k}} \right\rangle && (6.34)\\
C_T(\vec{k}) &= \left\langle -1.71 i k_z N_0 v_{\vec{k}} t^*_{\vec{k}} \right\rangle && (6.35)\\
D_T(\vec{k}) &= \left\langle -\frac{\kappa_{\|e}}{T_{e0}} k_z^2 |t_{\vec{k}}|^2 - \frac{3 m_e}{m_i}\frac{N_0}{T_{e0}}\nu_e |t_{\vec{k}}|^2 \right\rangle \\
&+ \left\langle \frac{3}{2}\frac{N_0}{T_{e0}}\mu_T(\partial_r^2 t_{\vec{k}} + \frac{1}{r}\partial_r t_{\vec{k}} - \frac{m^2}{r^2} t_{\vec{k}}) t^*_{\vec{k}} + \frac{3}{2}\frac{N_0}{T_{e0}} S_T t^*_{\vec{k}=0} \right\rangle && (6.36)\\
T_T(\vec{k},\vec{k}') &= \left\langle \frac{3}{2r}\frac{N_0}{T_{e0}}\left(i m' t_{\vec{k}'} \partial_r \phi_{\vec{k}-\vec{k}'} t^*_{\vec{k}} - i(m-m')\partial_r t_{\vec{k}'} \phi_{\vec{k}-\vec{k}'} t^*_{\vec{k}} \right) \right\rangle && (6.37)
\end{aligned}
$$

and for the parallel kinetic energy:

$$
\begin{aligned}
E_v(\vec{k}) &= \frac{1}{2}\frac{m_e}{m_i}\left\langle N_0 |v_{\vec{k}}|^2 \right\rangle && (6.38)\\
Q_v(\vec{k}) &= 0 && (6.39)\\
C_v(\vec{k}) &= \left\langle -i k_z N_0 n_{\vec{k}} v^*_{\vec{k}} + i k_z N_0 \phi_{\vec{k}} v^*_{\vec{k}} - 1.71 i k_z T_{e0} t_{\vec{k}} v^*_{\vec{k}} \right\rangle && (6.40)\\
D_v(\vec{k}) &= \left\langle -\nu_e \frac{m_e}{m_i} N_0 |v_{\vec{k}}|^2 \right\rangle && (6.41)\\
T_v(\vec{k},\vec{k}') &= \left\langle \frac{m_e}{m_i}\frac{N_0}{r}\left(i m' v_{\vec{k}'} \partial_r \phi_{\vec{k}-\vec{k}'} v^*_{\vec{k}} - i(m-m')\partial_r v_{\vec{k}'} \phi_{\vec{k}-\vec{k}'} v^*_{\vec{k}} \right) \right\rangle . && (6.42)
\end{aligned}
$$

CHAPTER 7

Nonlinear Instability for the Periodic Simulation

In this chapter, I use the energy dynamics machinery developed in the last chapter to show where in wavenumber space and to which fields energy is deposited, how it's transferred, and where it's dissipated. I show that the linear instability plasma paradigm doesn't hold for the LAPD simulations, but rather, a complex nonlinear instability process dominates the energy dynamics. Furthermore, in this chapter, I consider only the simulations with periodic boundary conditions: the Periodic simulation and the $n = 0$ suppressed simulation. I analyze the remaining simulations (Dirichlet, Neumann, and Sheath) in the next chapter.

7.1 Energy Dynamics Applied to LAPD Turbulence

7.1.1 The Energy Spectra

Although I have already discussed the relative importance of the $n = 0$ fluctuation flute structures and shown evidence for this in Figs. 5.3, 5.4, and 5.8, I now use the energy expressions in Eqs. 6.23, 6.28, 6.33, and 6.38 to show a detailed look at the energy wavenumber spectra. The spectra for the four fields in (m, n) space are shown in Fig. 7.1. As expected from Figs. 5.3, 5.4, and 5.8, most of the density energy $E_N(\vec{k})$ is located at $n = 0$ (and $1 < m < 10$). This wavenumber location is much different from my expectation which was that of the fastest growing linear eigenmode, which is at $(n = 1, m = 60)$. Additionally, $E_T(\vec{k})$ and $E_\phi(\vec{k})$ have similar-looking spectra as $E_N(\vec{k})$, though the actual magnitudes of the energy

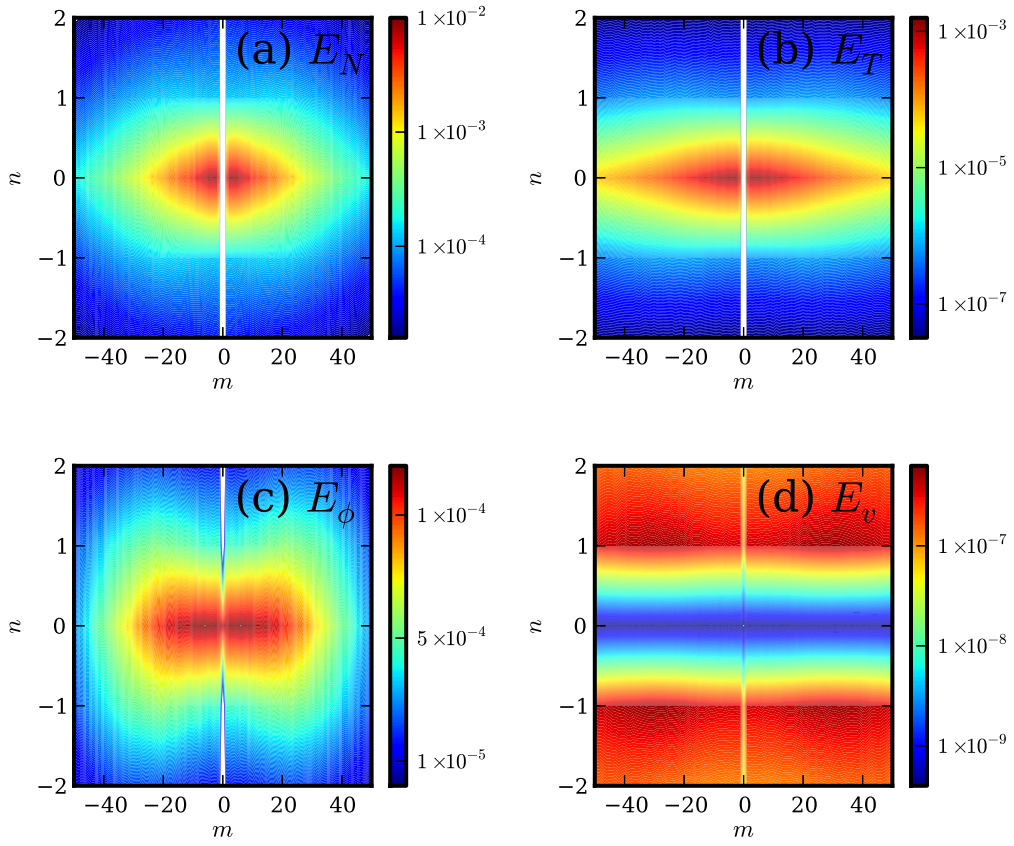

Figure 7.1: Energy k-Spectra

are quite different for the three fields. Finally, $E_v(\vec{k})$ has a remarkably different energy spectrum than the other fields. Most of the energy is contained at $n \geq 1$ and $m \sim 30$, which is somewhat similar to the linear eigenmode growth rate spectrum, though m is lower.

Although these results are rather unexpected given the hypothesis that the most unstable linear eigenmode should pump energy into the turbulent system, one could still build upon this hypothesis to explain the nature of the spectra. In fact, in Ref. [UPC11], my collaborators and I posited and tested this hypothesis. Our specific hypothesis was that the most unstable linear eigenmode pumped

energy into the system at its characteristic wavenumber and then proceeded to cascade energy forward and backward into other waves. The inverse cascade into $n = 0$ would be particularly strong to account for all of the energy in the $n = 0$ Fourier components.

Our test of this inverse cascade revolved around the use of a particular bicoherence three wave interaction, namely that between three density fluctuation Fourier modes of $(n, m) = (1, 25), (-1, -24)$ and $(0, 1)$. Note that in that study, we used a different set of profiles and parameters for the simulation than the one I use in this report, and the dominant azimuthal mode numbers in that study were smaller than those in this report. In any case, in Ref. [UPC11], we found a strong bicoherence amplitude for this three-wave interaction and assumed that this meant that the waves with $(n, m) = (1, 25)$ and $(-1, -24)$ coupled to transfer their energy to waves with $(0, 1)$. This fit within the standard linear instability paradigm because linear eigenmodes with $(n, m) \sim (\pm 1, \pm 25)$ were the most unstable for that system. Unfortunately, bicoherence is only a vague proxy for three-wave energy interaction, and it doesn't indicate a direction of energy transfer. As I later worked on energy dynamics calculations, I discovered, to my surprise, that we had the direction of energy transfer backwards! Our assumption regarding the direction of energy transfer was wrong. The paradigmatic plasma turbulence view led us astray.

7.1.2 Energy Dynamics Details

The full energy dynamics analysis using the machinery of Chapter 6 removes any ambiguity regarding the locations and magnitudes of energy injection into the fluctuations and direction of energy transfer between different Fourier modes. In fact, the full dynamics contains so much information that it can be difficult to digest it all. I therefore try to focus on the most important parts, especially those that are crucial to the nonlinear instability. First, in Fig. 7.2, I show values for

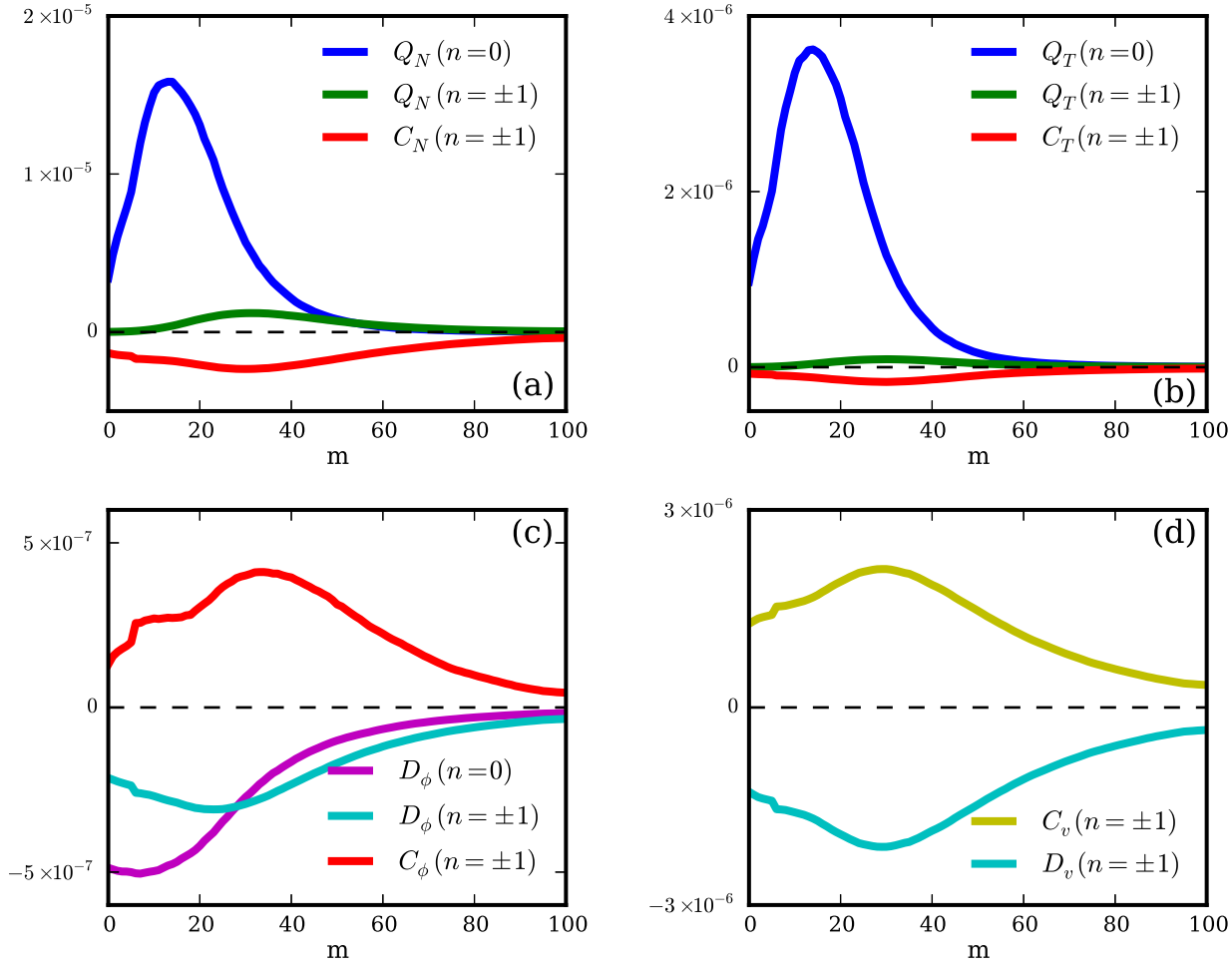

Figure 7.2: Periodic simulation energy dynamics

some of the Q_j, C_j, and D_j terms in the energy dynamics equations for $n = 0, \pm1$ and $0 \leq m \leq 100$, neglecting all dynamics with $|n| \geq 2$, which have relatively small values and are mostly insignificant. The dynamics curves are all averaged over a time period during the turbulent stage of the simulation where the dynamics processes have all reached a quasi-steady state. The label $n = \pm1$ represents the addition of terms with $n = 1$ and $n = -1$. Fig. 7.2 a) reveals the density potential energy injection (Q_N) and the adiabatic response transfer (C_N). I don't show

the dissipation (D_N) in this figure, which is why the curves don't seem to add up to zero as they would if all dynamics were shown. Nevertheless, this figure immediately reveals that the majority of the energy is injected straight into the $n = 0$ fluctuations from the equilibrium density gradient rather than into the $n = \pm 1$ fluctuations! Looking at Eq. 6.24 again, and I reiterate, $Q_N(\vec{k})$ does not depend on n, so it is perfectly acceptable to inject energy straight into $n = 0$ fluctuations. However, $C_N(\vec{k})$ is proportional to n (Eq. 6.25), so energy can only travel through the adiabatic response path in finite n structures. This is why the unstable linear eigenmodes have finite n – because eigenmodes with $n = 0$ cannot access the adiabatic response and thus have no field coupling. But with nonlinearities involved, there is nothing to prevent energy extraction at $n = 0$. Likewise, Fig. 7.2 b) reveals the same kind of story for the temperature potential energy, although the magnitudes are quite low compared to the density ones, indicating that the temperature fluctuations are relatively insignificant as a player in the total energy dynamics.

Fig. 7.2 c) shows the perpendicular kinetic energy dynamics. Recall $Q_\phi = 0$, so there is no direct energy injection; rather, energy enters ϕ fluctuations via the adiabatic response (C_ϕ). Even though no energy enters ϕ at $n = 0$, flute-like dissipation $D_\phi(n = 0)$ is significant, forshadowing the need for three-wave energy transfer into $n = 0$ ϕ fluctuations. Additionally, although I don't show $|n| \geq 2$ dynamics, they are somewhat important for C_ϕ and D_ϕ, accounting for the obviously unbalanced dynamics in this figure. Lastly, Fig. 7.2 d) reveals the parallel kinetic energy dynamics, which simply includes the adiabatic transfer (C_v) and electron-ion frictional dissipation (D_v). Recall that $C_N + C_\phi + C_T = -C_v$ for each $\vec{k}$. In other words, looking at the C_j terms altogether, one can see that energy is drawn from the density and potential fluctuations into the $v_{\|e}$ fluctuations and then moves onto the electrostatic potential ϕ fluctuations. That is only clear when looking at all of the C_j taken together.

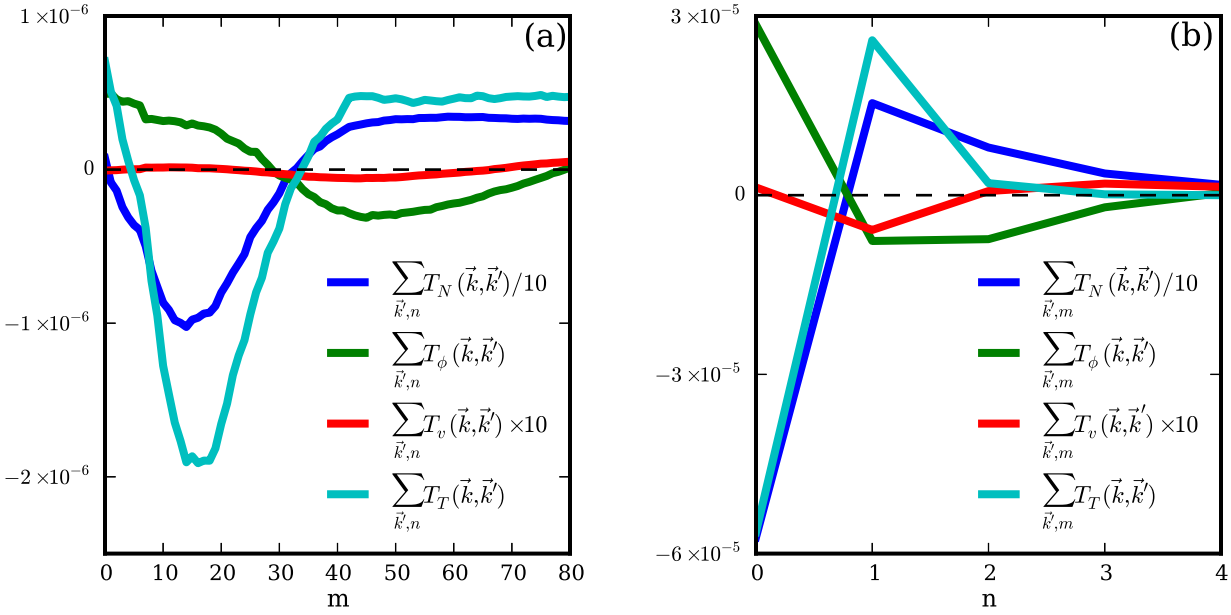

Figure 7.3: Periodic simulation three-wave transfer dynamics

Fig. 7.2 only shows the dynamical pieces due to the linear terms of Eqs. 4.1-4.4, and they therefore don't show the nonlinear transfer between different $\vec{k}$. The advective nonlinearities provide this transfer (the $T_j(\vec{k},\vec{k'})$ terms), and they are essentially conservative, meaning they provide no net injection or dissipation with respect to the fluctuations. Now the $T_j(\vec{k},\vec{k'})$ terms are each four dimensional, making them difficult to show. I choose to sum over some of the dimensions to show some of their aggregate properties. In Fig. 7.3 a), I sum over $\vec{k'}$ and n leaving them as only functions of m. Also note that I have divided $T_N(\vec{k},\vec{k'})$ by 10 and multiplied $T_v(\vec{k},\vec{k'})$ by 10 so that all of the T_j can be shown on one plot. Notice where T_N and T_T are positive and where they are negative. Negative values at a particular m indicate that the fluctuations with azimuthal wavenumber m are giving up net energy, while positive values correspond to fluctuations that are taking up net energy at that m. T_N and T_T transfer, on the aggregate, energy in the range $5 < m < 30$ to energy at all other values of m. This is not at all surprising because Q_N and Q_T are largest for $5 < m < 30$. This means that energy is

injected from the equilibrium gradients at $5 < m < 30$ and then three-wave transferred into other azimuthal wave numbers in both forward and inverse cascades (mostly forward). Actually the summation I use hides the information regarding the locality of wavenumber transfer, so it's indeterminate from this figure whether the transfer process is by cascading or non-local transfer. I defer this detail to future work. On the other hand, T_ϕ and T_v have the opposite character of T_N and T_T, meaning that the transfer dynamics are the other way around. This is typical in similar systems, such as Hasegawa-Wakatani systems [HW83, CBS95] in which the density potential energy exhibits a forward cascade, while the perpendicular kinetic energy exhibits an inverse cascade. It was also obvious that this had to happen given the azimuthal assymetry between C_ϕ and D_ϕ (see Fig. 7.2 c)).

More importantly, however, Fig. 7.3 b) shows the axial wavenumber transfers. Again T_N and T_T are similar. Both show energy transfer from $n = 0$ to $n \neq 0$. This is truly important! It is the most direct evidence for the nonlinear instability. Our paradigmatic hypothesis in Ref. [UPC11] posited the opposite transfer direction. The most unstable linear eigenmodes have $n = \pm 1$ and all eigenmodes with $n = 0$ are stable, yet Fig. 7.3 b) shows that the dominant energy transfer is from $n = 0$ to $n \neq 0$, at least for N and T_e. Again, T_ϕ and T_v have the opposite character of T_N and T_T, as really they must, since ϕ and $v_{\|e}$ gain their energy through the adiabatic response.

It's still difficult to see the energy flow paths from Figs. 7.2 and 7.3 alone. So I have put the results in a flow diagram – Fig. 7.4. In order to do this, I've summed all quantities over m and n (including $|n| \geq 2$), except that I have left $n = 0$ components out of the sums and shown them separately. For instance, $Q_N(0)$ represents the density fluctuation energy injection at $n = 0$, while $Q_N(!0)$ represents the density fluctuation energy injection for all $n \neq 0$ summed together. Furthermore, the symbol $N(0)$ represents $\sum_m E_N(m, n = 0)$, $N(!0)$ represents $\sum_{m,n\neq 0} E_N(\vec{k})$, etc. Note that every term is summed over m.

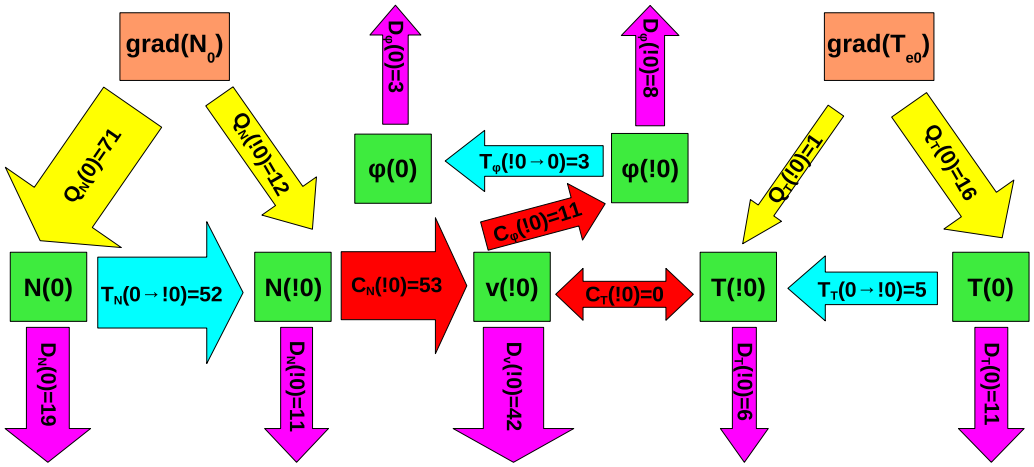

Figure 7.4: Periodic simulation energy flow diagram

The diagram starts at the top with the equilibrium density and temperature profile gradients. They ultimately supply free energy for the fluctuations. Pointing out of them, the yellow Q_j's extract that energy, channeling it to the density and potential fluctuations. The Q_j's are normalized so that they sum to 100 so that each one represents a percentage of energy brought into the system. Clearly, the $n = 0$ components dominate the energy injection from the equilibrium gradients, and the density injection is much stronger than the temperature injection. The blue T_N and T_T three-wave transfers both go in the direction of $n = 0$ to $n \neq 0$. Dissipation occurs for every fluctuation component and takes all of the injected energy out of the system during the quasi-steady-state stage. Next, the red C_N and C_T transfer channels transfer energy from N and T_e to $v_{\|e}$, only at $n \neq 0$, which is the start of the adiabatic response. Actually, $C_T = 0$ because the parallel heat conduction is such a large dissipative factor. Completing the adiabatic response, C_ϕ transfers energy from $v_{\|e}$ to ϕ at $n \neq 0$. Finally, T_ϕ shows axial transfer into $n = 0$ ϕ components.

7.1.3 Nonlinear Instability

Fig. 7.4 provides a look at the way energy flows through the system. The nonlinear instability mechanism can be extracted from a subset of the steps in the flow diagram. I provide a reduced diagram in Fig. 7.5 to isolate the essential interactions of the nonlinear instability mechanism. Notice that I focus only on the density fluctuation side (as opposed to the temperature fluctuation side) because it's clear from the numbers in Fig. 7.4 that the density fluctuations are a much stronger drive for the system than the temperature fluctuations. Again, starting at the top, the $n = 0$ potential fluctuations draw energy from the equilibrium density gradient by advection, depositing that energy into the $n = 0$ density fluctuations. Then, those density fluctuations nonlinearly transfer energy into $n \neq 0$ density fluctuations. Next, the adiabatic response acts to transfer some of that energy into $n \neq 0$ potential fluctuations, which finally nonlinearly transfer energy into the $n = 0$ potential fluctuations.

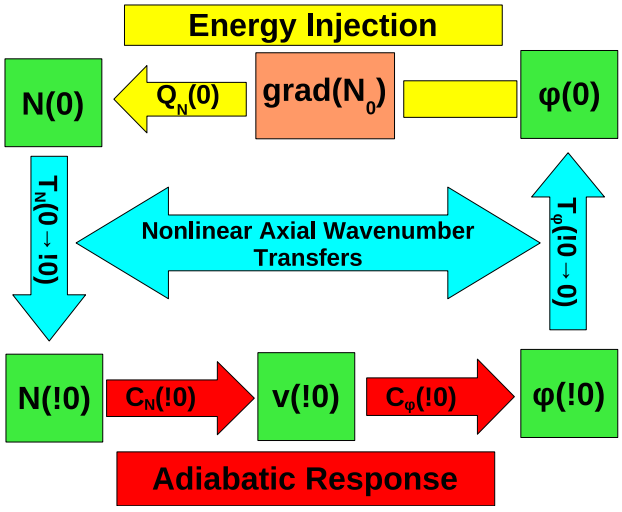

Figure 7.5: Nonlinear instability diagram

Shown in this way, it's clear that the process is self-sustaining. It's also the

dominant process by which the fluctuations get their energy from the equilibrium gradients, which is clear from the fact that $Q_N(n = 0)$ comprises 71% of all of the energy injection. Also, the net direction of T_N (from $n = 0$ to $n \neq 0$) and its large magnitude support this.

To me at least, this came as a big surprise due to my understanding of the unstable linear eigenmode drive paradigm. Given this paradigm, it seems counterintuitive that energy can be injected into the fluctuations at $n = 0$, where only stable linear eigenmodes reside.

The reason why regions in wavenumber space where only stable linear eigenmodes exist can actually inject energy into the system is that the linear eigenmodes are nonorthogonal. Highly nonorthogonal stable eigenmodes may transiently draw energy from an equilibrium as I discussed in Sec. 2.2. To show that this happens in the simulation, I turn off the nonlinearities and observe the energy evolution. I show the total energy as a function of time after turning off the nonlinearities for the $(n = 0, m = 10)$ fluctuations in Fig. 7.6. At early time, the energy grows despite the fact that all of the linear eigenmodes with $n = 0$ are stable. Furthermore, it grows linearly (algebraically) at very early time, consistent with simple model calculations [Wal95]. At late time, the energy drops and doesn't recover. But this is because I have shut off the nonlinearities. As I discussed previously, the energy-conserving nonlinearities mix energy in the system, enforcing the structures which grow transiently, leading to a self-sustaining system of stable nonorthogonal linear eigenmodes. The key to this self-sustaining process is the ability of the linearly stable eigenmodes to transiently draw energy from the equilibrium, which happens in these simulations. This explanation does not take away the necessity of the $n \neq 0$ fluctuations, which are essential in this particular nonlinear instability for allowing access to the adiabatic response, another important step in the self-sustainment process.

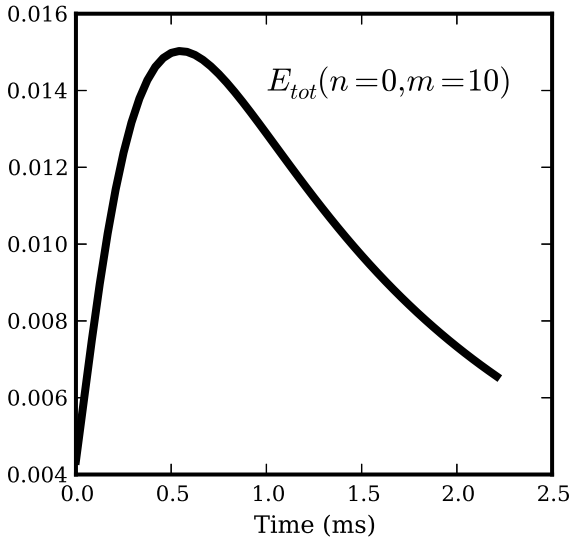

Figure 7.6: Transient linear $n = 0$ growth

7.1.4 n=0 Suppression

I previously introduced the $n = 0$ suppressed simulation in Sec. 5.3, where I discussed the nature of the simulation and some of its statistical properties. I claimed before that this simulation, in which I artificially remove the $n = 0$ components of the density, temperature, and potential fluctuations, eliminates the nonlinear instability. The details of the nonlinear instability mechanism described in the previous section should now make it obvious why removing these components eliminates the nonlinear instability. One may also consider other ways to remove the nonlinear instability while keeping the linear drift wave instability intact. For example, one could remove the $n = 0$ component of the linear drive terms or remove one or more of the nonlinear advection terms, although this would affect quite a bit more than just the nonlinear instability. In any case, my method certainly removes the nonlinear instability mechanism while keeping the linear instability intact, allowing the simulation to act more in the paradigmatic manner.

Rather than showing another diagram of the energy flow for the $n = 0$ sup-

pressed simulation, I present the energy dynamics data in a new, compressed way. That is, I construct a growth rate spectrum from the energy dynamics. I define the growth rate as:

$$\gamma(\vec{k}) = \frac{\partial E_{tot}(\vec{k})}{\partial t}\Big|_{lin} \Big/ \left(2E_{tot}(\vec{k})\right) = \sum_j \left[Q_j(\vec{k}) + D_j(\vec{k})\right] \Big/ \left(2E_{tot}(\vec{k})\right). \quad (7.1)$$

Recall that $\sum_j C_j(\vec{k}) = 0$, so C_j does not appear in this sum. I also only include the linear contribution to $\frac{\partial E_{tot}(\vec{k})}{\partial t}$ so that the growth rate only involves the energy injection and dissipation at each wavenumber and not the three-wave transfers ($T_j(\vec{k}, \vec{k'})$). Adding the three-wave transfers would always make this sum about equal to zero in the turbulent quasi-steady state stage of the simulation anyway, rendering this quantity useless. In the linear stage of the simulations, this method reproduces the linear growth rate spectrum. Specifically, this γ is equivalent to the linear growth rate for the fastest growing branch $n = 1$ eigenmodes. I actually used this γ to generate the curves in Figs. 5.1 and 5.2, though I used other methods to confirm the accuracy of this calculation. γ can also be applied to the turbulent stage of the simulation, in which it gives a composit look at the net energy injection into the system at each $\vec{k}$ normalized by the steady-state energy at that given $\vec{k}$.

Fig. 7.7 shows the results of this calculation for three different cases. First, the light blue (cyan) curves represent $\gamma(m)$ for $n = 1$ (the solid line) and $n = 0$ (the dashed line) for the Periodic simulation during the linear exponential growth stage. The $n = 1$ curve is the same as that shown in Figs. 5.1 and 5.2. The $n = 0$ curve, on the other hand, is the linear growth rate of the $n = 0$ linear eigenmodes, which all have negative growth rates of course. The red curves map out γ for the turbulent stage of the Periodic simulation. The $n = 0$ growth rate is *positive* for low m, while the $n = 1$ growth rate is negative for all m. This isn't surprising given the previous section's evidence for $n = 0$ energy injection due to the nonlinear instability, but it is certainly a nice way to show the contrast

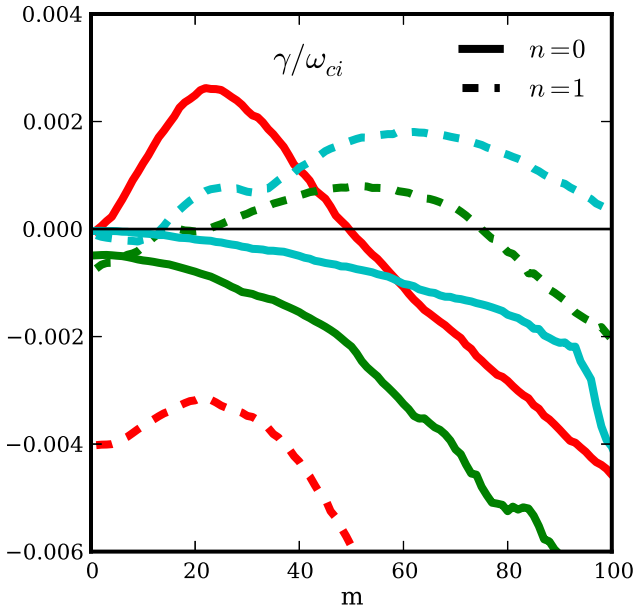

Figure 7.7: Linear vs. nonlinear growth rates

with the linear growth rate curves. The growth rates in the turbulent stage are consistent with the slopes of the transient growth curves like that shown in Fig. 7.6. Finally, the green curves are the growth rates for the $n = 0$ suppressed simulation during the "turbulent phase" (recall from Fig. 5.8 that the fluctuations remain rather coherent, and the state is only weakly turbulent). These growth rates are somewhat similar to the linear growth rates, representative of the expectation under the unstable linear eigenmode paradigm.

Now, one may wonder why there is any $n = 0$ growth rate curve at all for the $n = 0$ suppressed simulation. The reason is because I remove the $n = 0$ components after they are nonlinearly excited. I allow the nonlinearities to transfer energy into the $n = 0$ components at each time step and then I save the data. The energy, by the way, is transferred from $n = 1$ to $n = 0$ modes as in the paradigmatic process. Then, I remove these $n = 0$ components before the equations are evolved again. So there are small values for these $n = 0$ components that come

out in the data, but are not used to evolve the equations. This allows construction of the $n = 0$ growth rate curve. Furthermore, notice that the $n = 0$ suppressed simulation growth rates do not exactly match the linear growth rates. The reason for this is that the nonlinearities change the structures and phases between the fields. Or to put it another way, they excite slower growing or damped eigenmodes that lessen the effect of the most unstable eigenmodes. This is consistent with the linear instability paradigm.

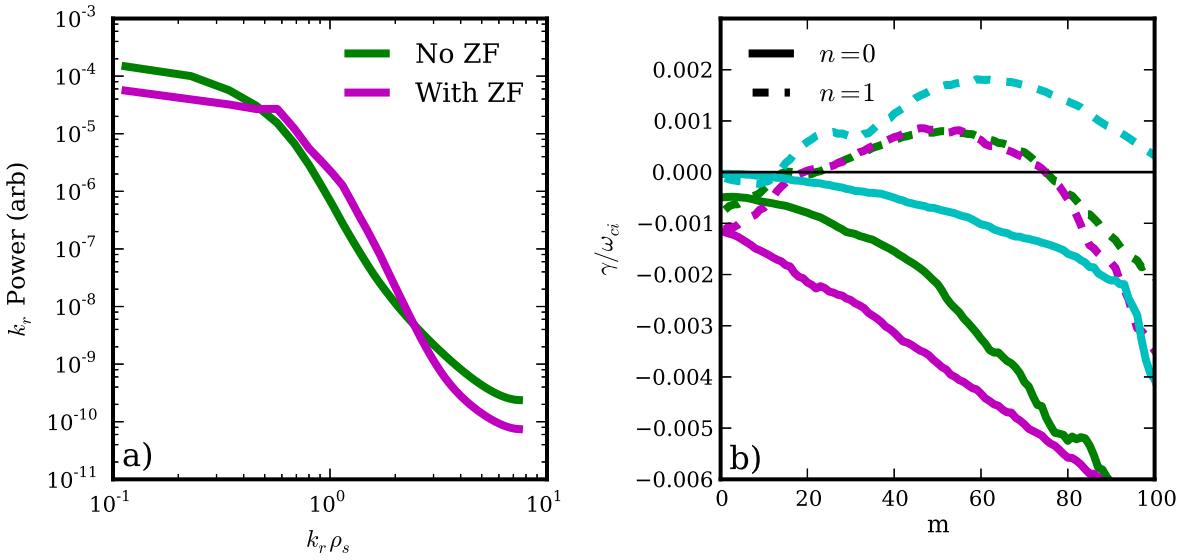

Figure 7.8: Zonal flow affect on spectra and growth rate

Finally, one might notice that manually removing all of the $n = 0$ fluctuation components means that the zonal flows ($n = 0, m = 0$ component of ϕ) are also removed. Zonal flows are often seen as being an important saturation mechanism for turbulence by either shearing the turbulent eddies [BDT90] or by exciting stable eigenmodes [MTK12]. They are often considered to provide the most important nonlinear interactions to plasma turbulence. So one might naively think that their removal in the $n = 0$ suppressed simulation causes the removal of the nonlinear instability. I say "naively" because the nonlinear instability mechanism outlined

in Fig. 7.5 doesn't depend upon zonal flows. But to prove this and to explore the real affect of the zonal flows, I have rerun the $n = 0$ suppressed simulation without removing the zonal flows. I still remove all of the $n = 0$ components of the density and temperature fluctuations and all of the $n = 0, m \neq 0$ components of ϕ, but I leave the zonal flow component intact. I show some comparisons of the two simulations in Fig. 7.8. In Fig. 7.8 a), I show the k_r spectrum of the two simulations, revealing that the zonal flows cause radial wavenumber transfers from low k_r to medium k_r. This is a simple consequence of a three-wave interaction between the dominant low k_r structures and the zonal flows which have finite k_r. This interaction causes a slight saturation effect because the medium k_r modes have lower growth rates than the low k_r modes, and the overall saturation level is depressed by about a factor of 2 when I retain the zonal flows.

Nevertheless, the zonal flows don't cause the nonlinear instability, which is evident from Fig. 7.8 b) where the nonlinear growth rates of the two simulations are shown along with the linear growth rates. Recall from Fig. 7.7 how different the growth rates look when the nonlinear instability is present. The simulation with the zonal flows is qualitatively similar to the simulation without the zonal flows, but as expected, the growth rates with the zonal flows are less than or equal to the growth rates without the zonal flows. Interestingly, the zonal flows only affect the growth rates at $n = 1$ at very low and very high m, but they affect the $n = 0$ growth rates mostly at medium m. Anyhow, the zonal flows don't affect the nonlinear instability, and they also have a relatively weak affect on turbulent saturation compared to some other types of turbulence like ITG turbulence [DBB00, HDC03].

7.2 The Nonlinear Instability in Context

7.2.1 Nonlinear Instability History

Now, after I found this curious nonlinear instability, I wondered if others had previously found this particular mechanism. After all, the equations and the geometry that I use are not new. In fact, a look at Fig. 7.5 reveals that even simpler models like the 3D Hasegawa-Wakatani equations [HW83] contain the proper components to cause the nonlinear instability. And cylindrical simulations of the Hasegawa-Wakatani equations are three decades old (although the original simulations were 2D). My search of the literature reveals that this nonlinear instability was, in fact, identified in 1995. Actually, going even further back, in 1977-1979, Cheng et al. [CO77, CO79] performed 3D turbulence simulations that may have actually been driven by the nonlinear instability. In their work, they identified a dominance of $k_{\|} = 0$ "convective cells [that] are non-linearly excited as a result of mode-coupling of the drift instabilities." It's unclear what equation set they used and what exactly they meant by this mode coupling, but their results seem similar to mine, and it's reasonable to believe that they at least identified the consequences of the nonlinear instability.

In 1995, Biskamp and Zeiler simulated local cylindrical plasma fluid turbulence in the first published use of the 3D Hasegawa-Wakatani equations [BZ95]. Using an energetics analysis, they in fact, correctly identified the nonlinear instability mechanism that drove the $k_{\|} = 0$ structures in their simulations. So the nonlinear instability mechanism is, in fact, not new. Furthermore, others expanded on this original work. Drake et al. showed that elimination of the linear instability by removing the $k_{\|} \neq 0$ components of the linear drive term had virtually no affect on the turbulence [DZB95]. Furthermore, they showed that adding magnetic shear, which also stabilized the linear drift waves, did not stop the turbulence from sustaining itself. Both of these showed that the nonlinear instability could act as

a subcritical instability. Additionally, Scott and others have explore nonlinear drift wave turbulence in a number of different models with different physics effects such as magnetic shear and curvature and found that drift wave turbulence with very long parallel structures tends to sustain itself despite the presence or lack thereof of linear instabilities [Sco90, Sco92, ZBD96, ZDB97, KMN99, Sco02, Sco03, Sco05].

After visually exploring their turbulent simulations, Drake et al. proposed a physical mechanism for the nonlinear instability. The mechanism contains three steps: (1) a radially elongated $k_z = 0$ convective cell radially transports density across the equilibrium density gradient, causing a density fluctuation with an azimuthal density gradient. (2) Radially propagating drift waves with $k_z \neq 0$ grow on this density gradient. (3) The flows associated with these drift waves reinforce the original radial flows of the convective cell. They went on to simulate this mechanism in a reduced equation set, using a finely crafted initial state to show the growth of the structures involved in the mechanism. It's not difficult to see that this mechanism is the same one that I described using Fig. 7.5, though my description used modal energy transfer language while Drake's uses the language of flows and drift waves. Furthermore, he lumped together my two middle steps into his single middle step. Nevertheless, our explanations are equivalent.

Drake et al. cleverly used their physical insight to develop a reduced turbulent model, consisting of only three modes: a $k_z = 0$ radially elongated mode, a $k_z \neq 0$ drift wave with finite radial and azimuthal wavenumbers, and a second $k_z \neq 0$ drift wave with higher azimuthal wavenumber with a phase such that its interaction with the other drift wave drives the $k_z = 0$ mode. The electrostatic potential resulting from these modes is given by the expression

$$\phi = \phi_0 \cos(\pi y) + [\phi_1 \cos(\pi y) + \phi_2 \sin(2\pi y)] \times \sin(k_z z) \exp(i k_x x). \tag{7.2}$$

The evolution of these modes can be calculated by insertion of this expression

into the evolution equations (such as Eqs. 4.1 and 4.3). Further simplifying the resulting equations, they calculated that the $k_z = 0$ mode would grow with an algebraic time dependence of $t^{4/3}$ (they didn't have any dissipation in the model to stop the growth). Such an algebraic time dependence is consistent with the notion of non-normal transient growth [Wal95]. They didn't make this connection, but in light of my Fig. 7.6 and general properties of non-normal subcritical turbulence, this isn't a surprising result.

Later, Krommes, noted the similarity between Drake's self-sustainment mechanism and the mechanism of turbulent self-sustainment in subcritical hydrodynamic flows like Poisuille pipe flow [Kro99]. The self-sustainment mechanism in hydrodynamic flows is the following: (1) advection of mean shear by weak streamwise rolls (vortices) which create streaks (spanwise velocity fluctuations); (2) secondary instability of the resulting streaks; (3) nonlinear self-interaction of the streaks that re-energizes the original streamwise rolls. The streamwise rolls are elongated $k_z = 0$ structures. Furthermore, the first step is a linear interaction, called the 'lift-up' mechanism, which relies on nonorthogonal eigenmodes that grow transiently with algebraic dependence [TTR93, Wal95, Hen96]. This self-sustainment mechanism is analagous to the Drake plasma mechanism with the caveat that a secondary drift wave instability in the plasma case replaces the wake-like instability in the neutral fluid case. Such a correspondence between the two mechanisms led Krommes to suggest using mathematical techniques and conclusions from the neutral-fluid studies to further study the plasma mechanism. Krommes and others also tried to expand on Drake et al.'s reduced model. That work never seems to have been published (to my knowledge), but their method was to extract a low-order dynamical system that exhibits the critical self-sustainment mechanism. Krommes claims that numerical simulations of the low-order systems produced, in some regimes, chaotic orbits similar to the Lorenz attractor.

I further note here a curious connection between the aforementioned work and

studies done on LAPD. In LAPD, the frequency spectra sometimes have an exponential shape, which has been linked to the presence of Lorentzian-shaped pulses in the time signals [PSM08a, PSM08b]. In an attempt to recreate these numerically, Shi et al. prescribed a potential field, much like Drake's of Eq. 7.2, except that this field was two-dimensional without any z dependence and used two drift wave modes rather than three modes like Drake [SPM09]. Shi's low-dimensional model produced the Lorentzian-shaped pulses in the time signals. Maggs and Morales later connected the Lorentzian pulses to deterministic chaos and explained why deterministic chaos produces such shaped pulses [MM11, MM12b, MM12a]. They showed that broadband turbulence (at least the frequency spectra) can be the result of low-order chaotic systems. The connection between this work and Drake's and Krommes's is tenuous at this point. But can the few basic modes of Drake's mechanism create all the turbulence in LAPD, and does the turbulence in LAPD and other machines work in the same basic way as the turbulence in neutral-fluid systems?

CHAPTER 8

Energy Dynamics for the Non-periodic Simulations

I turn my focus in this chapter to the simulations with non-periodic axial boundary conditions; namely the Dirichlet, Neumann, and Sheath simulations. I showed in Sec. 5.1 that the linear properties of these simulations are rather different from the Periodic simulation and from one another. However, the statistical turbulent properties of the four simulations are all quite similar (Sec. 5.3). This, combined with the observation that the turbulence in the Periodic simulation self-organizes and drives itself by nonlinear instability, points to the conclusion that the axial boundary conditions have little affect on the nonlinear instability or the energy dynamics in general. Nevertheless, additional supporting evidence for this claim can provide confirmation regarding the robustness of the nonlinear instability. I therefore explore the energy dynamics of the non-periodic simulations in this chapter, attempting to differentiate the nonlinear dynamics from the linear ones.

8.1 Fourier Decomposing Non-periodic Functions

To my knowledge, nobody has considered the affect of non-periodic axial boundary conditions on this nonlinear instability in a straight magnetic field. But this is a critical extension of the topic because in the real world, linear plasma devices don't have periodic boundary conditions. Additionally, the nonlinear instability seems to crucially depend on axial wavenumber dynamics, which should be affected by

the axial boundary conditions. It is perhaps surprising then that nobody has taken up this line of research.

On the other hand, it may not be so surprising given that the non-periodicity can cause interpretation issues regarding the linear vs. the nonlinear instability. To clarify, in the periodic case, the linear eigenmodes are sinusoildal with integer axial mode numbers. And all of the unstable eigenmodes have $|n| \geq 1$. So any energy injection into $n = 0$ fluctuations is a clear indication that the unstable linear eigenmodes are not responsible for such injection. In the non-periodic cases, the linear eigenmodes are not necessarily sinusoidal (see Fig. 5.2 b)) and if they are, they certainly don't have integer mode numbers. Fourier decompositions of the non-periodic unstable eigenmodes yields finite $n = 0$ Fourier coefficients. This can muddle interpretation of energy injection into $n = 0$ fluctuations during the turbulent simulation phase. It seems as though a linear eigenmode decomposition may fix this problem, but these decompositions are difficult to perform in practice, and more importantly, decompositions with highly non-normal bases aren't guaranteed to yield interpretable results. So I proceed with the spectral energy dynamics on non-periodic simulations and show that the results are less clear-cut than those of the Periodic simulation, but nevertheless, rather conclusive in that the nonlinear instability still dominates.

First, however, I raise another problem regarding spectral energy dynamics and spectral analysis in general. That problem is Gibbs phenomena. Fourier basis functions are continuous and periodic, so Fourier decomposing discontinuous or non-periodic functions leads to Gibbs phenomena. One of the significant results of this is the slow convergence of Fourier reconstructions to the original signal. Mathematically, I can take a discrete signal with the following Fourier decomposition:

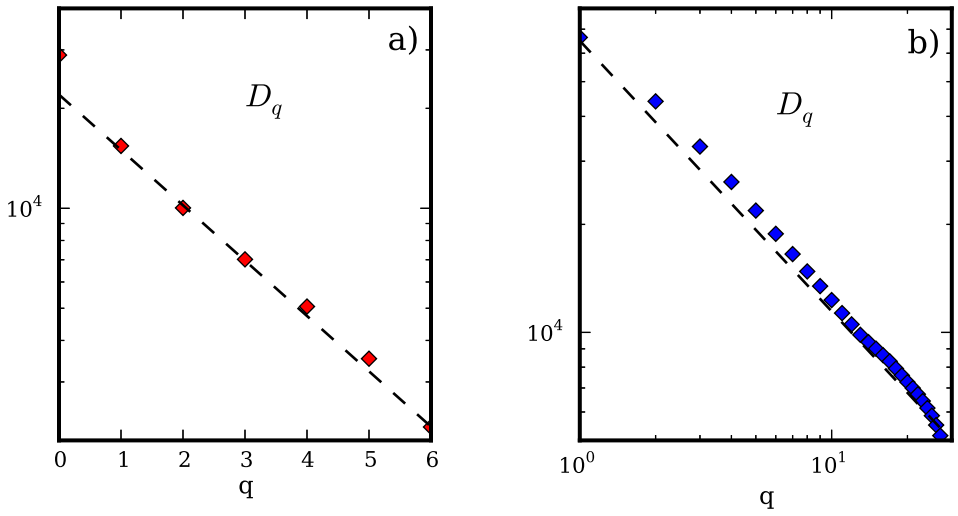

Figure 8.1: Convergence of Fourier reconstructions

$$f(x) = \sum_{k=-Q}^{Q} \hat{f}_k e^{2\pi i k x}, \tag{8.1}$$

where the $\hat{f}_k$ are ordered in the sum by the size of their absolute value with $\hat{f}_0$ being the largest Fourier coefficient. The Fourier reconstruction of order $q < Q$ is then:

$$g_q(x) = \sum_{k=-q}^{q} \hat{f}_k e^{2\pi i k x} \tag{8.2}$$

There are several types of convergences of the g_q, one of which is the $L1$ norm. Defining the difference between the original signal and the Fourier reconstruction of order q as $D_q = \sum_x |f(x) - g_q(x)|$, I can look at the convergence of D_q as a function of q. For continuous periodic signals, D_q converges exponentially, while it only converges algebraically (power law) for non-periodic or discontinuous signals.

As an example, I have plotted D_q for the Periodic and Sheath simulations in Fig. 8.1. The Periodic simulation in Fig. 8.1 a) converges exponentially, while the Sheath simulation in Fig. 8.1 b) converges algebraically. Now in this figure, even

though the x-axis label q indicates the mode with the q^{th} largest amplitude by construction of Eq. 8.2, it also happens to correspond to the axial mode number n for all but the last few q. In other words, in both simulations, most of the energy is contained in $n = 0$ modes followed by $n = 1$ modes and so on. So I should still be able to focus on the $n = 0$ and $n = \pm 1$ mode numbers in the energy dynamics data, but they will not contain as much of the dynamics as they do for the Periodic case.

8.2 Energy Dynamics Results

The simplest way to view the vast quantities of energy dynamics information is through the effective growth rate defined in Eq. 7.1. So in Fig. 8.2, I show the growth rates for all of the simulations. In Fig. 8.2 a), I plot the growth rates during the turbulent phases of all five simulations (see Fig. 5.8 for the color code). Again, I break up the $n = 0$ and $n = 1$ components and don't show the $n \geq 2$ growth rates. Notice that the Periodic, Dirichlet, Neumann, and Sheath simulations all have quite similar growth rates, especially at $n = 0$. Their $n = 1$ growth rates have similar m dependencies, but somewhat different magnitudes, and the $n = 1$ growth rates are all negative except for a small region in the Dirichlet curve, which is marginal. Contrast these with the $n = 0$ suppressed simulation, which recall, is dominated by the linear instability. These growth rates certainly indicate that the same kind of processes occur for the four similar simulations regardless of axial boundary conditions – namely, the nonlinear instability process. This isn't too surprising given the similarity of the turbulent statistics of the four simulations (Fig. 5.8).

It is also instructive to compare the nonlinear turbulent growth rates against the linear growth rates as I did for the Periodic simulation in Fig. 7.7. I do this for the non-periodic simulations in Figs. 8.2 b)-d). The black curves in these

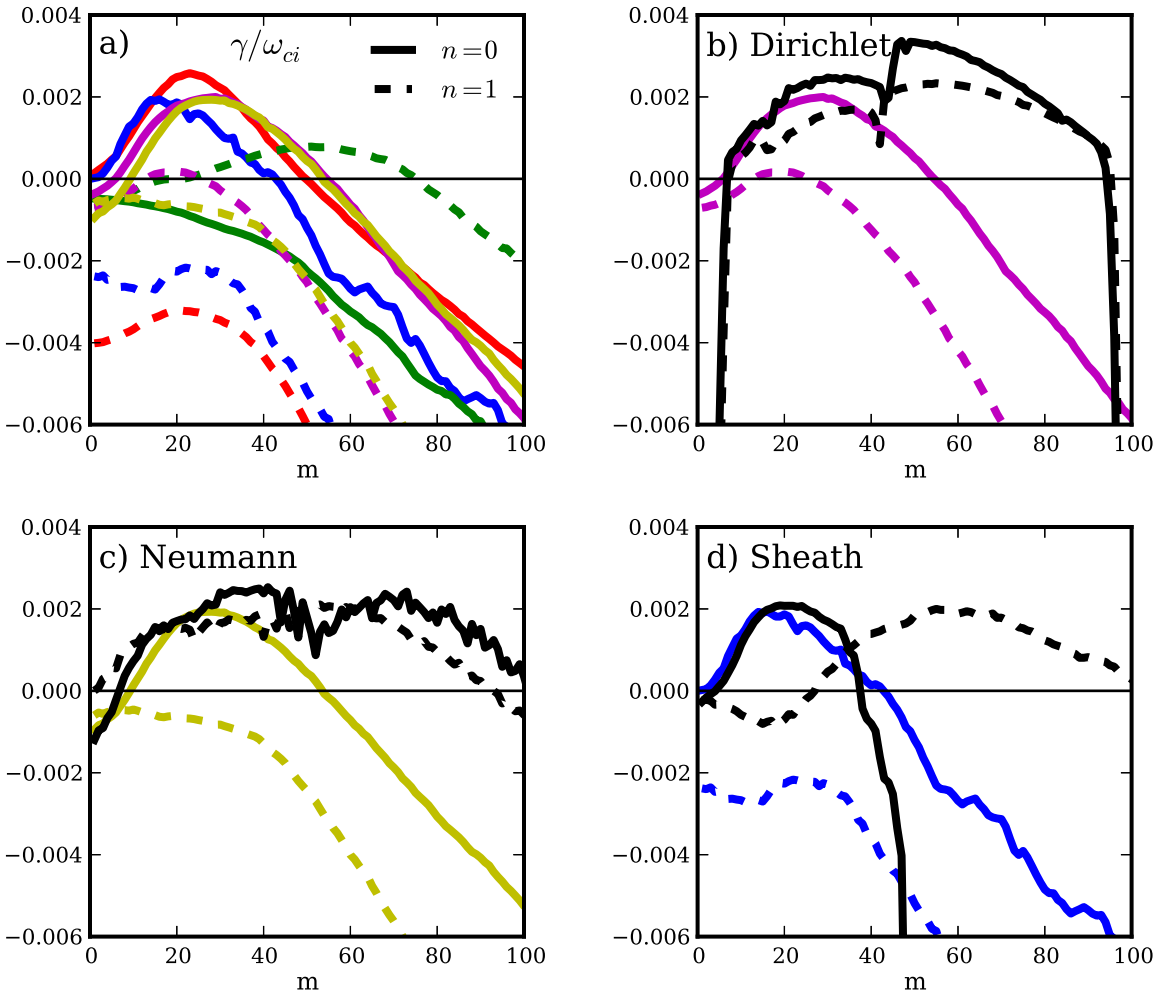

Figure 8.2: Linear and nonlinear growth rates of all simulations

figures are the linear growth rates for each respective simulation. For example, the solid black line in Fig. 8.2 b) corresponds to the $n = 0$ linear growth rate of the Dirichlet simulation. The dashed black line in this figure corresponds to the $n = 1$ growth rate of the Dirichlet simulation. Note that the linear growth rates come from the same data as that used in Fig. 5.2, but these are decomposed in m and n, while those were simply decomposed in m.

Now all three of these simulations (Dirichlet, Neumann, and Sheath) have a lot of similarity, especially the Dirichlet and Neumann simulations. The $n = 1$ growth rate curves for all three simulations are all qualitatively different between the linear and the nonlinear stage. For the most part, the $n = 1$ linear growth rates are always positive, while the $n = 1$ nonlinear growth rates are always negative. The $n = 0$ linear growth rates for the Dirichlet and Neumann simulations are similar to the $n = 1$ linear growth rates because the linear eigenmode structures contain roughly equal parts $n = 0$ and $n = 1$ and the density-potential phases are set by the linear drift-wave physics. The $n = 0$ and $n = 1$ Sheath simulation linear growth rates are quite different because the linear eigenmodes actually undergo a bifurcation at $m \sim 40$. All $m < 40$ Sheath linear eigenmodes have shapes like that in Fig. 5.2 b), which are even about the axial midpoint. However, all $m > 40$ linear eigenmodes have shapes that are odd about the axial midpoint. The CWM has even and odd solution branches whose growth rates cross at $m \sim 40$, causing this seemingly odd behavior.

In any case, it is interesting that the $n = 0$ linear and nonlinear growth rates for these three simulations are nearly equal for $m < 50$. However, they are not at all similar for $m > 50$. Does this low m region of similarity indicate that the linear instability dominates these simulations? Based on Fig. 8.2 a), the $m > 50$ region, and the $n = 1$ dissimilarity, I would say that the nonlinear instability is still the dominant player. However, it's not conclusive either way, and it's possible that in some complicated way, the linear and nonlinear physics are somewhat similar in this region. This is the problem of using Fourier decompositions rather than linear eigenmode decompositions, although as I stated before, there's no guarantee that an eigenmode decomposition would yeild anything more conclusive because of the eigenmode nonorthogonality. Eigenmode nonorthogonality is the real culprit to all of the difficulties, in fact. It causes the nonlinear instability, but it also makes it difficult to identify in some cases. Therefore, I try to devise a way around this

in the next section.

8.3 Linear vs Nonlinear Structure Correlation

To try to sort out the problem of linear vs. nonlinear instability in a non-normal linear system, I propose the following method. First, imagine the case where a simulation is dominated by a linear instability. Then, the fastest growing linear eigenmode dominates the system, nonlinearly transfering some energy to more weakly unstable or even stable eigenmodes. In this case, a large portion of the energy should remain in the fastest growing linear eigenmode [HTJ11]. In the alternative case where a nonlinear instability is dominant, the linear eigenmode should have little bearing on the structure of the turbulence and therefore little energy should be contained in this eigenmode. Therefore, a reasonable gauge of whether a linear or nonlinear instability dominates a system is the fraction of energy in a turbulent system that is contained in the fastest growing linear eigenmode. This may be calculated by projecting the fastest growing eigenmode onto the turbulent state.

Formally, in my model, I fully describe the turbulent state by four independent fields, which I can appended into a single vector of the spatio-temporal field functions: $\boldsymbol{f}_{turb}(\vec{r},t) = \{N(\vec{r},t), T_e(\vec{r},t), \nabla_\perp\phi(\vec{r},t), v_{\|e}(\vec{r},t)\}$. This vector may be decomposed in a complete basis:

$$\boldsymbol{f}_{turb}(\vec{r},t) = \sum_{i,m} c_{i,m}(t)\boldsymbol{\psi}_{i,m}(r,z)e^{im\theta}, \tag{8.3}$$

where $\boldsymbol{\psi}_{i,m}(r,z)$ are time-independent spatial complex basis functions of the form $\boldsymbol{\psi}_{i,m}(r,z) = \{n_{i,m}(r,z), t_{i,m}(r,z), \nabla_\perp\phi_{i,m}(r,z), v_{i,m}(r,z)\}$, and $c_{i,m}(t)$ are the complex time-dependent amplitudes. I have explicitly imposed a Fourier bases for the θ dependence of the basis functions. The total number of linearly independent

basis functions is the number of total grid points used in the simulation times the number of independent fields, which is four in this case. Now, $\boldsymbol{\psi}_{i,m}(r,z)$ can be any linearly independent set of functions and need not be the linear eigenfunctions of the system. In fact, I want to use orthogonal basis functions, ruling out the linear eigenfunctions. However, it is quite useful to set $\boldsymbol{\psi}_{0,m}(r,z)$ to the fastest growing linear eigenmode because this is the structure of interest that is to be projected onto the turbulence. The other $\boldsymbol{\psi}_{i\neq 0,m}(r,z)$ comprise the remainder of the orthonormal basis, and they must be different from the remaining linear eigenfunctions in order to complete the orthogonal basis. It isn't necessary for the purpose of this study to actually compute these other basis functions, but if I were to compute them, I would probably start with all of the linear eigenmodes and perform a Gram-Schmidt orthogonalization procedure, making sure to start with the fastest growing eigenmode in order to preserve it. Using this procedure, Hatch et al. [HTJ11] found that a significant fraction ($\sim 50\%$) of the energy in a turbulent state of ITG turbulence was contained in the fastest growing linear eigenmode at each perpendicular wavenumber. Such a result, however, doesn't require knowledge of the other basis functions, and thus I don't compute them here.

Now, to compute the fraction of energy in the fastest growing eigenmode to the total energy, I first define an inner product that is energetically meaningful and that sets the orthonormality of the basis functions:

$$\langle \boldsymbol{\psi}_{i,m}, \boldsymbol{\psi}_{j,m} \rangle = \int w \boldsymbol{\psi}^*_{i,m} \cdot \boldsymbol{\psi}_{j,m} dV = \delta_{i,j}. \tag{8.4}$$

The weighting w is such that $\langle \boldsymbol{f}_{turb}, \boldsymbol{f}_{turb} \rangle = E_{turb}$. Now from Eqs. 8.3 and 8.4, $\langle \boldsymbol{f}_{turb}, \boldsymbol{f}_{turb} \rangle = E_{turb} = \sum_{i,m} |c_{i,m}|^2$ and $\langle f_{turb,m}, f_{turb,m} \rangle = E_{turb,m} = \sum_i |c_{i,m}|^2$. Then, the amount of energy contained in the fastest growing mode (for each m) is given by the square of the projection of the mode onto the turbulence: $E_{0,m} = |\langle \boldsymbol{\psi}_{0,m}, f_{turb,m} \rangle|^2 = |c_{0,m}|^2$. The ratio $R_m = E_{0,m}/E_{turb,m}$ is a measure of

the fraction of turbulent energy contained in the fastest growing linear eigenmode.

Of course, $E_{turb,m}$ is easily calculated from the turbulent state, but $E_{0,m}$ in the turbulent state can only be found with knowledge of the fastest growing eigenfunction. The fastest growing eigenfunction, though, can be found easily by running a simulation from a random or turbulent state with all of the nonlinearities removed from the model equations. After some time, the fastest growing eigenfunctions will come to dominate the fluctuation structure. Then, a Fourier decomposition in m space will separate the fastest growing eigenfunctions at each m, including the real and imaginary part of the eigenfunctions (up to a time dependent complex constant, which is removed by normalizing the eigenfunction). I can then project the eigenfunctions onto the turbulent state with the inner product defined in Eq. 8.4, giving $E_{0,m}$.

I do this and show the ratio R_m in Fig. 8.3 for the five simulations. For the most part, the simulations other than the $n = 0$ suppressed one have a small value of the ratio ($R_m < 0.3$) for all m. This confirms that the turbulence largely self-organizes without regard to the linear physics in the four other simulations. The one exception is the Dirichlet simulation for $m > 50$, which has $R_m \sim 0.5$. This is quite the unexpected result, and I can't explain it based on any of the other evidence. Most of the energy in this and the other simulations, however, is at low m (Fig. 7.1), so these larger m eigenmodes don't make a large impact on the overall structure of the turbulence.

In fact, R_m is below 0.1 for $m < 40$ for the periodic, Dirichlet, and Neumann simulations, precisely the area where $n = 0$ structures dominate the energy spectrum. This answers the question posed in the previous section regarding the similarity in the $n = 0, m < 40$ linear and nonlinear growth rates for the Dirichlet and Neumann simulations. The fastest growing linear eigenmodes do not significantly drive the turbulence in this region. The nonlinear instability does.

On the other hand, the fastest growing eigenfunctions make up a significant

fraction of the energy in the $n = 0$ suppressed simulation. Where the linear drift wave instability (and the turbulent growth rate) is the strongest (at $m \sim 50$), $R_m \sim 0.5$. The linear physics controls the $n = 0$ suppressed simulation, and the linear eigenmode structure certainly asserts itself in the turbulence, but only to a degree (50%).

The Sheath simulation is the most difficult to analyze because it has more linear eigenmode dominance at low m than the other simulations. R_m is still only about 0.25 there. While this isn't at the level of the $n = 0$ suppressed simulation or the Hatch et al. gyrokinetic ITG simulation [HTJ11], it still might be significant. It appears that the linear instability never completely disappears from any of the simulations, and the level to which it acts on the turbulence differs between the different simulations. The Sheath simulation is driven more by its linear instability than all of the others except for the $n = 0$ suppressed simulation, indicating a possibly important role for the CWM in LAPD, though LAPD doesn't have such simple boundary conditions. However, the turbulence statistics of the Sheath simulation are so similar to those of the other simulations (Sec. 5.3) that $R_m \sim 0.25$ probably isn't significant enough to say that the linear instability dominates.

8.4 Nonlinear Saturation Levels

A common topic of plasma turbulence is the prediction of the saturation level of turbulence. Generally, such predictions are based off of linear properties, however, a dominant nonlinear instability should have an affect on the level at which the turbulence saturates. One theory – mixing length theory – based on linear drift waves predicts that the saturation level should be about $\gamma/k_\perp^2$ where γ and $k_\perp$ are the growth rate and perpendicular wavenumber of the fastest growing linear eigenmode [Hor90]. Turbulence driven by a nonlinear instability may saturate at

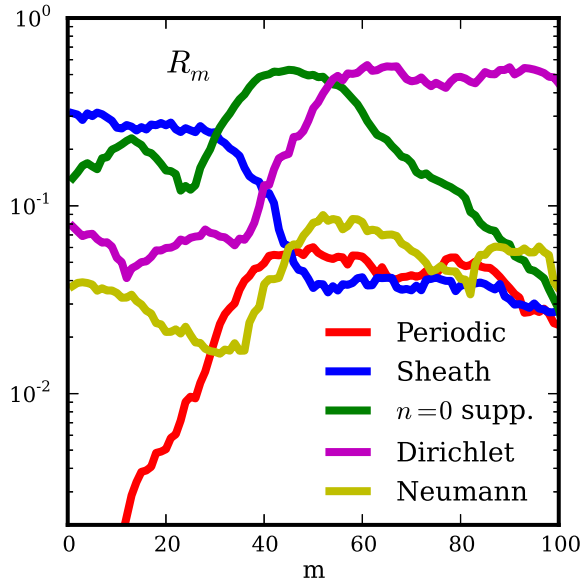

Figure 8.3: Energy fraction contained in the most unstable eigenmodes

some other level, which seems probable given Fig. 5.8, which shows that the $n = 0$ suppressed simulation saturates at a lower level than the simulations driven by the nonlinear instability.

Mixing length theory provides an estimate for the turbulence saturation level where only properties of the linear eigenmodes are known. This can be quite useful to find scaling relations, and allows prediction without direct numerical simulation. Therefore, I develop a corresponding estimate based on the drift wave turbulence driven by the nonlinear instability that I have described. Now, it is quite difficult to predict a saturation level based on a nonlinear mechanism when nonlinear simulation results are not available. However, as suggested in Ref. [CO79], and as seen in Fig. 5.4 b), it appears that the turbulence begins to saturate when the amplitude of the $n = 0$ field components becomes equal to the $n = 1$ field components. At this point, the strongest nonlinear interaction term catches up to the linear terms, bringing about the onset of saturation. However, the nonlinear instability really doesn't become important up until this point, which

is why saturation occurs only when values are a few times higher than this point. Therefore, this crossing point can only be seen as a rough approximation for the saturation level, and more work will be needed to improve upon this calculation.

Now in order to find the crossing point amplitude, notice from Fig. 5.4 b), that before the components become equal, in the linear phase of the simulation, the $n = 0$ components seem to have twice the growth rate of the $n = 1$ components. This indicates that the $n = 0$ components are driven nonlinearly (parametrically). Furthermore, both are exponentially growing in the linear phase. It is possible then to use only linear eigenmode knowledge to compute the level at which the $n = 0$ and $n = 1$ components become equal as long as both start at small amplitudes and experience a few e-foldings before saturating. To find the crossing point, I first derive an expression for the time evolution of the linear eigenmode amplitudes. According to Drazin [DR81], such an evolution for the linear eigenmode A_j should take the form:

$$\frac{dA_j}{dt} = s_j A_j + N_j(A_k) \tag{8.5}$$

where the complex function N_j of the A_ks represents the nonlinear action of all the k modes on the jth (including the self-interaction). I now derive such an equation for my model set, finding the explicit forms for s_j and N_j.

8.4.1 Linear Eigenvector Amplitude Evolution

The linear eigenvectors are fixed composit objects of the independent fields ($N, v_{\|e}, \phi$ and T_e). Each one has a fixed complex-valued spatial structure where the different fields have a certain amplitude and phase relationship between each other. Each one evolves in time under the linear equation set with a fixed frequency and growth rate. Eigenmode structures of global simulations have radial and axial shapes that are not described by well-known functions like sines and cosines or

Bessel functions. So to simplify matters, I use a local model in which each linear eigenmode can simply be identified by its wavevector $\vec{k} = (k_r, k_\theta, k_z)$. Then number of eigenvectors at each $\vec{k}$ is equal to the number of fields – 4 in my case.

Formally, the local fully spectral version of Eqs. 4.1- 4.4 can be written as

$$\frac{\partial \boldsymbol{\xi}_{\vec{k}}}{\partial t} = \mathbf{M}_{\vec{k}} \cdot \boldsymbol{\xi}_{\vec{k}} + \sum_{\vec{k}'} (k_r k'_\theta - k'_r k_\theta) \boldsymbol{\xi}_{\vec{k}'} \phi_{\vec{k}-\vec{k}'}, \tag{8.6}$$

where

$$\boldsymbol{\xi}_{\vec{k}} = \begin{pmatrix} N_{\vec{k}} \\ v_{\parallel e\vec{k}} \\ \phi_{\vec{k}} \\ T_{e\vec{k}} \end{pmatrix},$$

$$\mathbf{M}_{\vec{k}} = \begin{pmatrix} -\mu_N k_\perp^2 & -ik_z & -\frac{ik_\theta}{L_N} & 0 \\ -\frac{ik_z m_i}{m_e} & -\nu_e & \frac{ik_z m_i}{m_e} & -1.71\frac{ik_z m_i}{m_e} \\ 0 & \frac{ik_z}{k_\perp^2} & -\nu_{in}\mu_\phi k_\perp^2 & 0 \\ 0 & -1.71\frac{2}{3}ik_z & -\frac{ik_\theta}{L_T} & -\frac{2}{3}\kappa_{\parallel e}k_z^2 - \frac{2m_e\nu_e}{m_i} - \mu_T k_\perp^2 \end{pmatrix}$$

where I have used $\partial_r N_0 = -1/L_N$ in accordance with the local approximation, and I have neglected the sources, which are only nonzero for $k_r = k_\theta = 0$ in any case. The final term on the RHS is the nonlinear advection contribution. Without this, the system is linear, constituting a linear eigenvalue problem:

$$\frac{\partial \boldsymbol{\rho}_{\vec{k},j}}{\partial t} = -i\omega_{\vec{k},j} = \mathbf{M}_{\vec{k}} \cdot \boldsymbol{\rho}_{\vec{k},j} \tag{8.7}$$

where $\omega_{\vec{k},j}$ and $\boldsymbol{\rho}_{\vec{k},j}$ are the eigenvalues and eigenvectors of $\mathbf{M}_{\vec{k}}$. j is an index that goes from 1 to 4, since there are 4 linear independent eigenvectors for each $\vec{k}$. I note that the linear matrix $\mathbf{M}_{\vec{k}}$ is not normal; therefore, the eigenvectors are not orthogonal. This can be a problem for eigenvector decompositions. However, the *left* eigenvectors are orthogonal to the right eigenvectors: $\mathbf{l}_{\vec{k},i}^T \boldsymbol{\rho}_{\vec{k},j} = \delta_{i,j}$, where

$$\mathbf{l}^T_{\vec{k},i} \cdot \mathbf{M}_{\vec{k}} = -i\omega_{\vec{k},j}\mathbf{l}^T_{\vec{k},i}. \tag{8.8}$$

Now decomposing the spectral vectors $\boldsymbol{\xi}_{\vec{k}}$ with the linear eigenvectors:

$$\boldsymbol{\xi}_{\vec{k}} = \sum_{j=1}^{4} A_{\vec{k},j}\boldsymbol{\rho}_{\vec{k},j} \tag{8.9}$$

where $A_{\vec{k},j}$ are the time-dependent eigenmode amplitude coefficients, I substitute this decomposition into Eq. 8.6:

$$\sum_j \boldsymbol{\rho}_{\vec{k},j}\frac{\partial A_{\vec{k},j}}{\partial t} = \sum_j A_{\vec{k},j}\mathbf{M}_{\vec{k}} \cdot \boldsymbol{\rho}_{\vec{k},j} + \sum_{\vec{k'},j} A_{\vec{k'},j}(k_r k'_\theta - k'_r k_\theta)\boldsymbol{\rho}_{\vec{k'},j}\phi_{\vec{k}-\vec{k'}}. \tag{8.10}$$

Contracting this equation on the left by the left eigenvector $l_{\vec{k},i}$ and using the eigenvector orthogonality gives

$$\frac{dA_{\vec{k},i}}{dt} = -i\omega_{\vec{k},i}A_{\vec{k},i} + \sum_{k'} A_{\vec{k'},i}(k_r k'_\theta - k'_r k_\theta)\phi_{\vec{k}-\vec{k'}}. \tag{8.11}$$

This has the Drazin form of Eq. 8.5 with s_j as the complex linear eigenfrequencies and the N_j as a form indicative of three-wave interactions from nonlinear advection. With this, I proceed to find the amplitude at which the $n = 0$ eigenmodes cross with the $n = 1$ eigenmodes.

8.4.2 Mixing Length Approximation

To begin, I apply Eq. 8.11 to the fastest growing drift wave in the linear phase of the simulation before the $n = 0/n = 1$ crossing. The $n = 1$ fastest growing eigenmode curve, which has $m \sim 60$, evolves as:

$$\frac{dA_d}{dt} = -i\omega_d A_d \tag{8.12}$$

where A_d represents the fastest growing $n = 1, m \sim 60$ linear drift wave structure with time-dependent amplitude (d is shorthand for the wavevector of this eigenmode). Note that I have made the assumption that in the linear phase of the simulation, the linear term dominates the nonlinear term, which is quadratic in two small quantities. The solution of this equation is:

$$A_d(t) = A_d(0)e^{-i\omega_d t}. \tag{8.13}$$

On the other hand, the $n = 0$ mode has much smaller amplitude than the linear drift wave during the linear simulation phase, meaning that the nonlinear term can be comparable to or larger than the linear term. Specifically, the evolution equation for the $n = 0$ "convective cells" is:

$$\frac{dA_c}{dt} = -i\omega_c A_c + \sum_{\vec{k'}} (k_{rc}k'_\theta - k'_r k_{\theta c}) A_{\vec{k'}} \phi_{c-\vec{k'}}. \tag{8.14}$$

Now, the convective cells that nonlinearly grow the fastest have $m \sim 0$. This is clear by noting that the largest term in the sum should have $\vec{k'} = d$ and $c \sim 0$. Using the symbol M_{cd} for the wavevector difference $k_{rc}k_{\theta d} - k_{rd}k_{\theta c}$ and noting that $\phi_{-d} = \phi_d^* \sim A_d^*$,

$$\frac{dA_c}{dt} \approx -i\omega_c A_c + M_{cd}|A_d|^2. \tag{8.15}$$

Plugging in Eq. 8.13 into the A_d in this equation, and then solving this differential equation for $A_C(t)$ results in:

$$A_c(t) = A_c(0)e^{-i\omega_c t} + \frac{M_{cd}|A_d(0)|^2}{2\gamma_d + i\omega_c} \left(e^{2\gamma_d t} - e^{-i\omega_c t}\right). \tag{8.16}$$

Now a large simplifying approximation is that $\omega_c = 0$. I essentially take the linear eigensystem of these convective cells to have zero axial wavenumber, zero

frequency and growth rate, near-zero azimuthal wavenumber, and radial wavenumber about twice that of the drift wave radial wavenumber. All of these assumptions are confirmed by the spectra of the convective cells and drift waves (not shown here). Also, these mean that $k_{rc}k_{\theta d} \gg k_{rd}k_{\theta c}$, so that $M_{cd} \approx k_{rc}k_{\theta d}$ Then,

$$A_c(t) = A_c(0) + \frac{k_{rc}k_{\theta d}|A_d(0)|^2}{2\gamma_d}\left(e^{2\gamma_d t} - 1\right). \tag{8.17}$$

At the time (t_f), when the amplitudes of the drift waves and convective cells equal one another, the initial perturbation $A_c(0)$ is much smaller than the second term on the right hand side of Eq. 8.17 and can therefore be neglected when looking at large times. While this doesn't have to be true in general, it is true if the initial perturbations are set small enough. In fact, if the initial perturbations are not set to be small enough, the convective cells will not necessarily grow nonlinearly before saturating – they could grow transiently due to the nonorthogonality of the linear eigenmodes [CTC98, CPB09]. So, setting the amplitude of $A_d(t_f)$ from Eq. 8.13 to the amplitude of $A_c(t_f)$ from Eq. 8.17 and performing some algebra, the result is:

$$|A_c(t_f)| = |A_d(t_f)| = \frac{2\gamma_d}{k_{rc}k_{\theta d}}. \tag{8.18}$$

The factor of two probably isn't significant given the approximations that went into this result, but the scalings of the drift wave growth rate, the drift wave azimuthal wavenumber, and the convective cell radial wavenumber are. The result is very similar to the mixing length result except that the wavenumbers of interest are from both the drift waves and the convective cells rather than from just the drift waves. Putting in LAPD values for this relation gives that the crossing level amplitude should be about 0.05. This is consistent with the amplitude at which the simulations begin to saturate, as can be seen in Fig. 5.4 a). Again, though, the ultimate saturation level is somewhat larger than this, and it's not clear if that

ultimate saturation level can be completely predicted without direct numerical simulation.

One last point I want to make involves the $n \geq 2$ curves in Fig. 5.4 b). These curves all appear to grow at the same growth rate as the $n = 1$ curve during the linear stage of the simulation. This may seem odd because the linear growth rates of the eigenmodes with these higher axial mode numbers are much less than the growth rate of the fastest $n = 1$ eigenmode. Furthermore, if these modes were to be pumped nonlinearly (parametrically), one might expect them to grow with twice the growth rate of the $n = 1$ curve just like the $n = 0$ curve does. In fact, the $n \geq 2$ curves are pumped nonlinearly. A look at the spectra (not shown) reveals that all of the $n \geq 2$ modes have $k_r - k_\theta$ spectra just like that of the $n = 1$ mode. So this means that the nonlinear interaction that drives the $n \geq 2$ modes involves the fastest growing $n = 1$ linear eigenmode beating against an eigenmode that has $k_r \sim k_\theta \sim 0$. This second eigenmode has close to zero growth rate, meaning that the $n \geq 2$ modes will only grow at the same rate as the fastest growing $n = 1$ linear eigenmode and not at twice its growth rate. It's difficult to guess this *a priori* due to the complexity of the nonlinear transfer term, so it seems that simulation results have to provide the evidence for this.

CHAPTER 9

Finite Mean Flow Simulations

9.1 The LAPD Biasing Experiment

9.2 New Linear Instabilities

9.3 Statistical Comparisons to Experiment

9.4 Energy Dynamics Results

CHAPTER 10

Conclusion

APPENDIX A

The BOUT++ Code

I use the BOUT++ [DUX09] code to solve the model equations of Chapter 4. This is a free open-access code available at https://github.com/bendudson/BOUT. In this appendix, I briefly describe this code and my specific implementation of the model equations. I cannot simply paste the entire code here and explain it line for line because the code is on the order of 10^6 lines and quite complicated. Rather, I provide an overview of the BOUT++ framework and focus on describing and discussing details that are specific to my code implementation so that readers should be able to understand how to reproduce the simulations that I describe in this dissertation.

A.1 The Object-Oriented Fluid Framework

BOUT++ was built as an object-oriented C++ extension of BOUT. BOUT, short for Boundary Turbulence, was written by X. Q. Xu and M .V. Umansky [XC98, UXD09]. BOUT, written in C, evolves a set of drift-reduced Braginskii fluid equations in 3D tokamak geometry. P. Popovich and Umansky also made modifications to solve the equations in cylindrical geometry for simulation of LAPD turbulence [PUC10b]. BOUT++ is much more, however, than a C++ version of BOUT.

BOUT++ is a C++ framework for writing single or multi-species fluid simulations with an arbitrary number of equations in 3D curvlinear coordinates. The

framework allows input of a grid file, which contains information regarding the magnetic field geometry, the metric tensor, and axisymmetric equilibrium profiles and parameters if desired. Users may simulate fluids and plasmas in slabs, sheared slabs, cylinders, or tokamaks. The input equilibria have only one restriction in that they must be two-dimensional, having one axisymmetric coordinate.

The inner workings of the code take care of many of the difficult coding and numerical issues associated with writing fluid simulations. For example, users may run parallelized simulations that are spread onto multiple processors simply by specifying a number in an input file. Furthermore, one can specify the use of different implicit or explicit numerical schemes to solve the equations along with specific finite difference schemes to approximate spatial derivatives in the equations. None of the numerical schemes need be written by the user, although the framework also provides relatively simple ways that the user can implement his own finite difference schemes. Derivatives in the axisymmetric coordinate may be solved spectrally, but BOUT++ is not a spectral code in general.

Moreover, the user specifies the equation set to be solved in a "physics module." The equation set can be the Braginskii equations, MHD equations, Navier-Stokes equations, gyro-fluid equations, etc. Finally, BOUT++ evolves variables from initial conditions with boundary conditions applied at every time step. It cannot solve the eigensystem of a linear equation set. Overall, BOUT++ is easily adaptable to solving many different hydrodynamic and plasma physics models. More information can be obtained in the various reference manuals included in the downloaded working tree.

I have implemented a specific LAPD turbulence model in the BOUT++ framework using the equations, sources, profiles, and parameters outlined in Chapter 4. In the next section, I explain the specific choices of numerical schemes that I use for the time evolution and the spatial differential operators.

A.2 Numerical Schemes

A.2.1 Spatial Finite Differences

In my BOUT++ LAPD turbulence implementation, the code uses the current state of the fields $(N, T_e, \phi, v_{\|e})$, equilibrium profiles, and transport coefficients to calculate the right hand side (RHS) of Eqs. 4.1- 4.4. Then the code explicitly time evolves the fields $(N, T_e, \varpi, v_{\|e})$. The code does this at each spatial location. So the first step is the calculation of the RHS of the equations, all of which involve a number of differential operators.

For the linear advection terms such as $\mathbf{v_E} \cdot \nabla N_0$, I write this out explicitly into an azimuthal derivative of ϕ times a radial derivative of N_0 and use simple first-derivative central 4^{th} order finite difference schemes for each of these. For the perpendicular Laplacian operators, I use Fourier transforms, which is the standard BOUT++ scheme for this. For the parallel Laplacian operator, I use a second-derivative central 4^{th} order finite difference scheme.

For the parallel gradient operators, I use a quasi-staggered method to prevent grid-sized oscillations on top of the solution that are called grid modes. For the explanation of why non-staggered numerical schemes can cause unphysical grid modes, see Appendix C in Popovich et al. [PUC10b]. In the quasi-staggered method, I use a first derivative first or third order one-sided finite difference scheme for the parallel gradients. I use a right-sided scheme for the derivatives when they are applied to the flux variables ($v_{\|e}$ and $j_{\|}$) and a left-sided scheme when applied to the state variables (N, T_e, and ϕ). BOUT++ now has the capability to use real staggered grids in which the flux and state variables exist on different grids that are shifted by half a grid-spacing from one another, but this capability wasn't present when I started the work, so I had to use the quasi-staggered method of using different one-sided derivatives for the flux and state variables. I implemented the third-order schemes myself in the physics module, which I have pasted below, so

the one-sided third order schemes are not part of the standard BOUT++ internal code. I generally use the third order schemes, but I sometimes use the first order schemes, and the statistical solution doesn't significantly vary between the two different schemes.

Finally, for the nonlinear advection terms in the Poisson brackets, I generally use an Arakawa advection scheme that I have written into the physics module, which is not part of the BOUT++ internal code. The Arakawa advection scheme [Ara66] is useful for my purposes because it exactly conserves fluctuation energies of the type I have written in Chapter 6. I have used this advection scheme for all of the zero equilibrium flow simulations of Chapters 7 and 8. The Arakawa advection scheme can cause overshoots or spurious fluctuations at steep gradients, which is one of the reasons why I used artificial diffusion and viscosity in the equations. Another problem with the Arakawa advection scheme is that it is not a positivity-preserving scheme. The advection equation:

$$\frac{\partial A}{\partial t} + \mathbf{v} \cdot \nabla A = 0, \tag{A.1}$$

for any normal flow field $\mathbf{v}$ preserves the positivity of the variable A if it starts out positive everywhere. This is easy to see because anytime A becomes very small at a certain location not on the boundary, it becomes a local minimum there and its gradient goes to zero. This prevents A from decreasing any further. When dealing with finite differences, however, the gradient of A at a local minimum may be different from zero due to finite grid spacing effects. This can cause A to become negative at that point on a subsequent time step. Some finite difference advection schemes take this into account and do not allow A to become negative. Arakawa schemes do not. This can be a problem because the total density and electron temperature (N_t and T_{et} respectively) are physically positive quantities in my model. They should not be allowed to become negative at any time or spatial location. Otherwise, the results become unphysical, invalidating the simulation.

As long as the fluctuations are not too large, the total density and temperature remain positive when I use Arakawa advection. But I found that in the finite mean flow simulations, the fluctuations can become large enough that the total density and/or temperature become negative when I use the Arakawa scheme. In those cases, I use a first-order upwind (U1) advection scheme. In this scheme, the component $\left(v_x \frac{\partial A}{\partial x}\right)_{U1}$ is approximated as:

$$\begin{aligned} v_{x,i}\frac{A_i - A_{i-1}}{\Delta x} \quad &\text{for} \quad v_{x,i} > 0, \\ v_{x,i}\frac{A_{i+1} - A_i}{\Delta x} \quad &\text{for} \quad v_{x,i} < 0. \end{aligned} \tag{A.2}$$

It is easily confirmed that any local minimum must grow in amplitude from this formula (A is advected into the local minimum). Also note that a local maximum must shrink. Because of these properties, solutions tend to numerically smooth out, indicative of diffusive action. To show this explicitly, Eq. A.2 can be rewritten in an interesting way:

$$\left(v_x \frac{\partial A}{\partial x}\right)_{U1} = v_{x,i}\frac{A_{i+1} - A_{i-1}}{2\Delta x} - \frac{\Delta x}{2}|v_{x,i}|\frac{A_{i+1} - 2A_i + A_{i-1}}{(\Delta x)^2}. \tag{A.3}$$

The first term on the RHS is simply the expression for central second order advection, while the second term on the RHS is $\frac{\Delta x}{2}|v_{x,i}|$ times the expression for the central second order second derivative. So,

$$\left(v_x \frac{\partial A}{\partial x}\right)_{U1} = \left(v_x \frac{\partial A}{\partial x}\right)_{C2} - \frac{\Delta x}{2}|v_{x,i}|\left(\frac{\partial^2 A}{\partial x^2}\right)_{C2}, \tag{A.4}$$

meaning that the one dimensional advection equation with a first order upwind advection scheme is equivalent to the advection-diffusion equation with a second order central advection scheme and a diffusion coefficient of $\frac{\Delta x}{2}|v_{x,i}|$. This generalizes to the 3D advection equation as well. The diffusion is numerical diffusion,

and when I use U1 advection, I make sure to add this numerical diffusion to the artificial diffusion in my energy analyses to correctly obtain the energy dissipation.

Now, using a U1 advection scheme helps maintain positivity of the total density and temperature, but Eqs. 4.1 and 4.4 are not simple advection equations or even advection-diffusion equations. The density equation is close to an advection-diffusion equation, but since I partially linearize it, it doesn't preserve the concept of evolving the total density. And more importantly, the source term makes it a different equation altogether. Physically, the source is an ionization source and a recombination sink at the end plates, but in the model, it is much simpler. It's simply a term that corrects the equilibrium by essentially removing the flux-surface averaged density fluctuation component (Eq. 4.5). Such a source is clearly not positivity-preserving since it averages over an entire flux surface and has not knowledge of local total density. When positivity preservation becomes an issue in the simulations, I multiply the source terms in Eqs. 4.1 and 4.4 by N_t and T_{et} respectively whenever the sources are negative. Thus, when N_t or T_{et} becomes small, if the sources are negative, they become weaker so that they can't drive N_t and T_{et} negative. Physical sources must have this property, so it's not unreasonable to do this with the model sources.

A.2.2 Time Integration Technique

Perhaps the real power of BOUT++ lies in its time integration procedures. While a few simple explicit methods such as Euler and Runge-Kutta 4^{th} order methods come with the BOUT++ code, some much more sophisticated solver packages can be compiled with the code and used given simple user option choices. These packages generally work as a black box for the user, who only has to make a few choices regarding error tolerances and problem stiffness. The code that I use is the CVODE package that comes in the Sundials suite of codes. CVODE is a parallel solver that can solve stiff or nonstiff ODE initial value problems of the

form [CVO]:

$$\frac{du}{dt} = f(t, u). \tag{A.5}$$

Plasma simulations tend to be stiff due to the large range of time scales involved. Simple explicit schemes are generally too inefficient or too inacurate to use, and only some implicit schemes work with stiff systems. For stiff problems, CVODE uses the Backward Differentiation Formula (BDF). This formula approximates u at time n as

$$u_n = \sum_{i=1}^{q} \alpha_{n-i} u_{n-i} + h_n \beta_0 f_n, \tag{A.6}$$

where $f_n \equiv f(u_n, t_n)$, h_n is the timestep at time n, q is the order of the BDF method, and $\alpha n - i$ and β_0 are coefficients determined by the order of the BDF method. Since, f_n is unknown, CVODE uses a Newton formula to approximate it as

$$f_n \approx f_{n-1} + \frac{\partial f}{\partial u}(u_n - u_{n-1}). \tag{A.7}$$

$\frac{\partial f}{\partial u} \equiv J$ is the Jacobian. This allows Eq. A.6 to be written as

$$(1 - h_n \beta_0 J) u_n = \sum_{i=1}^{q} \alpha_{n-i} u_{n-i} + h_n \beta_0 f_{n-1} - h_n \beta_0 J u_{n-1}. \tag{A.8}$$

The process is actually more complicated as the Eq. A.7 approximation actually uses a Newton iteration[CVO], so that the solution can be computed more accurately. The user supplies error tolerances and CVODE iterates the solution until the tolerance is met. If the tolerance is not met after a certain number of iterations, CVODE changes the order of the implicit method. If this doesn't produce a tolerable error, CVODE reduces the time step and starts the procedure

again. These tolerance steps are not necessarily all done in this order. Again, CVODE is an efficient, yet complicated code.

References

[Ara66] A. Arakawa. "Computational Design for Long-Term Numerical Integration of the Equations of Fluid Motion." *J. Computational Physics*, **1**:119–143, 1966.

[BCR93] H. L. Berk, R. H. Cohen, D. D. Ryutov, Yu. A. Tsidulko, and X. Q. Xu. "Electron temperature gradient induced instability induced in tokamak scrape-off layers." *Nuclear Fusion*, **33**:263, 1993.

[BDT90] H. Biglari, P. H. Diamond, and P. W. Terry. "Influence of sheared poloidal rotation on edge turbulence." *Phys. Fluids B*, **2**:1, 1990.

[BF92] K. M. Butler and B. F. Farrell. "Three-dimensional optimal perturbations in viscous shear flows." *Phys. Fluids A*, **4**:1637, 1992.

[BK85] D. Biskamp and H. Kaifen. "Three-drift-wave interaction at finite parallel wavelength: bifurcations and transition to turbulence." *Phys. Fluids*, **28**:2172, 1985.

[Bra65] S. I. Braginskii. "Transport processes in a plasma." In M A Leontovich, editor, *Reviews of Plasma Physics*, volume 1, pp. 205–311. Consultants Bureau, New York, 1965.

[BRT91] H. L. Berk, D. D. Ryutov, and Yu. A. Tsidulko. "Temperature-gradient instability induced by conducting end walls." *Phys. Fluids B*, **3**:1346, 1991.

[BZ95] D. Biskamp and A. Zeiler. "Nonlinear Instability Mechanism in 3D Collisional Drift-Wave Turbulence." *Phys. Rev. Lett.*, **74**:706, 1995.

[CBS95] S. J. Camargo, D. Biskamp, and B. D. Scott. "Resistive drift-wave turbulence." *Phys. Plasmas*, **2**:48, 1995.

[Che06] F. F. Chen. *Introduction to Plasma Physics and Controlled Fusion.* Springer, 2006.

[CO77] C. Z. Cheng and H. Okuda. "Formation of convective cells, anomalous diffusion, and strong plasma turbulence due to drift instabilities." *Phys. Rev. Lett.*, **38**:708, 1977.

[CO79] C. Z. Cheng and H. Okuda. "Theory and numerical simulations on collisionless drift instabilities in three dimensions." *Nuclear Fusion*, **18**:587, 1979.

[CPB09] J. Cohen, J. Philip, and G. Ben-Dov. "Aspects of linear and nonlinear instabilities leading to transition in pipe and channel flows." *Phil. Trans. R. Soc. A*, **367**:509, 2009.

[CTC98] S. J. Camargo, M. K. Tippett, and I. L. Caldas. "Nonmodal energetics of resistive drift waves." *Phys. Rev. E*, **58**:3693, 1998.

[CVO] `https://computation.llnl.gov/casc/sundials/documentation/cv_guide/node3.html`. [Online; accessed 9-May-2013].

[DBB00] A. M. Dimits, G. Bateman, M. A. Beer, B. I. Cohen, W. Dorland, G. W. Hammett, C. Kim, J. E. Kinsey, M. Kotschenreuther, A. H. Kritz, L. L. Lao, J. Mandrekas, W. M. Nevins, S. E. Parker, A. J. Redd, D. E. Shumaker, R. Sydora, and J. Weiland. "Comparisons and Physics Basis of Tokamak Transport Models and Turbulece Simulations." *Phys. Plasmas*, **7**:969, 2000.

[DR81] P. G. Drazin and W. H. Reid. *Hydrodynamic Stability.* Cambridge University Press, 1981.

[DUX09] B. D. Dudson, M. V. Umansky, X. Q. Xu, P. B. Snyder, and H. R. Wilson. "BOUT++: A framework for parallel plasma fluid simulations." *Computer Physics Communications*, pp. 1467–1480, 2009.

[DZB95] J. F. Drake, A. Zeiler, and D. Biskamp. "Nonlinear Self-Sustained Drift-Wave Turbulence." *Phys. Rev. Lett.*, **75**:4222, 1995.

[FCU12] B. Friedman, T. A. Carter, M. V. Umansky, D. Schaffner, and B. Dudson. "Energy dynamics in a simulation of LAPD turbulence." *Phys. Plasmas*, **19**:102307, 2012.

[FCU13] B. Friedman, T. A. Carter, M. V. Umansky, D. Schaffner, and I. Joseph. "Nonlinear instability in simulations of Large Plasma Device turbulence." *Phys. Plasmas*, **20**:055704, 2013.

[FUC12] B. Friedman, M. V. Umansky, and T. A. Carter. "Grid Convergence Study in a Simulation of LAPD Turbulence." *Contrib. Plasma Phys.*, **52**:412–416, 2012.

[Gus91] L. H. Gustavsson. "Energy growth of three-dimensional disturbances in plane Poiseuille flow." *J. Fluid Mech*, **224**:221, 1991.

[HDC03] C. Holland, P. H. Diamond, S. Champeaux, E. Kim, O. Gurcan, M. N. Rosenbluth, G. R. Tynan, N. Crocker, W. Nevins, and J. Candy. "Investigations of the role of nonlinear couplings in structure formation and transport regulation: experiment, simulation, and theory." *Nuclear Fusion*, **43**:761, 2003.

[Hen96] D. Henningson. "Comment on "Transition in shear flows. Nonlinear normality versus non-normal linearity" [Phys. Fluids 7, 3060 (1995)]." *Phys. Fluids*, **8**:2257, 1996.

[Hor90] W. Horton. *Nonlinear drift waves and transport in magnetized plasma*. North-Holland, 1990.

[HR94] D. S. Henningson and S. C. Reddy. "On the role of linear mechanisms in transition to turbulence." *Phys. Fluids*, **6**:1396, 1994.

[HTJ11] D. R. Hatch, P. W. Terry, F. Jenko, F. Merz, and W. M. Nevins. "Saturation of Gyrokinetic Turbulence through Damped Eigenmodes." *Phys. Rev. Lett.*, **106**:115003, 2011.

[Hut02] I. H. Hutchinson. *Principles of Plasma Diagnostics*. Cambridge University Press, 2002.

[HW83] A. Hasegawa and M. Wakatani. "Plasma Edge Turbulence." *Phys. Rev. Lett.*, **50**:682–686, 1983.

[KMN99] S. B. Korsholm, P. K. Michelsen, and V. Naulin. "Resistive drift wave turbulence in a three-dimensional geometry." *Phys. Plasmas*, **6**:2401, 1999.

[Kol41] A. N. Kolmogorov. "The local structure of turbulence in incompressible viscous fluid for very large Reynolds numbers." *Dokl Akad. Nauk SSSR*, **30**:301–305, 1941.

[Kro99] J. A. Krommes. "Recent results on analytical plasma turbulence theory: realizability, intermittency, submarginal turbulence and self-organized criticality." *Plasma Phys. Control. Fusion*, **41**:A641–A652, 1999.

[Lan44] L. D. Landau. "On the problem of turbulence." *C.R. Acad. Sci. U.R.S.S.*, **44**:311, 1944.

[LL59] L. D. Landau and E. M. Lifshitz. "Fluid mechanics." In *Course of theoretical physics*, volume 6. London: Pergamon Press, 1959.

[Lor63] E. N. Lorenz. "Deterministic nonperiodic flow." *J. Atmos. Sci.*, **20**:130, 1963.

[LRH12] J. Loizu, P. Ricci, F. Halpern, and S. Jolliet. "Boundary conditions for plasma fluid models at the magnetic presheath entrance." *Phys. Plasmas*, **13**:122307, 2012.

[McD04] J. M. McDonough. "INTRODUCTORY LECTURES on TURBULENCE Physics, Mathematics and Modeling.", 2004.

[MM11] J. E. Maggs and G. J. Morales. "Generality of Deterministic Chaos, Exponential Spectra, and Lorentzian Pulses in Magnetically Confined Plasmas." *Phys. Rev. Lett.*, **107**:185003, 2011.

[MM12a] J. E. Maggs and G. J. Morales. "Exponential power spectra, deterministic chaos and Lorentzian pulses in plasma edge dynamics." *Plasma Phys. Control. Fusion*, **54**:12041, 2012.

[MM12b] J. E. Maggs and G. J. Morales. "Origin of Lorentzian pulses in deterministic chaos." *Phys. Rev. E*, **86**:015401, 2012.

[MTK11] K. D. Makwana, P. W. Terry, J. H. Kim, and D. R. Hatch. "Damped eigenmode saturation in plasma fluid turbulence." *Phys. Plasmas*, **18**:012302, 2011.

[MTK12] K. D. Makwana, P. W. Terry, and J. H. Kim. "Role of stable modes in zonal flow regulated turbulence." *Phys. Plasmas*, **19**:062310, 2012.

[PSM08a] D. C. Pace, M. Shi, J. E. Maggs, G. J. Morales, and T. A. Carter. "Exponential frequency spectrum and Lorentzian pulses in magnetized plasmas." *Phys. Plasmas*, **15**:122304, 2008.

[PSM08b] D. C. Pace, M. Shi, J. E. Maggs, G. J. Morales, and T. A. Carter. "Exponential Frequency Spectrum in Magnetized Plasmas." *Phys. Rev. Lett.*, **101**:085001, 2008.

[PUC10a] P. Popovich, M. V. Umansky, T. A. Carter, and B. Friedman. "Analysis of plasma instabilities and verification of BOUT code for linear plasma device." *Phys. Plasmas*, **17**:102107, 2010.

[PUC10b] P. Popovich, M. V. Umansky, T. A. Carter, and B. Friedman. "Modeling of plasma turbulence and transport in the Large Plasma Device." *Phys. Plasmas*, **17**:122312, 2010.

[RH93] S. C. Reddy and D. S. Henningson. "Energy growth in viscous channel flows." *J. Fluid Mech*, **252**:209, 1993.

[RR10] B. Rogers and P. Ricci. "Low-frequency turbulence in a linear magnetized plasma." *Phys. Rev. Lett.*, **104**:225002, 2010.

[RSH93] S. C. Reddy, P. J. Schmid, and D. S. Henningson. "Pseudospectra of the OrrSommerfeld operator." *SIAM J. Appl. Math.*, **53**:15, 1993.

[RT71] D. Ruelle and F. Takens. "On the Nature of Turbulence." *Commun. math. Phys.*, **20**:167, 1971.

[SC03] A. N. Simakov and P. J. Catto. "Drift-ordered fluid equations for field-aligned modes in low-β collisional plasma with equilibrium pressure pedestals." *Phys. Plasmas*, **10**:4744, 2003.

[Sco90] B. D. Scott. "Self-Sustained Collisional Drift-Wave Turbulence in a Sheared Magnetic Field." *Phys. Rev. Lett.*, **65**:3289, 1990.

[Sco92] B. D. Scott. "The mechanism of self sustainment in collisional drift wave turbulence." *Phys. Fluids B*, **4**:2468, 1992.

[Sco02] B. D. Scott. "The nonlinear drift wave instability and its role in tokamak edge turbulence." *New J. Physics*, **4**:52.1–52.30, 2002.

[Sco03] B. D. Scott. "Computation of electromagnetic turbulence and anomalous transport mechanisms in tokamak plasmas." *Plasma Phys. Control. Fusion*, **45**:A385–A398, 2003.

[Sco05] B. D. Scott. "Drift wave versus interchange turbulence in tokamak geometry: Linear versus nonlinear mode structure." *Phys. Plasmas*, **12**:062314, 2005.

[SCR12] D. A. Schaffner, T. A. Carter, G. D. Rossi, D. S. Guice, J. E. Maggs, S. Vincena, and B. Friedman. "Modification of Turbulent Transport with Continuous Variation of Flow Shear in the Large Plasma Device." *Phys. Rev. Lett.*, **109**:135002, 2012.

[SPM09] M. Shi, D. C. Pace, G. J. Morales, J. E. Maggs, and T. A. Carter. "Structures generated in a temperature filament due to drift-wave convection." *Phys. Plasmas*, **16**:062306, 2009.

[Sta00] P. C. Stangeby. *The plasma boundary of magnetic fusion devices*. Institute of Physics Publishing, 2000.

[TL72] H. Tennekes and J. L. Lumley. *First Course in Turbulence*. The MIT Press, 1972.

[TTR93] L. N. Trefethen, A. E. Trefethen, S. C. Reddy, and T. A. Driscoll. "Hydrodynamic Stability Without Eigenvalues." *Science*, **261**:578, 1993.

[UPC11] M. V. Umansky, P. Popovich, T. A. Carter, B. Friedman, and W. M. Nevins. "Numerical simulation and analysis of plasma turbulence the Large Plasma Device." *Phys. Plasmas*, **18**:055709, 2011.

[UXD09] M. V. Umansky, X. Q. Xu, B. Dudson, L. Lodestro, and J. Myra. "Status and verification of edge plasma turbulence code BOUT." *Phys. Plasmas*, **180**:887, 2009.

[Wal95] F. Waleffe. "Hydrodynamic Stability and Turbulence: Beyond Transients to a Self-Sustaining Process." *Studies in Applied Mathematics*, **95**:319, 1995.

[Wes04] J. Wesson. *Tokamaks*. Clarendon Press, 2004.

[XC98] X. Q. Xu and R. H. Cohen. "Scrape-Off Layer Turbulence Theory and Simulations." *Contrib. Plasma Phys.*, **36**:158, 1998.

[XRD93] X. Q. Xu, M. N. Rosenbluth, and P. H. Diamond. "Electron-temperature-gradient-driven instability in tokamak boundary plasma." *Phys. Fluids B*, **5**:2206, 1993.

[ZBD96] A. Zeiler, D. Biskamp, J. F. Drake, and P. N. Guzdar. "Three-dimensional fluid simulations of tokamak edge turbulence." *Phys. Plasmas*, **3**:2951, 1996.

[ZDB97] A. Zeiler, J. F. Drake, and D. Biskamp. "Electron temperature fluctuations in drift-resistive ballooning turbulence." *Phys. Plasmas*, **4**:991, 1997.